FABRY-PÉROT STUDIES OF THE MILKY WAY BAR: KINEMATICS, CHEMICAL COMPOSITION AND INSTRUMENTATION

BY NASEEM RANGWALA

A dissertation submitted to the

Graduate School—New Brunswick

Rutgers, The State University of New Jersey

in partial fulfillment of the requirements

for the degree of

Doctor of Philosophy

Graduate Program in Physics and Astronomy

Written under the direction of

Theodore Williams

and approved by

_____

_____

_____

_____

_____

New Brunswick, New Jersey

October, 2009

ABSTRACT OF THE DISSERTATION

Fabry-Pérot Studies of the Milky Way Bar: Kinematics, Chemical Composition and Instrumentation

by Naseem Rangwala

Dissertation Director: Theodore Williams

Galactic bars and bulges play an important role in the formation and evolution processes in disk galaxies. There is now substantial evidence that our Galaxy is barred, and many unresolved questions about the structure, dynamics and star formation history of the inner Galaxy remain.

We use Fabry-Pérot (FP) absorption line imaging spectroscopy to measure radial velocities using the CaII8542 line in 3360 stars towards three lines of sight in the Milky Way's bar: Baade's Window and offset positions at $(l, b) \simeq (\pm 5.0, -3.5)^\circ$. This sample includes 2488 bar red clump giants, 339 bar M-giants, and 318 disk main sequence stars. We measure the first four moments of the stellar velocity distribution of the red clump giants, and find it to be symmetric and flat-topped. We detect stellar streams at the near and far side of the bar with velocity difference $\gtrsim$ 30 km s^{-1}at $l = \pm 5^\circ$, indicating strong non-circular motions. We do not detect two separate streams in Baade's Window. Our M-giants kinematics agree well with previous studies, but have dispersions systematically lower than those of the red clump giants by $\sim$ 10 km s^{-1}.

We show that reliable absorption line strengths can also be measured using FP

spectroscopy. The CaII8542 line is a good indicator of metallicity and its calibration to [Fe/H] is determined for globular cluster red giants in previous investigations. We derive such a calibration for the bulge giants and use it to infer metallicities for our red clump sample. We present the stellar metallicity distributions along the major axis of the bar. We find the mean [Fe/H] in Baade's Window close to solar, and the distribution in this field agrees well with previous works. We find negative gradients in the mean metallicity and its dispersion along the bar. We detect a signature of a possible new tidal stream at $l = +5.5°$, in both our velocity and metallicity distributions. We also measure the metallicity of a bulge globular cluster NGC 6522 in our Baade's Window field to be -0.9 dex, in good agreement with previous high-resolution spectroscopic measurements, demonstrating the reliability of our metallicity measurements.

We also present the design and testing of the FP system for the 10-meter class Southern African Large Telescope, and its characterization as measured in the laboratory. It provides spectroscopic imaging at any desired wavelength spanning a bandpass 430 – 860 nm, at four different spectral resolving powers ($\lambda/\Delta\lambda$) ranging from 300 to 9000. This FP system will provide a powerful tool for imaging spectroscopy on one of the world's largest telescopes.

Acknowledgements

I am grateful to many people who have helped me in different ways over the years to make this thesis possible. It was a transforming experience for me that I will always remember with pleasure.

I want to start by thanking my thesis advisor, Ted Williams. I am so lucky to have had him as my advisor. Ted is a very intelligent, kind and generous person from whom I have learned a lot. He has always been there to help, guide and make me laugh. Working with him has always been enjoyable and I have gained a lot of confidence from it. He is an expert in Fabry-Pérot instrumentation and observation so it was truly a pleasure to learn these skills from him. I also really appreciate his help in improving the English of my papers and this thesis, which read so much better now. He has invited me to numerous parties, which were fun and made me feel at home in a new country. Thank you very much Ted!

I am thankful for the help and advice of the entire astronomy faculty. I am especially grateful to Jerry Sellwood and Tad Pryor for their invaluable advice on this thesis. Tad is our local expert on many astronomy related topics, from whom almost every graduate student has gained knowledge and skill. He is always available to answer questions. Jerry's expertise in galactic dynamics has really helped this thesis. He and Ted wrote the observing/grant proposal almost ten years ago that made this work possible. I want to thank Terry Matilsky, Jack Hughes and Chuck Joseph for having many interesting as well as funny conversations. Chuck, thanks for letting us use your lab for testing our instrument. I want to thank Eric Gwaiser, Andrew Baker, Chuck Keeton and Saurabh Jha for their great help on dealing with the whole job hunting process and for always

being available to talk.

I want to thank the postdocs, Kristine Spekkens, Carlos Badenes, Felipe Menanteau and Gamil Cassam-chenai from who I have received great advice, and had fun chatting with them about variety of topics. Ron Ransome deserves a special thanks for being an awesome graduate director. He has always worked very hard every year to find funding for all students, and has helped many students to attend conferences on departmental funds. He has been very supportive and helpful to international students who always had some kind of visa issues. I have really enjoyed the company of Premi Chandra, with whom I had several lunches and great discussions. Many thanks to the administrative staff of the department for their time and help.

One of the best parts of grad school is making new friends with graduate students from all over the world. My time in graduate school would have been much harder, and much less fun without the friendship and support of Neelima Sehgal, Jessica Warren and Ricardo Sanchez. I also want to thank my other fellow grad friends, Maya Todua, Bonita DeSwardt, Gareth Hughes, Monica Hasegan, Juntai Shen, Matthew Francis, and Ross Fadely for their support. Ross - It was great to discuss astro-ph with you every morning and I am going to miss that, and Bonita - you are my best South African host and reminder of the fun memories of my time in Cape Town.

Finally, I want to thank my family. Without their love, support and patience this PhD would not have been possible. I want to first thank my best friend and husband, Eric, for his love, care and for always believing in me. I have learnt so much from him. He has enriched my life every day with many interesting and passionate discussions about astronomy, politics, culture, and the arts. I also want to mention our three cats Tango, Xander and Asha for just being so cute and loving. My brother Imtiaz has always been my mentor and friend throughout my life. Without him I would not have survived my first year in the US, and I am so happy we are finishing our PhDs together. I want to thank my sister-in-law, Kritee, for her strength, love and support. I am deeply

indebted to my parents for letting me pursue my dreams. Their unconditional love and support has been a source of constant happiness and security in my life. Thank you is not enough for them. I am so lucky to have been brought up by all four grandparents (Dada, Dadi, Nana and Nani). Their incredible strength and wisdom has taught me so much and made me a better person. I dedicate this thesis to them.

Dedication

For my Grandparents: Nana, Nani, Dada and Dadi

Table of Contents

List of Tables

List of Figures

Chapter 1

Introduction

Galaxies are the building blocks of the universe. They are classified broadly into two types: elliptical and spiral. The elliptical galaxies have smooth, featureless spheroidal shapes and are made up of an old stellar population with very little gas and dust, and are supported mostly by random motions. The spirals are flat and rotationally supported, and usually consist of an array of rich dynamical features such as bars, bulges, rings and spiral arms. They are gas rich and have on-going star formation. About two-third of the spiral or disk galaxies in the universe are barred, including our own Milky Way (MW). Figure 1.1 (top) shows an image of a majestic barred spiral galaxy NGC 1365.

Most spiral galaxies have some type of central bulge. Depending on the formation process it is usually classified into one of two types: pseudo or classical bulge. The pseudobulge is formed from the internal secular (slow) evolution of disk galaxies, producing a bar-like feature when viewed face on and looks like a boxy (peanut shaped) bulge when viewed edge on. On the other hand a rapid formation (mergers) gives rise to a dynamically hot featureless classical bulge that has morphology and characteristics very similar to an elliptical galaxy. This topic has been reviewed in detail by Kormendy & Kennicutt (2004) and Kormendy & Fisher (2008). Dynamical and chemical studies of both types of bulges provides important clues to the formation and evolution of disk galaxies. Bars provide a crucial mechanism of channeling gas from the disk to very small radii at the center of galaxy triggering new star formation, and are speculated to feed the active galactic nuclei. Many correlations exists between the properties of the bulge and the host galaxy, for example, the correlation of the bulge's velocity dispersion with

the mass of the central supermassive black hole (Ferrarese & Merritt 2000; Gebhardt K. and Bender). Bars also interact with the dark matter halo via dynamical friction and slow down by losing angular momentum to the halo (Debattista & Sellwood 2000). The measurement of angular speed of the bar thus provides an important constraint on the disk to halo mass ratio for the inner parts of a galaxy.

1.1 Milky Way Bar

The structure of the inner regions of our Galaxy has been studied for decades now. Our specific position in the Galaxy is both a blessing and a curse. Residing in the disk of the Galaxy we cannot see the inner structure directly, and have to infer it from indirect observations. Figure 1.1 (bottom) shows an artist's conception of our Galaxy, constructed using the observed parameters. This is also the only galaxy that we can study in extraordinary detail because we can resolve the individual stars and measure their position, motion and chemical abundance. Our Galaxy provides us with a laboratory to test the theories of galaxy formation and evolution.

The bar in the MW is now firmly established both in photometric and dynamical observations but the parameters of the bar are a matter of some controversy. Its signature is seen as a peanut shaped bulge in the COBE image as shown in Figure 1.3. Figure 1.2 shows another barred spiral seen edge-on with a distinct peanut bulge. The modeling of the COBE data is consistent with a bar at an orientation angle (w.r.t the sun-galactic center line) between 10°– 15°, semimajor axis of 1 kpc, and rotating with an angular speed of 60 km s^{-1} kpc^{-1} (Zhao 1996; Dwek et al. 1995). The strong non-circular motions of the HI gas agrees with a bar at 35°, 3.6 kpc semimajor axis and rotating with an angular speed of 42 km s^{-1} kpc^{-1}. The photometry of the the red clump giant stars from the OGLE survey reveals that they are systematically brighter by +0.4 magnitudes at positive Galactic longitudes (closer to us) than the negative longitudes (Stanek et al. 1997) agreeing with a bar with orientation of 20° and 3.5

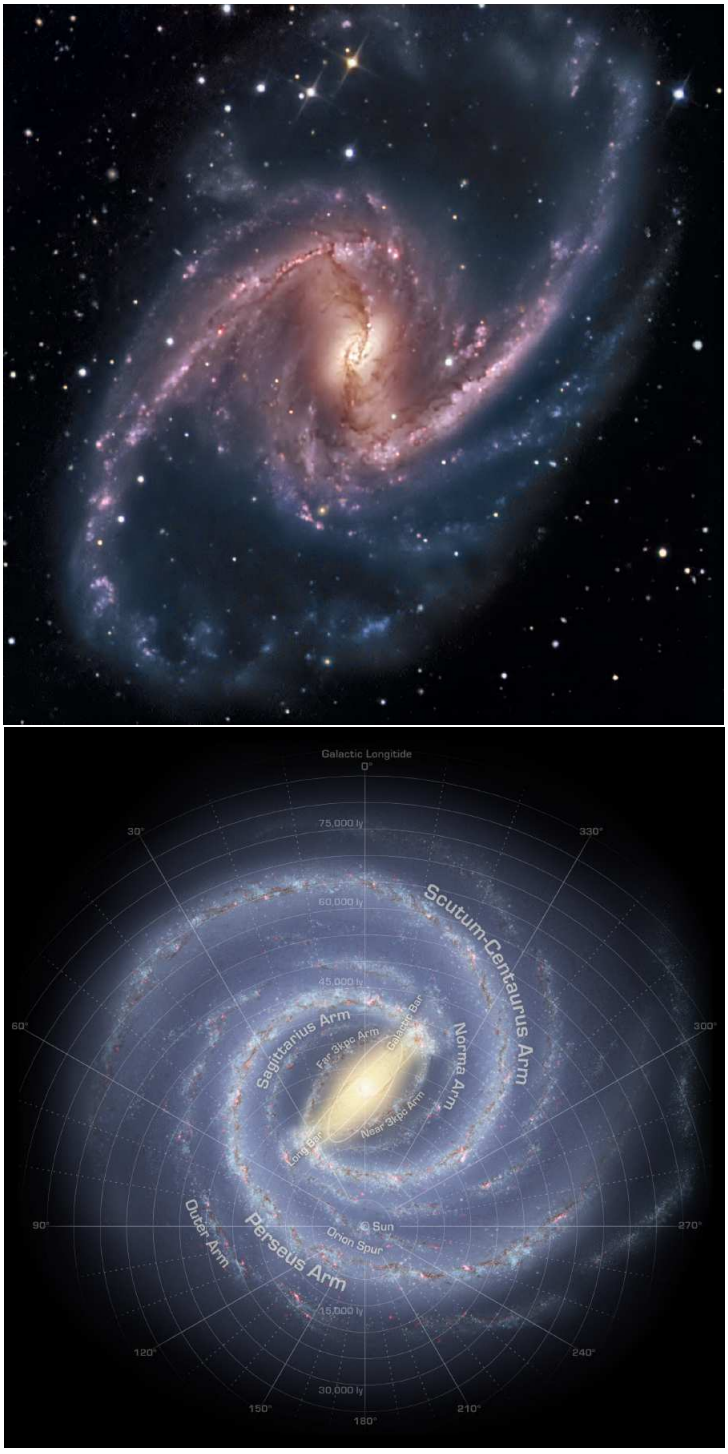

Figure 1.1 Top: Barred spiral galaxy NGC 1365; Bottom: Artist's conception of the Milky Way.

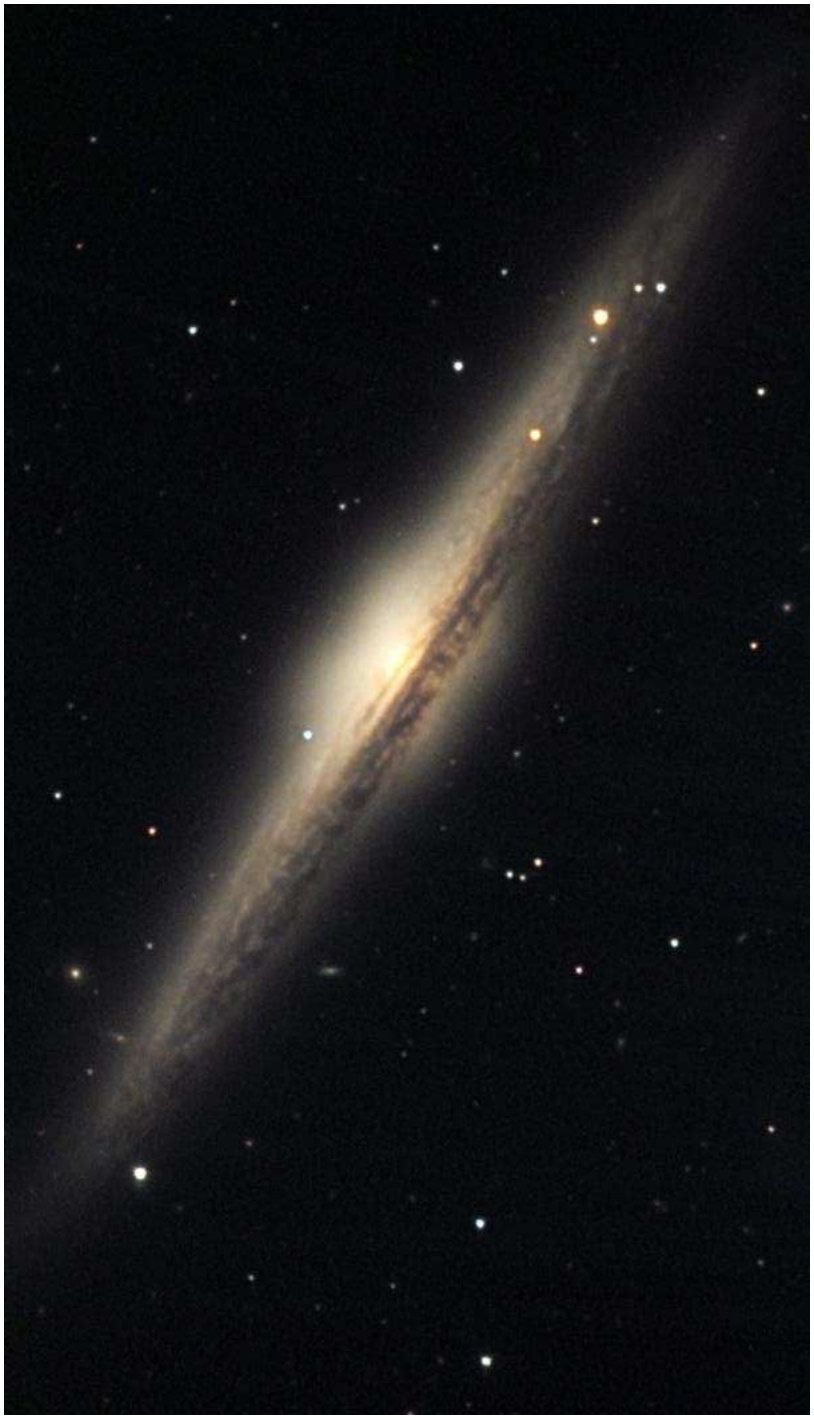

Figure 1.2 Peanut shape bulge in NGC 5746

kpc semimajor axis. The measurements of stellar radial velocity and dispersion in the bar give the ratio of ordered to random motion (V_{max}/σ) that is consistent with that of a pseudobulge (Rich et al. 2007) when placed on Kormendy & Kennicutt plot of V_{max}/σ vs ϵ, where ϵ represent the apparent flattening of the bulge. The recent Spitzer (infrared satellite) observations (Benjamin 2008; Benjamin et al. 2005) of the inner Galaxy suggest that the bar may extend much further out to $l = \pm 30^{\circ}$ compared to $l = \pm 10^{\circ}$ as found by the COBE data, with an orientation angle as large as $\sim 45^{\circ}$.

All these observations agree on the existence of bar (or pseudobulge) but do not agree on its characteristics such as orientation, shape, size and pattern speed. Moreover the MW bar is a stellar feature, but its signature is not yet unambiguously confirmed in the stellar kinematics. In addition, the chemical abundance measurements in the central parts of the galaxy show that alpha-elements (such as O, Ca, Mg) are enhanced compared to Fe, suggesting a classical bulge that formed on a very short timescale with a high star formation rate, most of these abundance studies are limited to Baade's Window (BW) (a low extinction window towards the Galactic center), leading to a debate on whether there is an old classical bulge population at the center in addition to the bar. Measuring the shape of the stellar velocity and metallicity distributions, and α/Fe (α stands for alpha-elements produced in type II supernova such as Ca and Mg) along the bar will put strong constraints on the chemical and dynamical models of the inner galaxy, and should also help distinguish between a bar and a classical bulge (if present). An ideal measurement would be to do tomography of the inner galaxy by measuring radial velocity, proper motion, distances and abundances of a large sample of individual stars. Such a sample can only be obtained for our Galaxy and will once and for all resolve issues related to the structure and formation of the inner galaxy and will also lead to a better understanding of disk galaxies.

Most stellar kinematics and abundance studies in the past have been limited to BW where the observations are not sensitive to the non-axisymmetric signature of the bar.

Recently, Howard et al. (2008) conducted a survey by measuring radial velocities of stars for several LOS along the major and minor axis of the bar. These observations have addressed a crucial problem of measuring kinematics away from BW. However their sample size is about 100 stars per LOS, insufficient to measure the shape of the velocity distribution and to estimate the radial streaming motions. One of the goals of this thesis is to use Fabry-Pérot imaging spectroscopy to obtain a large sample of stellar radial velocities in order to make these sensitive measurements.

1.2 Fabry-Pérot Spectroscopy

Fabry-Pérot (FP) interferometer or etalon consists of two parallel reflecting plates. The incident light goes through multiple reflections between the plates resulting in high resolution interference pattern. The interferometer can be tuned to a desired wavelength by changing the gap between the plates.

For astronomical observations, FP spectroscopy can provide narrow band spectra over the full field of view (FOV) of the telescope. It is most effective for objects that cover a large portion of the telescope's FOV. A series of images are taken around an absorption or emission feature of interest, building up a datacube as shown in Figure 1.3, where an absorption line can be measured for every star in the image, producing radial velocities and line strengths of hundreds or thousands of stars simultaneously. This type of dataset is in a sense orthogonal to the one obtained from a slit spectrograph where a spectrum is obtained over a large wavelength range covering many spectral lines for a single object or one dimensional slit.

FP emission line spectroscopy has been very successful in measuring velocity fields of spiral galaxies, star forming regions, planetary nebulae, and supernova remnants. As an example we show the FP velocity field of NGC 1365 in Figure 1.4 measured by Zánmar Sánchez et al. (2008). The absorption line work is less common but has been used to measure kinematics of stars in globular clusters (Gebhardt et al. 1994) and

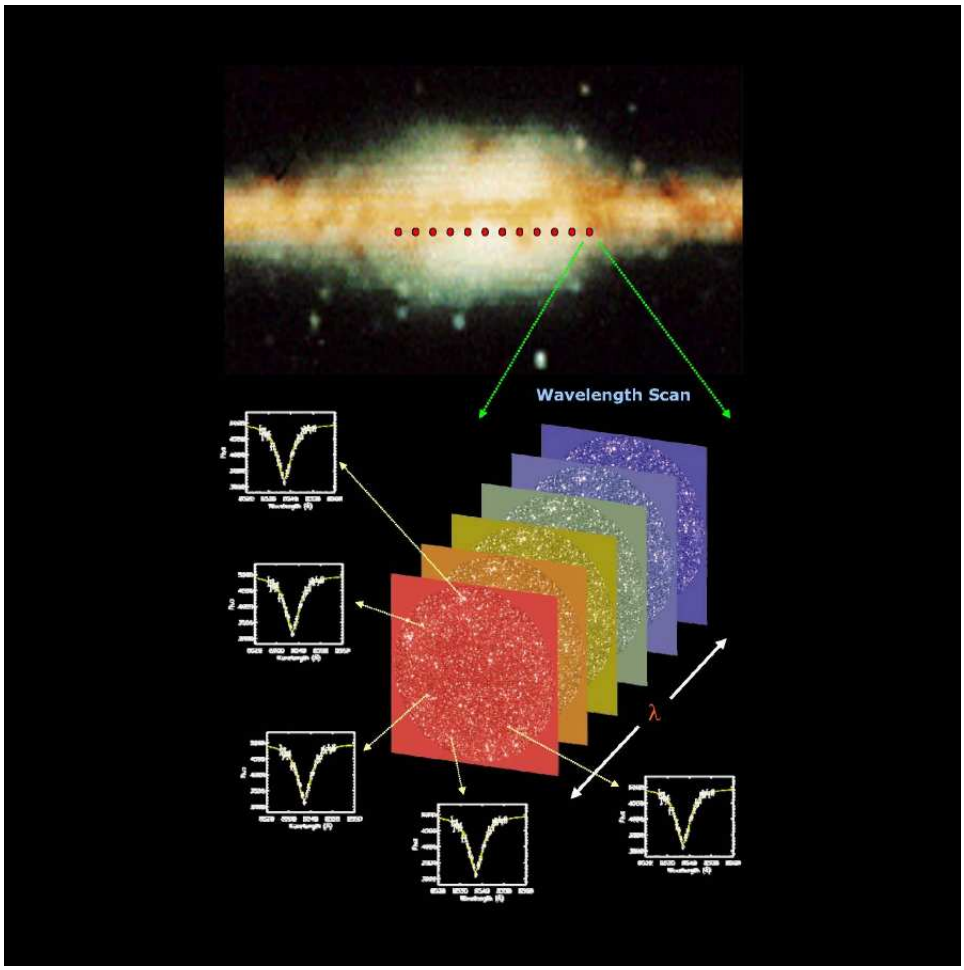

Figure 1.3 Top: COBE map of the inner Milky Way showing a distinct peanut-shaped bulge. Bottom: A schematic of Fabry-Pérot datacube.

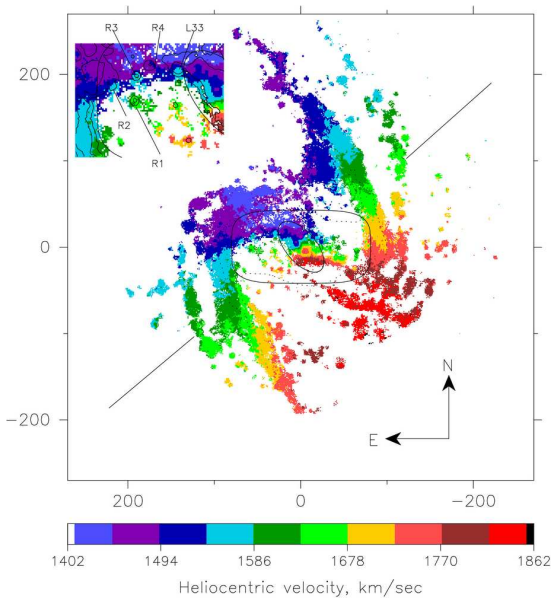

Figure 1.4 Fabry-Pérot emission line velocity map for NGC 1365 from Zánmar Sánchez et al. (2008).

pattern speed of the bar in NGC 7079 (Debattista & Williams 2004).

1.3 Purpose of the Thesis

In this thesis we study the MW bar by measuring radial velocities and metallicities of red clump giant stars. The presence of bar will distort stellar orbits so they are no longer circular but rather become elongated streams around the bar. Measuring the shape of the velocity distributions and streaming motions at several LOS in the bar can provide strong constraints on the dynamical models of inner Galaxy. All previous stellar radial velocity measurements were obtained from slit spectroscopy where typically ~ 100 stars are observed per LOS, too few to make these sensitive measurements and to constrain the parameters of the bar quantitatively.

The initial motivation of this thesis was to use the technique of Fabry-Pérot imaging spectroscopy to obtain a large sample of stellar radial velocities in the bar. In Chapter 2 we present the FP observations along three LOS in the MW bar. These observations produced an order of magnitude larger sample compared to previous investigations

using slit spectroscopy. In addition, this work also provides first detailed investigation into using these techniques to measure reliable line strengths from the same data set (Chapter 3). Because we measure the Ca II λ8542 line we can use its EW to infer metallicities for our sample, providing an additional constrain for the models. Future FP absorption line work will measure both kinematics and line strengths for more stars, and over larger parts of the inner the inner Galaxy.

This thesis is also describing the design and testing of dual-etalon FP instrumentation for SALT (Chapter 4) that will be used to extend the above measurements to several LOS in the inner Galaxy, for a detailed survey of the bar, and will have the capability of carrying out many other exciting astronomical observations. Unfortunately, there are not many FP systems on telescopes around the world. The SALT FP system that we describe in Chapter 4 can be used at four different resolving power (500, 1000, 2500, 9000) for any wavelength between 400 – 900 nm. On a 10-m class telescope this system has a great potential to study fainter and higher redshift systems. We hope that this thesis encourages the astronomical community to appreciate the efficiency of this technique and use it.

Bibliography

Benjamin, R. A. 2008, in Bulletin of the American Astronomical Society, Vol. 40, Bulletin of the American Astronomical Society, 266–+

Benjamin, R. A., Churchwell, E., Babler, B. L., Indebetouw, R., Meade, M. R., Whitney, B. A., Watson, C., Wolfire, M. G., Wolff, M. J., Ignace, R., Bania, T. M., Bracker, S., Clemens, D. P., Chomiuk, L., Cohen, M., Dickey, J. M., Jackson, J. M., Kobulnicky, H. A., Mercer, E. P., Mathis, J. S., Stolovy, S. R., & Uzpen, B. 2005, ApJ, 630, L149

Debattista, V. P., & Sellwood, J. A. 2000, ApJ, 543, 704

Debattista, V. P., & Williams, T. B. 2004, ApJ, 605, 714

Dwek, E., Arendt, R. G., Hauser, M. G., Kelsall, T., Lisse, C. M., Moseley, S. H., Silverberg, R. F., Sodroski, T. J., & Weiland, J. L. 1995, ApJ, 445, 716

Ferrarese, L., & Merritt, D. 2000, ApJ, 539, L9

Gebhardt, K., Pryor, C., Williams, T. B., & Hesser, J. E. 1994, AJ, 107, 2067

Gebhardt, K. and Bender, R. and Bower, G. and Dressler, A. and Faber, S. M. and Filippenko, A. V. and Green, R. and Grillmair, C. and Ho, L. C. and Kormendy, J. and Lauer, T. R. and Magorrian, J. and Pinkney, J. and Richstone, D. and Tremaine, S. 2000, ApJ, 539, L13

Howard, C. D., Rich, R. M., Reitzel, D. B., Koch, A., De Propris, R., & Zhao, H. 2008, ApJ, 688, 1060

Kormendy, J., & Fisher, D. B. 2008, 396, 297

Kormendy, J., & Kennicutt, Jr., R. C. 2004, ARA&A, 42, 603

Rich, R. M., Reitzel, D. B., Howard, C. D., & Zhao, H. 2007, ApJ, 658, L29

Sellwood, J. A., & Wilkinson, A. 1993, Reports of Progress in Physics, 56, 173

Stanek, K. Z., Udalski, A., Szymanski, M., Kaluzny, J., Kubiak, M., Mateo, M., & Krzeminski, W. 1997, ApJ, 477, 163

Zánmar Sánchez, R., Sellwood, J. A., Weiner, B. J., & Williams, T. B. 2008, ApJ, 674, 797

Zhao, H. S. 1996, MNRAS, 283, 149

Chapter 2

Fabry-Perot Absorption Line Spectroscopy of the Galactic Bar. I. Kinematics

The material in this chapter also appears in print as "Fabry-Perot Absorption Line Spectroscopy of the Galactic Bar. I. Kinematics", Rangwala et al. 2008, ApJ, 691, 1387.

2.1 Introduction

More than half of the disk galaxies in the universe have central bars (Freeman 1996). N-body simulations show that bars form naturally in disk galaxies, and play a crucial role in their formation and evolution (Sellwood & Wilkinson 1993). There is now abundant evidence that our own Galaxy is barred (see review by Gerhard 1999). One of the earliest indications came from the large non-circular motions of gas in the inner galaxy measured by de Vaucouleurs (1964) and subsequently by Liszt & Burton (1980). But it was not until the 1990s that the presence of a bar in the Milky Way (MW) was firmly established by the observations of a distinct peanut-shaped bulge in the COBE NIR light distribution (Blitz & Spergel 1991; Freudenreich 1998), a non-axisymmetric signature in the gas kinematics (Binney et al. 1991; Weiner & Sellwood 1999), OGLE photometry showing a magnitude offset of the bulge red clump giants at positive and negative longitudes (Stanek et al. 1997), and a large optical depth of the bulge to microlensing (Alcock et al. 2000). All these observations agree that the bar is inclined at some orientation angle with respect to the Sun-Galactic center line with its the near end in the first Galactic quadrant ($0^\circ \leq l \leq 90^\circ$).

Nonaxisymmetric models of the inner Galaxy have been produced in the last decade. Bissantz & Gerhard (2002) and Dwek et al. (1995) used COBE data to model the density distribution in the Galactic bar. Weiner & Sellwood (1999) measured the properties of the bar using gas kinematics. Rattenbury et al. (2007b) used red clump giants to trace the mass distribution of the bar. Zhao (1996) and Bissantz et al. (2004) have taken initial steps towards building fully self-consistent stellar dynamical models based on the available density and kinematic data. Existing stellar kinematic observation are insufficient to fully constrain the models, and there is significant variation in the estimates of the bar parameters such as orientation $(15^\circ - 45^\circ)$[1] , co-rotation radius (3.5 – 5 kpc) and pattern speed $(35 - 60$ km s^{-1} kpc$^{-1})$. There is not yet a unified quantitative dynamical model of the Galactic bar that explains all the observations in a consistent manner and the properties of the Galactic bar are still poorly determined.

The signature of the Galactic bar should also be seen in the kinematic distortions of the stellar velocity field, since the orbits are no longer circular, but rather are elongated streams along the bar. The stellar kinematic evidence of bulge triaxiality is still ambiguous. There has been significant work done in the past on the line-of-sight velocities of M and K giants (Rich 1990; Sharples et al. 1990; Terndrup et al. 1995; Minniti et al. 1992; Habing et al. 2006) and proper motions (Spaenhauer et al. 1992; Sumi et al. 2004; Rattenbury et al. 2007a; Clarkson et al. 2008) in the bulge. But most of these radial velocity observations were limited to the low extinction Baade's Window ($l \sim 0^\circ$). Häfner et al. (2000) show that measurements in Baade's Window (BW) alone are insensitive to the effects of triaxiality, and a stronger kinematic signature of the bar will be apparent away from $l = 0^\circ$. The ideal observation would be to measure stellar velocity distributions with high S/N for several lines-of-sight (LOS) in the bar. A sample size of ~ 1000

[1]Although most previous investigations find bar orientation angles between $20 - 30^\circ$, others (Weiner & Sellwood 1999; Benjamin et al. 2005; Cabrera-Lavers et al. 2008) have shown that the orientation angle could be as high as $35^\circ - 45^\circ$.

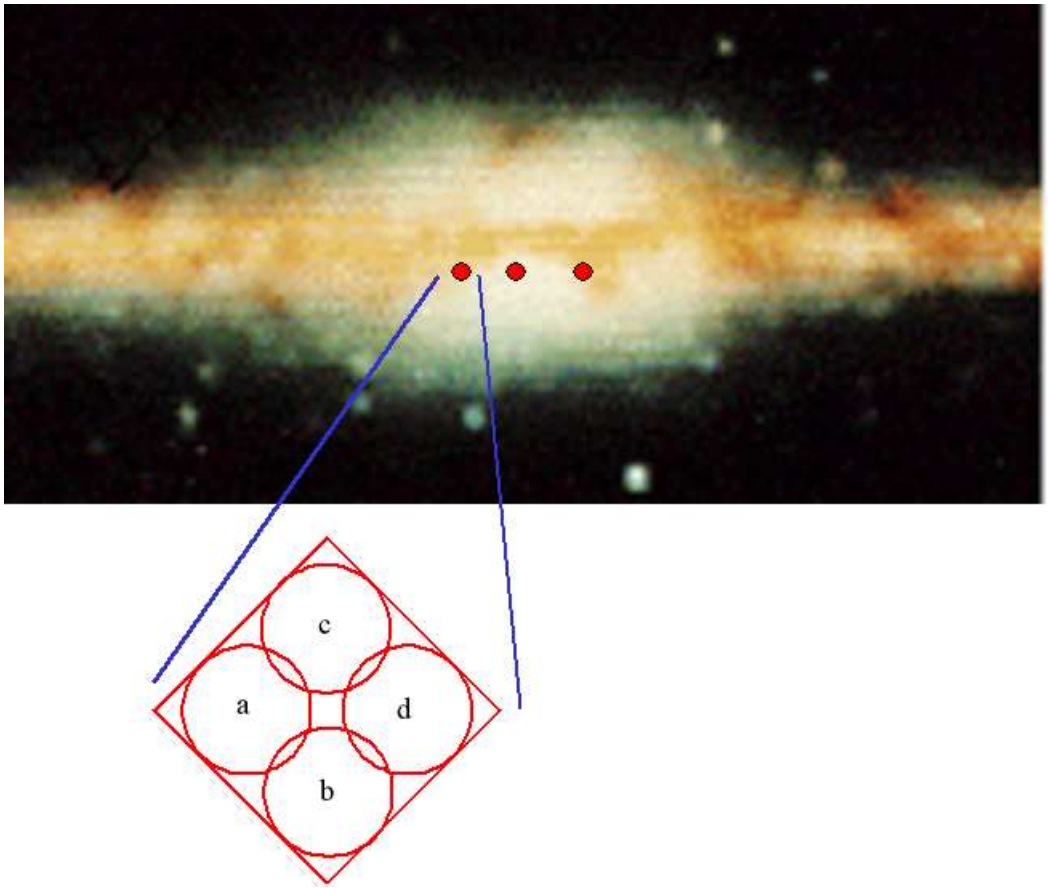

Figure 2.1 The position of our fields against the COBE NIR background. From left to right are the MM7B, BW and MM5B fields. MM7B and MM5B each have four overlapping sub-fields as shown in the box.

stars per LOS would enable the measurements of the higher moments of the velocity distribution and of the average radial velocity shift between the stellar streams in the bar (Mao & Paczyński 2002; Deguchi et al. 2001). In addition, combining accurate proper motions with these LOS velocities would provide even stronger constraints on the current dynamical models of the Galactic bar.

Further, the ratio of organized stellar streaming motion around the bar to random motion constrains the bar's angular rotation speed (also called pattern speed) (van Albada & Sanders 1982). Since bars can interact strongly with dark matter halos, transferring angular momentum into the halo and slowing the bar rotation dramatically (Debattista & Sellwood 2000), constraining the current pattern speed of the MW bar will provide a bound on the disk to halo mass ratio for the inner Galaxy.

The most recent bulge radial velocity survey by Howard et al. (2008) (also see Rich et al. 2007) measured radial velocities at many positions along the major and minor axes of the bar, obtaining the rotation and velocity dispersion curves. These observations have addressed the crucial problem of measuring kinematics of the bar away from BW. However, their sample size along each LOS is limited to about 100 stars, insufficient to measure the higher moments of the individual velocity distributions or the kinematics of the stellar streams. Our goal in the current investigation is to obtain a large radial velocity sample along several LOS, in order to measure these important quantities.

The basic procedure in Fabry-Pérot (FP) imaging spectroscopy is to obtain a series of narrow-band images, tuning the interferometer over a range of wavelengths covering a spectral feature of interest. The data cube thus produced is analyzed to extract a short portion of the spectrum of each object in the field of view. This spectrum is fit to determine the strength, width and central wavelength of the spectral feature, and the level of the adjacent continuum. If there are many objects of interest within the field of view, the technique can be extremely efficient. FP spectroscopy has traditionally been used to measure emission features in extended objects, and has been highly successful

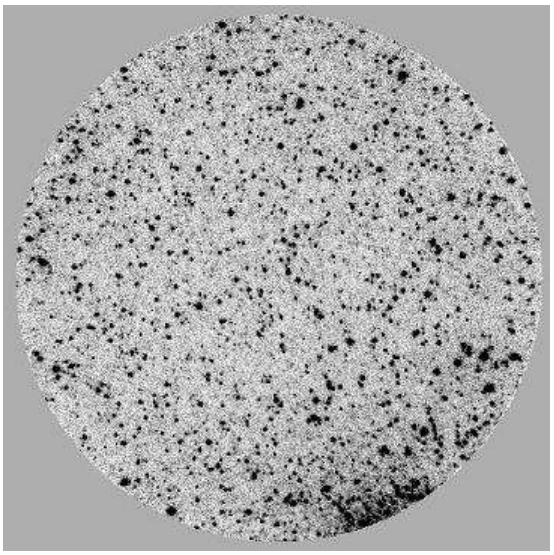

Figure 2.2 A Fabry-Pérot image of the Baade's Window stellar field. The FOV is $4'$ and the central wavelength is 8543 Å. The increasing stellar density towards the southwest edge of the field is caused by the bulge globular cluster NGC 6522.

for studying the velocity fields in disk galaxies (e.g. Palunas & Williams 2000; Zánmar Sánchez et al. 2008) star forming regions (Hartigan et al. 2000), planetary nebula (Sluis & Williams 2006), and supernova remnants (Ghavamian et al. 2003). It is less common to employ FP techniques to measure absorption spectra, but they have been used to determine the kinematics of stars in a large number of globular clusters (Gebhardt et al. 1994), and the pattern speed of the bar in the early type galaxy NGC 7079 (Debattista & Williams 2004).

In the present paper we use FP absorption line spectroscopy to obtain radial velocities using the Ca II λ8542 line for 2488 Red Clump Giants (RCGs), 339 red giants (M/K type) and 318 disk main sequence stars, towards three LOS in the MW bar: BW and two symmetric offset positions at $(l, b) \simeq (\pm 5.0, -3.5)^\circ$ (see Figure 2.1). This sample is an order of magnitude larger than any previous sample for a given LOS. We also measure equivalent widths of the Ca II λ8542 absorption lines that can be used to infer metallicities (e.g. Armandroff & Zinn 1988) for the late type stars. This will be the subject of a subsequent paper (Paper II) and is discussed only briefly here. In

Table 2.1 Sub-fields observed in the MW bar. Right ascension (α) and declination (δ) are from epoch J2000 and N_{stars} indicates the total number of stars (including foreground) obtained from each sub-field.

Field	Date Obs.	α	δ	$l(^\circ)$	$b(^\circ)$	N_{stars}
MM5B-a	1996	17:47:24.05	-35:00:21.07	-5.00	-3.47	472
MM5B-b	1997	17:47:40.03	-35:00:34.0	-4.97	-3.52	378
MM5B-c	1999	17:47:20.71	-35:56:52.84	-4.95	-3.43	608
MM5B-d	1997/99	17:47:39.80	-35:56:47.85	-4.92	-3.49	525
BWC-a	1999	18:03:39.70	-29:59:51.2	1.06	-3.93	718
BW1-a	1999	18:02:29.41	-29:49:27.4	1.09	-3.62	359
MM7B-a	1996	18:11:29.61	-25:54:06.6	5.50	-3.46	353
MM7B-b	1997	18:11:44.23	-25:54:26.0	5.52	-3.51	322
MM7B-c	1997/99	18:11:30.32	-25:50:38.5	5.55	-3.44	288
MM7B-d	1999	18:11:44.72	-25:50:33.4	5.58	-3.48	396

Paper III we will use our measurements for new, more detailed dynamical models of the MW bar.

2.2 Observations

Observations were made between 1996 and 1999 using the Rutgers Fabry-Pérot (RFP) system at the f/13.5 Cassegrain focus of the Cerro Tololo Inter-American Observatory (CTIO) 1.5m telescope. The field of view of the RFP was circular with a diameter of $4'$. The detector was a Tek 1024 x 1024 pixel CCD, giving an image scale of $0.36''$ per pixel. Typical seeing was in the range of $1'' - 1.5''$. Each narrow-band exposure was of 900 s duration. A typical image is shown in Figure 2.2. We observed three LOS: the MM5B field at l = -5°, the MM7B field at l = $+5^\circ$, and BW. There are four overlapping subfields in each of the MM5B and MM7B fields, as shown in Figure 2.1, and two sub-fields in BW. Table 2.1 lists the location of each sub-field and the total number of stars obtained per field. The choice and nomenclature of the fields was motivated by the OGLE survey (Udalski et al. 1992), which provides us with excellent I and V band stellar photometry. In total we obtained ~ 4400 stellar spectra.

We chose to observe the Ca II λ8542 spectral line. The calcium triplet (8498.02 Å,

8542.09 Å and 8662.14 Å) is one of the strongest near-infrared spectral features in late-type stars like the RCGs. The triplet arises from the transition between the two levels of 3^2D and the two levels of 4^2P in Ca II. The temperature of the bulk of the ISM is not high enough to excite Ca II to the 3^2D state, and therefore no contamination from the foreground ISM is expected. The 8542 Å line is the strongest of the triplet and falls in a wavelength region where the night sky is relatively free of strong terrestrial emission lines.

We used a medium-resolution etalon with a spectral response function that is well fit by a Voigt function with a FWHM of 4 Å, equivalent to approximately 140 km s^{-1} at 8500 Å. We typically scanned a range of $8530 - 8555$ Å with wavelength steps of 1 Å. The FP images are not monochromatic, because the rays from off-axis points pass through the collimated beam at an angle, making the passband shift to the blue towards the edge of the field. The scanning range was sufficient to compensate for the 4Å center-to-edge gradient by including extra images at the red end of the scan. The resulting spectra allowed measurement of the central wavelength of the line with high precision (5 – 10 km s^{-1}).

This project was plagued by bad weather and technical difficulties with the instrument and telescope, requiring a significantly longer period of time to acquire the data than expected. During two of the nights in the 1997 run the instrument shutter malfunctioned, affecting the data for sub-fields MM5B-b and MM7B-b, which upon reduction showed large deviations in kinematics compared to the neighboring fields that overlap with them. For this reason we excluded these two fields from our analysis. Because of time constraints only 18 images were obtained for the BW1-a field with heavy obscuration from clouds for half of them, and hence we also excluded this field. These exclusions brought the total sample size down to 3360 stars from seven sub-fields, of which 3144 are used in our kinematic analysis.

We calibrated the wavelength response of the system with several lines around

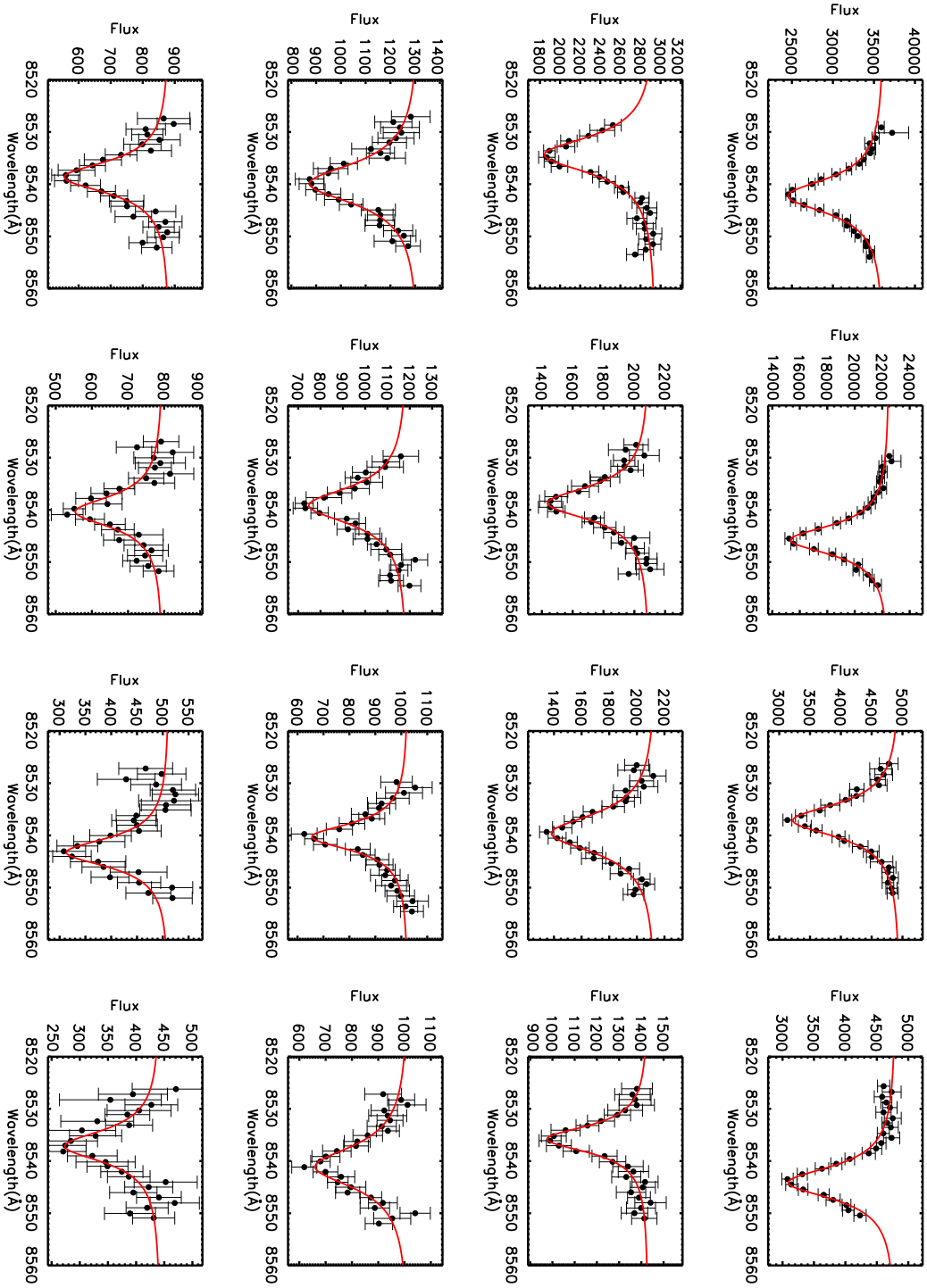

Figure 2.3 A sample of the Ca II λ8542 spectra for almost the entire brightness range of our sample from I-band magnitude of 11.0 to 16.5. Each data point on the absorption line comes from a single image in the data cube. The solid line is a Voigt fit to the spectrum.

8542 Å from a neon spectral lamp. The complete calibration sequence was done once per observing run, and was stable over the duration of the run (and indeed from year to year). The precision of the wavelength calibration was typically better than 0.05 Å, corresponding to 1.8 km s^{-1}at 8500 Å. The zero-point of the wavelength scale was affected by changes in the environmental conditions such as temperature and atmospheric pressure, and was monitored by taking a single neon calibration image once each hour during the observations. The wavelength zero-point for each observation image was determined by interpolation from these hourly calibrations. On images that have night sky lines within their spectral range, we can also use these sky lines to check the zero point. There were two weak OH lines (at 8548.71 Å & 8538.67 Å; Osterbrock & Martel (1992)) that fall within our scanning range. Although these lines had very low S/N, the zero-point we measured from them for a few frames was consistent with the interpolated calibration ring measurement.

2.3 Data Reduction

2.3.1 Fabry-Pérot Photometry

The images in each data cube are overscan corrected, trimmed and bias subtracted using IRAF[2]. To perform photometry on the individual images we use the DAOPHOT stand-alone package by Stetson (1987) that was specially developed to perform crowded field stellar photometry. The task FIND gives the initial centroids of all the stars in the field. After performing the initial aperture photometry using the PHOT task, PSF-based photometry is performed using a quadratically variable PSF, which we found to be especially useful at the edges of the field. We used about 50 – 100 stars per image to determine the PSF. The ALLSTAR task then simultaneously fits all of the stars in the image using the measured PSF to give a star subtracted image, and fluxes and

[2]IRAF is distributed by NOAO, which is operated by AURA, Inc., under a cooperative agreement with the NSF

positions for all stars. Because DAOPHOT performs local sky subtraction, the fluxes are not affected by the presence of the weak OH sky lines. DAOPHOT includes the ALLFRAME (Stetson 1994) program that is particularly useful for reducing a data cube. It simultaneously performs the PSF fitting for all stars in all the images of the cube to derive positions and magnitudes in a self-consistent manner, making use of the geometric transformations between the individual images and photometry information for all images. Because our fields are much less crowded than, for example, a globular cluster, DAOPHOT is able to resolve the stars easily. The final output of DAOPHOT are the centroids, fluxes (in arbitrary units) and flux uncertainty for each star.

2.3.2 Flux Normalization

In FP absorption line work, it is critically important to account for changes in flux due to variations in atmospheric transmission. This can be significant if the images of a spectral scan were taken over several nights or even in different years, or in non-photometric weather conditions. To measure the image-to-image normalization, we select about 30 high S/N stars uniformly covering the FOV, so that there is a range in velocity and wavelength coverage. We assume that all of these stars have a single dominant absorption line that is well represented by a Voigt function. We fit a Voigt profile to the spectrum of each star, and at each point calculate the ratio of the fit to the observed flux. For each image in the scan, we then calculate the mean and standard deviation of these ratios, using all of the normalization stars for that image. This ratio is the normalization factor for that image. If an image was taken in average transparency conditions, then its normalization factor should be 1.0, within the photometric uncertainty; if the image had lower transparency, the normalization will be greater than unity. We correct the fluxes for each image in the scan using the individual normalization factors. In order to determine the final normalization factors, we re-fit the profile to the normalized data, and iterate the entire process until it converges.

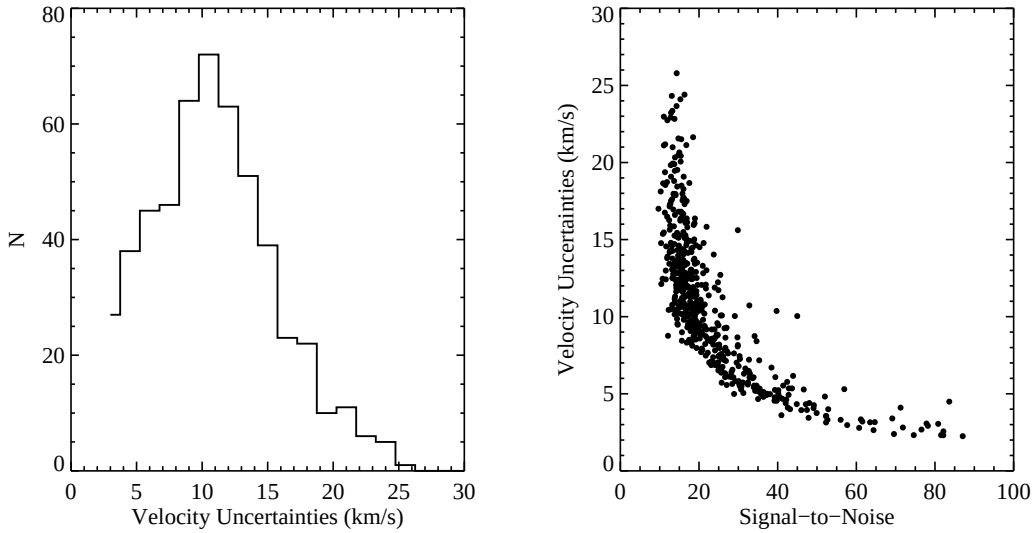

Figure 2.4 The distribution of velocity errors for the MM5B-c field (left panel) and velocity uncertainties as a function of signal-to-noise for the same field (right panel).

This procedure introduces an additional uncertainty in the flux measurement, which we call the 'normalization uncertainty'. We combine this in quadrature with the DAOPHOT flux uncertainties. For the highest S/N[3] ($\sim$ 80) stars the flux normalization error dominates, while for the majority of stars the DAOPHOT flux error is more important. Since the different normalization stars have a range of velocities, and also because of the center-to-edge wavelength gradient in a FP image, an individual image samples the stars at several different points on the line profile; this avoids "building in" a particular profile shape through the normalization factors. Under photometric conditions, the normalization factors were typically 1.00 ± 0.02, with uncertainties of $0.002 - 0.003$. In bad conditions, the worst normalizations were $1.5 - 2.0$, with uncertainties of ~ 0.01. We often re-observed at some of the wavelengths taken under poor conditions, and found excellent agreement between stellar fluxes after normalization.

[3]We define the S/N for an individual star as the mean ratio of the measured flux to the estimated flux uncertainty, averaged over all the points measured in the star's spectrum.

2.3.3 Spectroscopy

The Ca II λ8542 absorption line profiles with the combined uncertainties are fit with a Voigt function using the Levenberg-Marquardt method of least-squares fitting. The fit gives the central wavelength, continuum level, line strength, and the Gaussian and Lorentzian widths along with their measurement uncertainties. We find that the Gaussian contribution to the shape of the absorption line is negligible for the majority of stars and the line could be fit equally well by fixing the Gaussian width at 10^{-3} Å, using essentially a Lorentzian profile. This is because the instrumental profile itself is essentially Lorentzian with a negligible Gaussian core, and the Ca II λ8542 line in these stars is strongly saturated with damping wings from collisional broadening. Figure 3.2 shows a sub-sample of absorption lines covering almost the entire brightness range for our sample from I-band magnitude of 10.0 to 16.5. The Voigt fit is represented by the solid line. For the brightest stars the velocity uncertainties can be as low as 2 km s^{-1} and even for the very faint stars we can measure the absorption line adequately well with velocity uncertainties of 20 – 30 km s^{-1}.

2.4 Radial Velocities

Table 2.2 lists the heliocentric radial velocities and their uncertainties that we measured for our complete sample of 3360 stars with 1605 and 1037 stars at $l = \pm 5^{\circ}$, respectively, and 718 in BW. The median velocity error for our sample is $\sim$ 12 km s^{-1}. The uncertainties are higher for fainter stars and also in cases where a star has a close or unresolved neighbor. In Figure 2.4 we show the distribution of velocity errors and the error as a function of S/N for the MM5B-c subfield. The major source of error in the radial velocity measurements comes from the uncertainties in the flux measurements, which include contributions from DAOPHOT and normalization errors. In the case of very high S/N stars in the best seeing sub-fields like MM5B-c and BWC-a (with lower normalization errors) the velocity errors can be as small as 2 – 5 km s^{-1}.

Table 2.2 Radial Velocities and Equivalent Widths

ID	OGLEID	R.A. j2000	Dec. j2000	V km s^{-1}	$V_{\rm err}$ km s^{-1}	EW Å	EW$_{\rm err}$ Å	I	V-I	Source
BWCa-1	256217	18:03:35.16	-29:58:12.3	-4.49	1.60	4.64	0.17	11.560	2.117	o
BWCa-2	256200	18:03:31.91	-30:00:28.3	-27.71	2.55	2.12	0.12	11.523	3.960	o
BWCa-3	256193	18:03:31.67	-30:00:43.4	-44.86	1.91	4.55	0.19	11.730	2.522	o
BWCa-4	402256	18:03:43.52	-30:01:46.1	-17.77	1.70	4.34	0.15	11.733	1.358	o
BWCa-5	256201	18:03:30.78	-30:00:27.9	92.33	2.41	3.79	0.18	12.241	2.702	o
BWCa-6	256199	18:03:32.87	-30:00:31.4	9.84	3.60	2.42	0.20	12.098	0.710	o
BWCa-8	402258	18:03:45.27	-30:01:32.5	-74.90	3.48	2.94	0.22	12.214	3.876	o
BWCa-9	–	18:03:36.34	-30:01:50.2	-20.10	3.03	3.80	0.23	12.020	–	f
BWCa-11	244433	18:03:34.54	-30:01:37.6	32.20	3.41	1.20	0.11	12.229	4.566	o
BWCa-12	412692	18:03:38.98	-29:58:25.9	-38.04	2.72	5.65	0.31	12.215	2.595	o
BWCa-13	423223	18:03:41.96	-29:57:49.1	-70.86	2.80	4.07	0.25	12.289	2.120	o
BWCa-15	412682	18:03:38.18	-30:00:51.2	-16.60	2.91	4.07	0.23	12.467	1.912	o
BWCa-16	412681	18:03:38.24	-30:00:59.7	67.05	2.41	4.64	0.23	12.476	2.346	o
BWCa-19	412690	18:03:36.96	-29:58:47.1	-58.58	2.45	6.04	0.31	12.483	2.094	o
BWCa-20	256196	18:03:33.66	-30:00:36.1	-24.73	2.47	3.46	0.20	12.579	1.894	o
BWCa-21	412685	18:03:42.64	-30:00:06.5	131.70	3.01	4.69	0.32	12.493	2.927	o
BWCa-22	402257	18:03:37.71	-30:01:34.0	-15.85	2.90	3.79	0.22	12.637	2.040	o
BWCa-23	412683	18:03:47.96	-30:00:38.1	-17.18	3.30	4.40	0.32	12.627	2.948	o
BWCa-27	412719	18:03:39.69	-29:58:47.5	-108.48	3.33	6.48	0.35	12.787	2.576	o
BWCa-28	412708	18:03:49.05	-29:59:35.0	-7.34	2.95	5.23	0.35	12.905	2.475	o
BWCa-29	256222	18:03:34.70	-30:01:15.7	-18.07	3.08	3.48	0.23	12.923	1.883	o
BWCa-30	412702	18:03:37.64	-30:00:26.0	-45.72	6.02	3.66	0.41	12.877	0.925	o
BWCa-32	256236	18:03:34.96	-29:59:48.6	-76.35	5.27	4.78	0.45	12.982	3.493	o
BWCa-33	412727	18:03:45.61	-29:58:12.0	-132.32	3.95	4.81	0.40	13.174	2.579	o
BWCa-34	412711	18:03:41.51	-29:59:20.3	-134.86	3.59	4.75	0.26	13.081	2.852	o
BWCa-35	256235	18:03:30.56	-29:59:51.0	44.72	3.22	4.07	0.29	13.173	2.307	o
BWCa-36	256238	18:03:32.78	-29:59:39.1	143.70	2.71	4.15	0.27	13.132	2.736	o
BWCa-38	412728	18:03:42.44	-29:58:10.6	-168.91	3.82	5.29	0.34	13.205	2.625	o
BWCa-39	412712	18:03:47.60	-29:59:15.4	-65.47	3.57	5.50	0.38	13.223	2.865	o
BWCa-40	412718	18:03:38.12	-29:58:58.3	3.29	3.78	5.35	0.39	13.150	2.474	o
BWCa-42	412732	18:03:37.09	-29:57:56.3	4.77	3.54	2.35	0.22	13.133	1.571	o
BWCa-43	412724	18:03:39.04	-29:58:28.0	-153.07	4.33	5.49	0.39	13.173	1.917	o
BWCa-44	412704	18:03:38.05	-30:00:10.2	-61.60	4.52	3.80	0.27	13.141	1.419	o
BWCa-45	412716	18:03:47.48	-29:59:06.4	110.99	2.89	4.14	0.28	13.309	2.530	o
BWCa-46	412699	18:03:46.37	-30:00:47.9	-130.64	3.93	4.99	0.36	13.333	2.210	o
BWCa-47	412720	18:03:45.08	-29:58:46.3	89.38	3.35	4.34	0.31	13.284	2.242	o
BWCa-48	402288	18:03:40.62	-30:01:46.0	-10.80	4.33	3.03	0.30	13.377	1.751	o
BWCa-49	412729	18:03:39.95	-29:58:07.8	-102.93	4.34	4.77	0.37	13.295	1.956	o
BWCa-50	256226	18:03:36.45	-30:00:39.8	-13.72	3.74	5.04	0.39	13.311	2.713	o

Note. — Table 2.2 is published in its entirety in the electronic edition of the *Astrophysical Journal*. A portion is shown here for guidance regarding its form and content.

[a]Source of Photometry: 'o' for OGLE, 's' for SAAO and 'f' for fabry-pérot

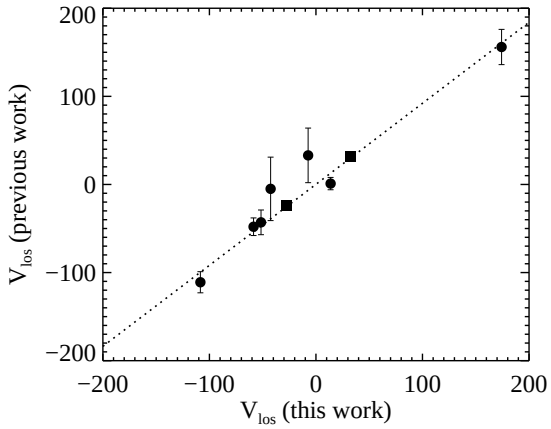

Figure 2.5 Radial velocities of 9 stars in common between this work and previous measurements by Sharples et al. (1990) (squares) and Terndrup et al. (1995) (circles).

To check if the velocity errors obtained from our Voigt fitter are reasonable, we carried out Monte Carlo simulations of the data. For each star in our sample, we generated 1000 random realizations of its spectrum by perturbing the fluxes of each point of the Voigt profile fit by the corresponding $1-\sigma$ individual flux uncertainty. We then fit a Voigt function to each of these generated spectra and find that the mean ratio of the error estimate from a single fit to the standard deviation of the velocities from the Monte Carlo fits is about 0.97 for all the fields, indicating that the single fit errors from our Voigt fitter code are reliable.

For the BW LOS, there are nine bulge M/K-giant stars in our work that are also present in the radial velocity samples of Sharples et al. (1990) and Terndrup et al. (1995). The velocity comparison is shown in Figure 2.5. Our error bars on the horizontal axis are equal to or smaller than the size of the data points. Our velocities agree very well with the previous measurements, with a reduced chi-square of 1.02.

We also have two measurements (repeated over 1 – 3 years) of the radial velocities for some stars in the region where the fields at a given LOS overlap with each other. The comparison between the velocities of stars in these overlapping regions is shown in Figure 2.6 where the vertical axis shows the velocity difference divided by the 1σ

error bars (Δ). The dashed, dotted and dot-dashed lines show the 1σ, 2σ and 3σ limits respectively. The stars at the very edge of the field in the overlapping regions may not show up in every image taken in the scan of that field, so they are not included in this comparison. There is also a 10% chance for a foreground disk main sequence star to be a spectroscopic binary which may result in velocity variations of $\lesssim 30$ km s^{-1} (Duquennoy & Mayor 1991). We find three such examples of foreground stars with large velocity differences in the overlapping regions, and these three stars are omitted from Figure 2.6. The comparison for the MM5B overlapping regions has a reduced chi-square of $\lesssim 1$. There is one additional star (not foreground) in each of the two overlapping regions of the MM7B fields that has a deviation of more than 3σ, inflating the reduced chi-square for these fields. We don't have a clear explanation for the deviations in these two cases except that they could be spectroscopic binaries in the bulge. The reduced chi-square for all the stars in the MM7B fields is 1.6; excluding the two outliers reduces chi-square to 1.06.

For most of the stars in the overlapping region we list the weighted mean velocity and errors in Table 2.2. For the faintest stars from the overlapping regions, we use the velocity from only the field with the best image quality, where the fit to the absorption line was significantly better than the other field. The comparison with previous work, and in the overlapping regions, indicates that our velocity measurements are repeatable and reliable. The velocity uncertainty of less than 30 km s^{-1} is small compared to the velocity dispersion of the stars in the bar, and will have no effect on our conclusions.

2.5 Photometry and Astrometry

We use photometric information to distinguish between the foreground disk stars, bulge red giants and bulge RCGs. Since our observed fields are coincident with the OGLE

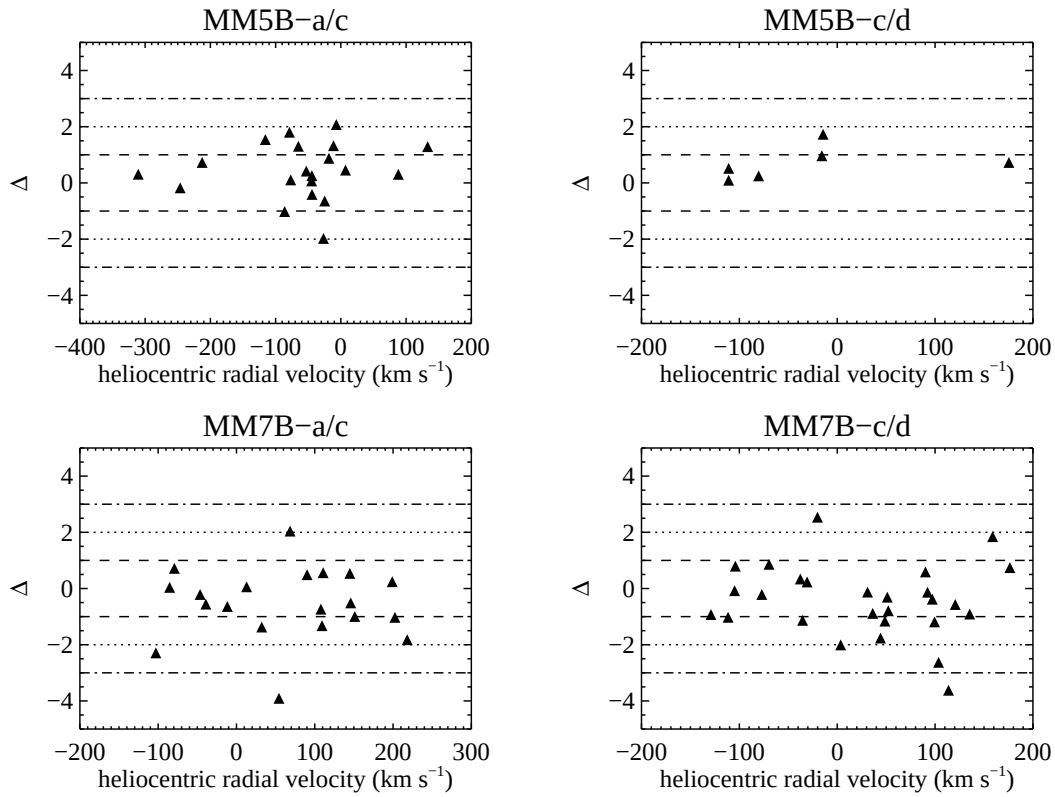

Figure 2.6 Repeated radial velocity measurements of stars in the overlapping regions of the sub-fields of MM5B and MM7B.

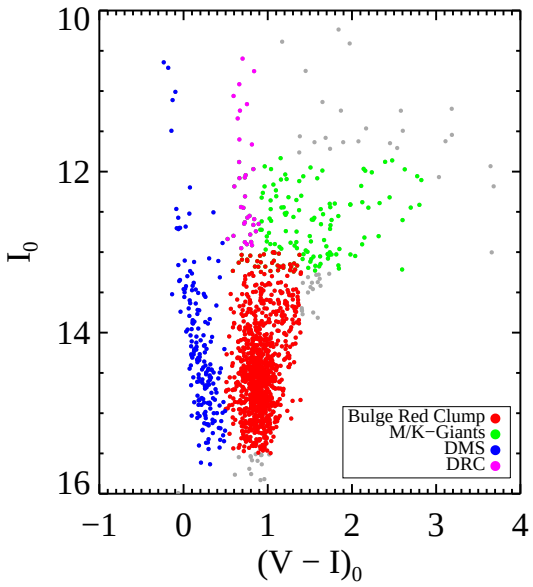

Figure 2.7 Extinction-corrected color-Magnitude diagram for the MM5B LOS shows a distinct red clump (red dots). The disk main sequence and the M/K – giants are shown in blue and green dots respectively. We measure the radial velocity of every star in the diagram.

survey, we have precision (1 – 2%) V and I band photometry and astrometry[4] (Szymanski 2005). Unfortunately, the fields MM7B-d and a quarter of MM7B-c fell outside the OGLE field. Photometric observations for these fields were obtained with the 1-m telescope at the South African Astronomical Observatory (SAAO). Reduction of these data using the IRAF photometry package gives V and I band magnitudes with an accuracy of 5% – 10%.

There are some stars in our sample that have no OGLE or SAAO photometry. For these stars we use the FP measurement of the continuum level of the Ca II λ8542 absorption line to estimate I-band magnitudes. To check the accuracy of these FP I-band magnitudes we use all the stars in the MM7Bc field where we have both OGLE and SAAO photometry. We determine the zero point of the FP I-band magnitudes from the OGLE photometry for these stars. We compare them to the OGLE and

[4]http://ogledb.astrouw.edu.pl/∼ogle/photdb/

the SAAO magnitudes to find that they are surprisingly consistent with differences $\lesssim 10\%$. These FP I-band magnitudes are used to exclude foreground stars as discussed in section 6. Comparison with the much deeper OGLE survey shows that our sample of RCGs in the bar is essentially complete. Table 2.2 lists the astrometry and photometry. The photometry source (OGLE, SAAO or FP) is indicated in the last column. The astrometry for all fields comes from OGLE except for the field MM7B-d where the source is the Digitized Sky Survey.

2.6 Selections from the Color-Magnitude Diagram

The color-magnitude diagram (CMD) is shown in Figure 2.7 for the MM5B field with 1605 stars. We chose to show the CMD for this particular LOS since it has the largest number of stars and also has OGLE photometry for all them. The CMDs for the other two LOS look almost identical. Paczynski et al. (1994) discuss various parts and features of the BW CMD using the photometry of about 3×10^5 stars from the OGLE project. We discuss in brief these features and their selection limits in the $(I_0, (V-I)_0)$ plane to be used in our analysis.

The first feature is a distinct red clump, marked by the red points. These RCGs are very useful candidates for studying the kinematics of the bar. They are basically metal-rich counterparts of the horizontal branch stars burning helium in their cores and hydrogen in their envelopes. Their intrinsic luminosity distribution is very narrow and has a weak dependence on metallicity and age, making them excellent distance indicators (Paczynski & Stanek 1998). They are bright and numerous in the inner galaxy and are located in the region of CMD that is least contaminated by disk stars (Stanek et al. 1994).

Our selection limits for RCGs towards all three LOS are $(I_0, (V-I)_0) = (13.0 - 15.5, 0.5 - 1.4)$, corrected for the extinction (A_I) and reddening (E_{V-I}) values from Sumi (2004). This I-band limit corresponds to a distance range of about 5.5 – 13

kpc for intrinsic red clump magnitude $M_I = -0.28 \pm 0.20$ (Paczynski & Stanek 1998). Stanek et al. (1997) used a slightly different selection criteria for OGLE RCGs where they define extinction independent I-band magnitudes. The effect of these two different selection methods on the overall kinematics of the RCGs is negligible, with changes in the mean radial velocity and dispersion of about 0.75 km s^{-1} and 1.15 km s^{-1} respectively. The latter selection also gives 2% fewer stars at $l = \pm 5°$and 10% fewer stars in BW. We have also investigated the effect of varying the brighter end of the I-band selection limit from 13.0 – 13.6 magnitudes, which produced negligible changes to the mean velocity and dispersion ($\sim$ 0.5 km s^{-1}). The effects of different selection criteria for RCGs will be more significant when modeling the data (subject of paper III), where it will be investigated in greater detail.

About 210 stars at $(l, b) = (\pm 5.0, -3.5)°$and 39 in BW have only I-band photometry. Without color information it is not possible to distinguish them from the foreground disk stars (blue points in Figure 2.7). If we apply only I-band cuts then the maximum difference in the kinematics between including or excluding these stars without color information is about 1.3 km s^{-1} in mean velocity and 0.6 km s^{-1} in dispersion. The 2MASS point source catalogue has J, H and K band photometry for our lines of sight. We found J-K colors for 60% of these stars with no V-I color information. The J-K colors confirmed that after applying the I-band or distance cut about 96% of these stars were RCGs. By analyzing the field MM7B-c, where 99% of the sample has complete V and I band photometry, we find that the contamination due to lack of color information is $\sim$ 14%, after applying the I-band or distance cut. This amounts to contamination by only 11 stars at $l = \pm 5°$and 2 stars in BW. These numbers are negligible compared to the overall sample size and will have little effect on the kinematics. Thus we include these stars (with just the I-band limits) in our final sample that will be used to measure bar kinematics, which now has a total of 1193 RCGs at $(l, b) = (-5.0, -3.5)°$, 738 at $(l, b) = (5.5, -3.5)°$and 557 in BW.

The region marked by the green points at roughly $(I_0, (V-I)_0) = (11.8-13.25, 0.5-3.0)$ contains the bulge M/K-giants (Sharples et al. 1990; Terndrup et al. 1995). This is the same M-giant population used in the recent radial velocity survey by Rich et al. (2007). In section 7.2 we use them to make a direct comparison with that study. This sample, measured simultaneously from the same data cube, allows us to compare the kinematics of two different stellar populations in the bar/bulge region.

The feature marked by the blue points at $(I_0, (V-I)_0) = (10.0-15.7, -0.3-0.5)$ is formed by the disk main sequence (DMS) stars. The stars in this feature are thought to be associated with the Sagittarius spiral arm located at $\sim$ 2 kpc from the Sun (Paczynski et al. 1994; Ng et al. 1996). We have radial velocities of about 350 stars in this region over three LOS. This feature and its possible association with the Sagittarius arm is discussed in section 7.3.

Finally, the feature at $(I_0, (V-I)_0) = (10.0-13.0, 0.5-0.9)^5$ on the CMD marked by the magenta points consists of the disk red clump giants spread over a distance of about 1.0 – 4.0 kpc. We had just enough stars in our sample along this LOS to detect this feature and measure its kinematics. The FP imaging spectroscopy has allowed us to measure simultaneously the kinematics of all these features, providing a powerful and reliable way to look for differences between the various stellar populations in a consistent manner.

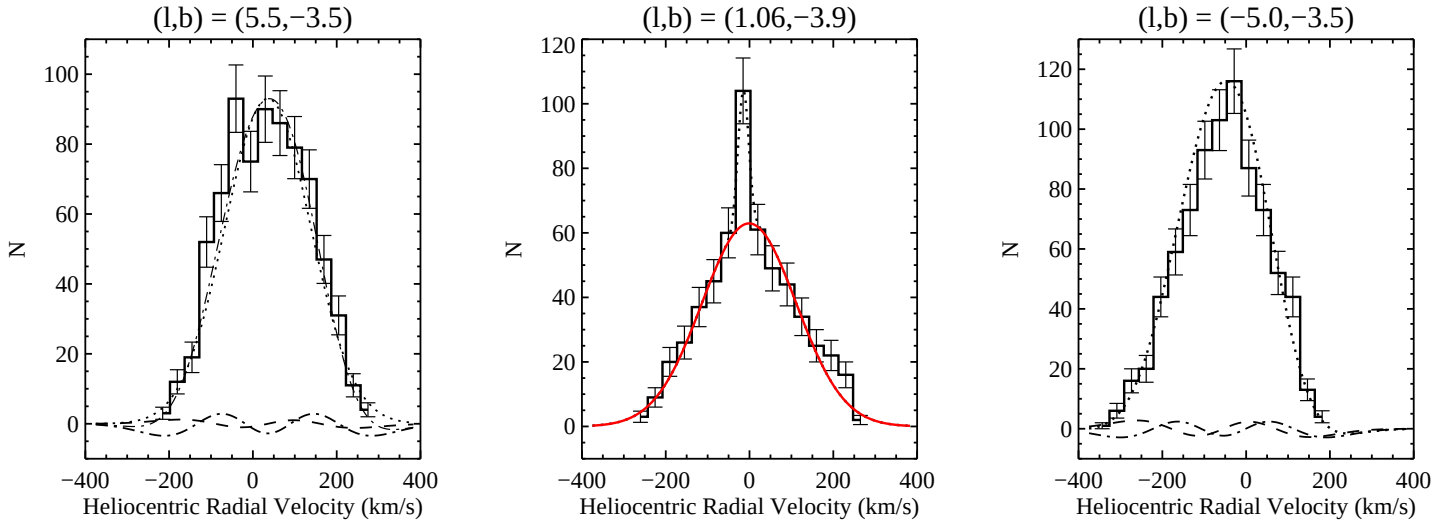

Figure 2.8 Stellar radial velocity distribution for three LOS in the bar. Right and Left panel: the dotted line is the Gauss-Hermite fit with h_3 and h_4 moments shown by dashed and dot-dashed lines respectively. Middle panel: the dotted line is double Gaussian with a narrow component for the globular cluster NGC 6522 and the solid line is the broad component (only) for the Galactic bar/bulge.

Table 2.3 Heliocentric kinematics of the red clump giants for three LOS in the Milky Way bar.

Method	$< V_{\rm los} >$ (km s^{-1})	$\sigma_{\rm los}$ (km s^{-1})	h_3 (km s^{-1})	h_4 (km s^{-1})
MM5B-(a+c); $(l, b) = (-5.0, -3.5)$; $N_{\rm stars} = 804$				
Likelihood	$-54.15 \pm 3.66\,(\pm 6.14)$	$101.72 \pm 0.66\,(\pm 0.80)$	$-0.030 \pm 0.017\,(\pm 0.034)$	$-0.032 \pm 0.008\,(\pm 0.017)$
Biweight	$-52.56 \pm 0.60\,(\pm 3.85)$	$102.30 \pm 1.25\,(\pm 2.50)$	$\cdots$	$\cdots$
Likelihood	$-56.46 \pm 1.84\,(\pm 4.48)$	$102.04 \pm 0.09\,(\pm 0.28)$	$-0.018 \pm 0.007\,(\pm 0.018)$	$-0.031 \pm 0.005\,(\pm 0.012)$
Biweight	$-58.57 \pm 0.48\,(\pm 3.35)$	$101.46 \pm 1.21\,(\pm 2.03)$	$\cdots$	$\cdots$
MM7B-(a+c+d); $(l, b) = (5.5, -3.5)$; $N_{\rm stars} = 738$				
Likelihood	$35.73 \pm 7.20\,(\pm 9.44)$	$102.40 \pm 0.15\,(\pm 0.31)$	$-0.016 \pm 0.031\,(\pm 0.043)$	$-0.047 \pm 0.022\,(\pm 0.026)$
Biweight	$30.73 \pm 0.58\,(\pm 3.89)$	$102.38 \pm 1.21\,(\pm 2.39)$	$\cdots$	$\cdots$
BWC-a; $(l, b) = (1.06, -3.9)$; $N_{\rm stars} = 557$				
Likelihood	$4.32 \pm 0.26\,(\pm 5.21)$	$110.29 \pm 0.36\,(\pm 0.73)$	$-0.031 \pm 0.011\,(\pm 0.019)$	$-0.035 \pm 0.009\,(\pm 0.017)$
BW (B)	-1.01 ± 5.42	112.62 ± 3.41	$\cdots$	$\cdots$
NGC 6522 (N)	-14.67 ± 3.77	7.9 ± 2.82		

2.7 Kinematics

2.7.1 Kinematics of Red Clump Giants in the Bar: Measurement of h_3 and h_4

The large size of our sample allows us to measure, for the first time, the higher moments of the velocity distribution along our three LOS. We fit a Gauss-Hermite series to the velocity distribution (Gerhard 1993; van der Marel & Franx 1993) of RCGs to extract the four velocity moments – mean line of sight velocity ($< V_{\rm los} >$), line-of-sight velocity dispersion ($\sigma_{\rm los}$), asymmetry of the distribution (h_3), and flatness of the distribution (h_4) – using a maximum likelihood estimator (MLE). An advantage of using the MLE is that it corrects for the individual velocity errors that can broaden the width of the distribution. We use the MLE code developed by Glenn Van de Ven (private communication; see van de Ven et al. (2006) for more details) to fit a Gauss-Hermite series to our velocity distributions and to determine the velocity moments. The code gives a robust measurement of the uncertainties of each moment in two ways. The bootstrap method randomly draws from the observed velocity distribution with replacement (see Sect. 15.6 of Press et al. 1992); this gives the maximum possible errors of the parameters. The Gaussian randomization (GR) method randomly draws velocities from an intrinsic Gaussian distribution with a given mean and dispersion that is broadened by velocity errors randomly drawn from the observed velocity error distribution (see Appendix B of van de Ven et al. 2006). GR gives reliable estimates if the individual errors are not underestimated, which we believe is the case with our analysis. Finally, the code uses the biweight statistic to measure just the first two velocity moments ($< V_{\rm los} >$ and $\sigma_{\rm los}$) and their uncertainties; these are the appropriate measures to compare with previous investigations that had too few stars to reliably

[5]Note that there is an overlap in the selection limits between other features and the M-giant sample. We chose the selection of the M-giants to be as close as possible to that used in previous investigations, in order to make kinematic comparisons.

determine the higher moments.

MM5B-a and MM5B-c have identical kinematics and can be combined into a single field MM5B-(a+c). MM5B-d is at the same LOS and overlaps with the MM5B-c sub-field but has a mean velocity that is offset by 13 km s^{-1} (i.e. about a 2σ deviation). The dispersions in all three sub-fields however agree within the 1σ errors. For this reason we measure the velocity moments at $l = -5.0^{\circ}$ using both MM5B-(a+c) as well as the three sub-fields combined MM5B-(a+c+d). There are no significant differences in the kinematics of sub-fields MM7B-a, MM7B-c and MM7B-d, so they are combined into a single field MM7B-(a+c+d). The velocity distributions for MM5B-(a+c) and MM7B-(a+c+d) are shown in the left and right panel of Figure 2.8. The dotted line is the Gauss-Hermite fit with the h_3 and h_4 moments represented by the dashed and dot-dashed lines respectively. Table 2.3 lists the velocity moments along with their uncertainties. Our large sample size allows us to measure $< V_{\rm los} >$ and $\sigma_{\rm los}$ with high accuracy. As expected, in Galactocentric coordinates $< V_{\rm los} >$ has equal amplitude of about ± 63 km s^{-1} at $l = \pm 5^{\circ}$, respectively. The h_4 moment is significantly non-zero while the h_3 is consistent with zero. Our high S/N velocity distributions show no sign of cold kinematic features that could be related to disrupted satellites, as suggested by Rich et al. (2007).

The analysis of the BW velocity distribution (middle panel) is slightly complicated by the presence of stars from the bulge globular cluster NGC 6522, the outskirts of which extend into the southwest edge of our field (see Figure 2.2). The spike at the center of the BW velocity distribution (shown in Figure 2.8 middle panel) is caused by the stars that are part of this cluster. To extract kinematics we fit a double Gaussian (broad for the bulge and narrow for NGC 6522) to this distribution. The narrow Gaussian has a mean velocity of -14.67 ± 3.77 km s^{-1} and dispersion of 7.9 ± 2.82 km s^{-1} ; consistent with previous measurements for NGC 6522 of -10.3 ± 1.6 km s^{-1} and $7.3^{+3.5}_{-2.0}$ km s^{-1} respectively (Dubath et al. 1997). The dotted line in Figure 2.8 shows the double

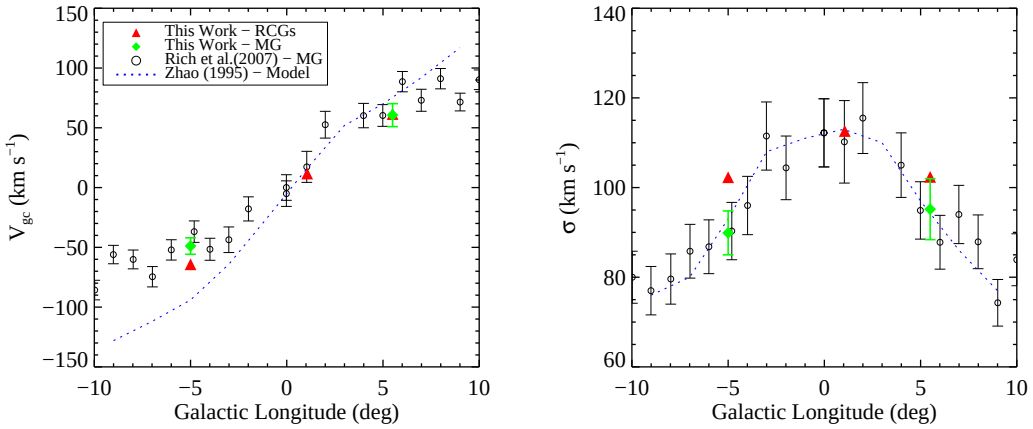

Figure 2.9 Comparison of the kinematics (in galactocentric frame) of RCGs (red triangles) and M-giants (green diamonds) from our sample to Rich et al. (2007) data (open circles) and Zhao (1996) model (blue dashed line)

gaussian fit to the distribution and the solid line is the broad component representing the bulge velocity distribution. We also fit a Gauss-Hermite series to this distribution and list the values in Table 2.3, although this measurement is most probably affected by the presence of the spike at the center. Since this is the most heavily studied LOS, there are several measurements of the kinematics in BW for comparison. Our values of the mean line-of-sight velocity and dispersion are in excellent agreement with all previous measurements of the kinematics in BW such as Mould (1983) ($< V_{\rm los} >= -10 \pm 19$ km s^{-1}, $\sigma_{\rm los} = 113 \pm 11$ km s^{-1}), Sharples et al. (1990) ($< V_{\rm los} >= 4 \pm 8$ km s^{-1}, $\sigma_{\rm los} = 113^{+6}_{-5}$ km s^{-1}), Rich (1990) ($< V_{\rm los} >= -13 \pm 12$ km s^{-1}, $\sigma_{\rm los} = 111 \pm 8$ km s^{-1}), Terndrup et al. (1995) ($< V_{\rm los} >= -8 \pm 6$ km s^{-1}, $\sigma_{\rm los} = 110 \pm 10$ km s^{-1}) and Rich et al. (2007) ($< V_{\rm los} >= -1.1 \pm 12.9$ km s^{-1}, $\sigma_{\rm los} = 110.2 \pm 9.1$ km s^{-1}).

2.7.2 Kinematics of M-giants

Our measurements of the kinematics of M-giants (in the heliocentric coordinate system) are listed in Table 2.4. We do not tabulate the measurements for BW since the globular cluster M-giants dominate the already small sample, and are difficult to separate from

Table 2.4 Kinematics of bar M-giants and disk main sequence stars

LOS	$< V_{\rm los} >$ ($\rm km\,s^{-1}$)	$\sigma_{\rm los}$ ($\rm km\,s^{-1}$)	N
M-giants			
(-5.0, -3.5)	-37.2 ± 6.9	89.9 ± 4.9	171
(5.5, -3.5)	29.9 ± 9.6	95.2 ± 6.8	98
DMS			
(-5.0, -3.5)	-17.8 ± 4.0	45.9 ± 2.8	134
(1.06, -3.9)	-3.1 ± 4.8	41.3 ± 3.4	75
(5.5, -3.5)	0.9 ± 4.3	45.7 ± 3.1	109

Note. — There are two types of errors for the velocity moments: Gaussian randomization and bootstrap (in parenthesis).
For BW kinematics the B and N stand for the broad and narrow Gaussian components.

the bulge population, making the measurement unreliable. In Figure 2.9 we compare the kinematics of the bulge RCGs and M-giants from our sample with that of Rich et al. (2007) M-giants and Zhao (1996) (Zhao hereafter) model. We find that the radial velocities of the RCGs and M-giants stars agree well with each other and with the Rich et al. (2007) measurements. However the LOS dispersion for our M-giant sample (green diamonds) is systematically lower than the RCGs (red triangles), and is consistent with the velocity dispersion of Rich et al. (2007) M-giants (black circles). Note that the higher dispersion of the RCGs in our sample is not because they are fainter and thus have somewhat larger velocity uncertainties. The MLE method we use removes the effects of the uncertainties from the estimate of the dispersion. In any event, to produce the difference between the M-giant and the RCG dispersion would require addition in quadrature of 40 – 50 km $\rm s^{-1}$ compared to the uncertainties of 10 – 25 km $\rm s^{-1}$.

The blue dashed line in Figure 2.9 is the prediction from Zhao's model. The bar in this model rotates faster than the observed rotation curve at greater longitudes. According to Zhao and Rich et al. (2007) this rapid rotation is due to a lack of retrograde orbits in the model. But adding retrograde orbits will increase the $\sigma_{\rm los}$ of the model,

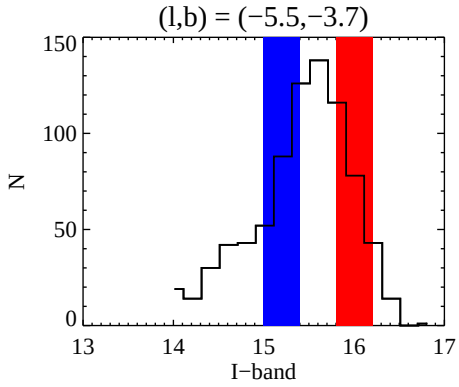

Figure 2.10 I-band apparent magnitude distribution of the red clump giants in MM5B field. The two bands show the sample limits for stars on the near and far sides of the bar.

which may then agree with the dispersion of RCGs rather than that of the M-giants.

Is there really a difference in dispersion between the M-giants and RCGs? One possibility is that the M-giant sample may have more foreground contamination, which could cause the observed decrement in the dispersion. However, our M-giant selection criteria are virtually the same as those of Rich et al. (2007), who argue that contamination is negligible. If the difference is real, then perhaps there is an age difference between the RCGs and the M-giants, with RCG's being older. Another possibility is that the M-giants represent multiple dynamical populations. But at this point we have no means to distinguish between these or other hypotheses. We plan to obtain more lines-of-sight in the bar using the FP system (Rangwala et al. 2008) on the 10-m Southern African Large Telescope (SALT) (Buckley et al. 2003) to explore this discrepancy further.

2.7.3 Kinematics of Disk Stars

Our measurements of the kinematics of the DMS stars (blue dots in figure 2.7) are listed in Table 2.4. Earlier studies of the Baade's window CMD (Terndrup et al. 1995; Paczynski et al. 1994; Ng et al. 1996) found an excess of stars within 2.5 kpc of the

Sun. They associated this increased stellar density (by a factor ~ 2) of DMS stars with the location of the Sagittarius spiral arm at a distance of ~ 2 kpc. The simulations performed by Ng et al. (1996) showed this density enhanced feature to consist of some very young stars (0.1 – 2.0 Gyr) that are identified with the recent spiral arm population superimposed on a larger population of young and intermediate age (2.0 – 7.0 Gyr) stars identified with some past spiral arm population. We find the $\sigma_{\rm los}$ to be the same ($\sim$ 45 km s^{-1}) towards all three LOS. According to the relationship between velocity dispersion and distance from the Galactic center (Lewis & Freeman 1989), our dispersion corresponds to a position within 3.5 kpc of the Sun. This suggests that the majority of the stars in this feature may belong to the Sagittarius spiral arm population.

The dispersion of the disk red clump feature (Magenta points on the CMD) is about 53 km s^{-1}, consistent with the disk kinematics.

2.8 Radial Streaming Motion

Previous observations have established that the near end of the Galactic bar is in the first Galactic quadrant, i.e., at positive longitudes. Since the stars forming the bar stream in the same sense as the Galactic rotation, for this bar orientation the stars on the near and far side of the bar will have radial velocity components towards and away from us, respectively. The radial velocity difference between these approaching and receding stellar streams depends on the orientation of the bar, among other things. Since RCGs are good distance indicators with a small dispersion in intrinsic luminosity, they can be localized in space and used to measure precisely the velocity shift between the two streams (Mao & Paczyński (2002); MP02 hereafter). This measurement will provide an additional strong constraint on the dynamical models of the Galactic bar, especially its orientation angle.

MP02 discuss the optimal selection of the bright and faint samples to isolate these

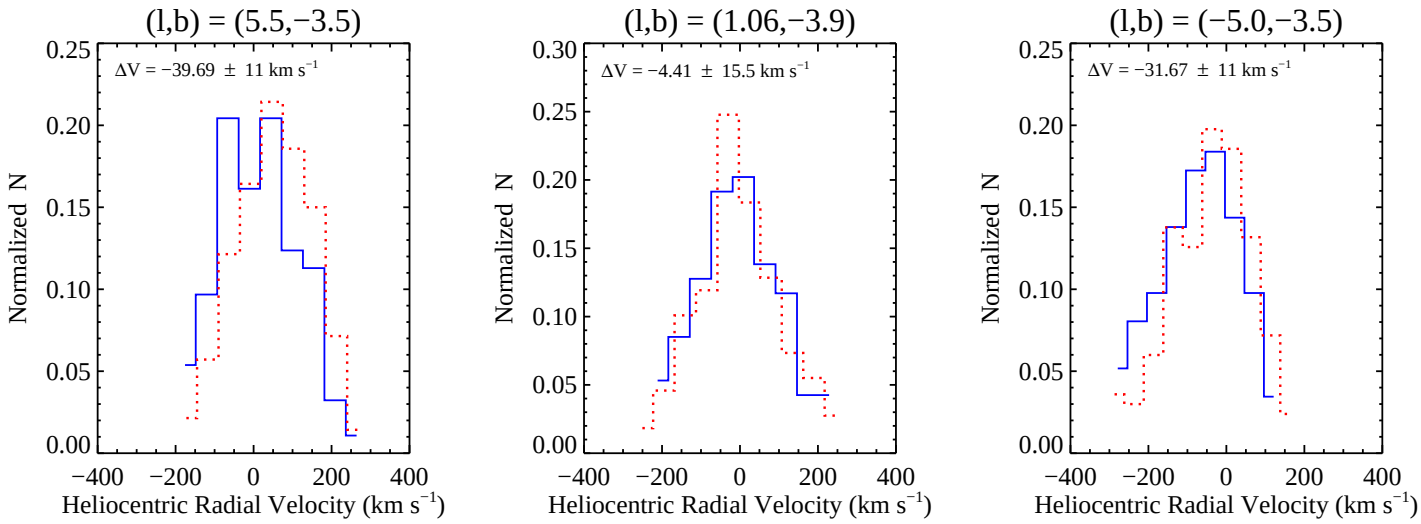

Figure 2.11 The radial velocity distribution for the stars in the near and far side samples, shown by the solid and dotted histograms respectively.

Table 2.5 Radial Streaming Motions.

LOS (l,b)	I_{peak}	$\langle V_{bright} \rangle$ km s^{-1}	N_{bright}	$\langle V_{faint} \rangle$ km s^{-1}	N_{faint}	ΔV km s^{-1}
$(+5.5, -3.5)$	15.4	13.57 ± 7.5	186	52.90 ± 8.3	140	-39.69 ± 11.2
$(+1.06, -3.9)$	15.2	-7.05 ± 11.3	94	-2.64 ± 10.7	109	-4.41 ± 15.5
$(-5.0, -3.5)$	15.6	-73.48 ± 8.1	174	41.81 ± 8.1	167	-31.67 ± 11.5

stellar streams. We adapt their criteria for the characteristics of our data set, selecting RCGs 0.2 to 0.6 magnitudes brighter and fainter than the peak in the observed luminosity distribution for each field to define the bright (front side) and faint (back side), respectively. Figure 2.10 illustrates the two samples for the $l = -5.0^\circ$ field, and the details of these bright and faint samples for the three LOS are listed in Table 2.5. Figure 2.11 shows the velocity distribution of the near and far side samples. We detect a clear velocity shift of ~ 35 km s^{-1} in each of $l \simeq \pm 5^\circ$ LOS. The velocity shift in BW is much smaller and is consistent with zero. This may be because in BW we are seeing an older spheroidal bulge population superimposed on the bar population, masking this signal. The higher velocity dispersion in BW also indicates that there are higher random motions compared to the streaming motions. Our observed shifts of 35 km s^{-1} are much greater than any possible projection effects arising from the Galactic rotation and the location of the near and far samples (1 – 2 km s^{-1}). This suggests that there are strong non-circular streaming motions associated with the bar. MP02 predicted the difference of the LOS component of the streaming motions between the bright and faint sample to be ~ 33 km s^{-1} based on the E2 model of Dwek et al. (1995). This predicted shift is consistent with our measurements in the $l = \pm 5^\circ$ fields but not in BW. MP02 also discussed the effects of red giant contamination on these shifts and concluded that their presence in the RCG sample could significantly dilute the magnitude of the velocity shifts, so that the actual shifts could be larger than those that we measure.

Deguchi et al. (2001) (see also Deguchi 2001) used SiO masers in the bar to measure the velocity shifts. They find an average radial velocity difference of -21 ± 27 km s^{-1} for sources with distances less than 7 kpc compared to those at distances greater than 7 kpc, essentially independent of longitude. While their results agree with our measurements, they suffer from a large (50%) uncertainty in distance and large statistical errors in kinematics (due to a smaller sample size).

As pointed out by Deguchi et al. (2001) most of the dynamical models of the inner galaxy do not predict or even discuss the change in average radial velocity with distance. The dynamical model of Häfner et al. (2000) was one of the first to discuss this in some detail. In their Figures 9 and 10 they plot line-of-sight and proper motion kinematics as a function of distance for four windows, one of which is BW. We have a large enough sample of RCGs to plot LOS average velocity and dispersion as a function of distance in the inner galaxy, which we show in Figure 2.12. Although we cannot make an exact comparison with Hafner's predictions for BW since they use a generic selection function for K giants, our data are nonetheless in excellent agreement with their model (open diamonds in Figure 2.12).

2.9 Equivalent Widths

Table 2.2 lists the equivalent widths and their uncertainties for our complete sample of 3360 stars. We measured the equivalent widths of Ca II λ8542 lines in our sample by integrating the Voigt fit over all wavelengths. Our measurements of mean equivalent width and dispersion for the bulge RCGs are listed in Table 3.1. The mean equivalent width ($<$ EW $>$) and its dispersion decrease on either side of BW similar to the LOS velocity dispersion. Because the Ca II λ8542 line is a good proxy for metallicity (Armandroff & Zinn 1988), the gradient in the mean equivalent width may imply a gradient in metallicity (Frogel 1988; Minniti et al. 1995) along the Galactic bar. We also find that the mean EW of the DMS stars is about 25% lower than the bulge RCGs,

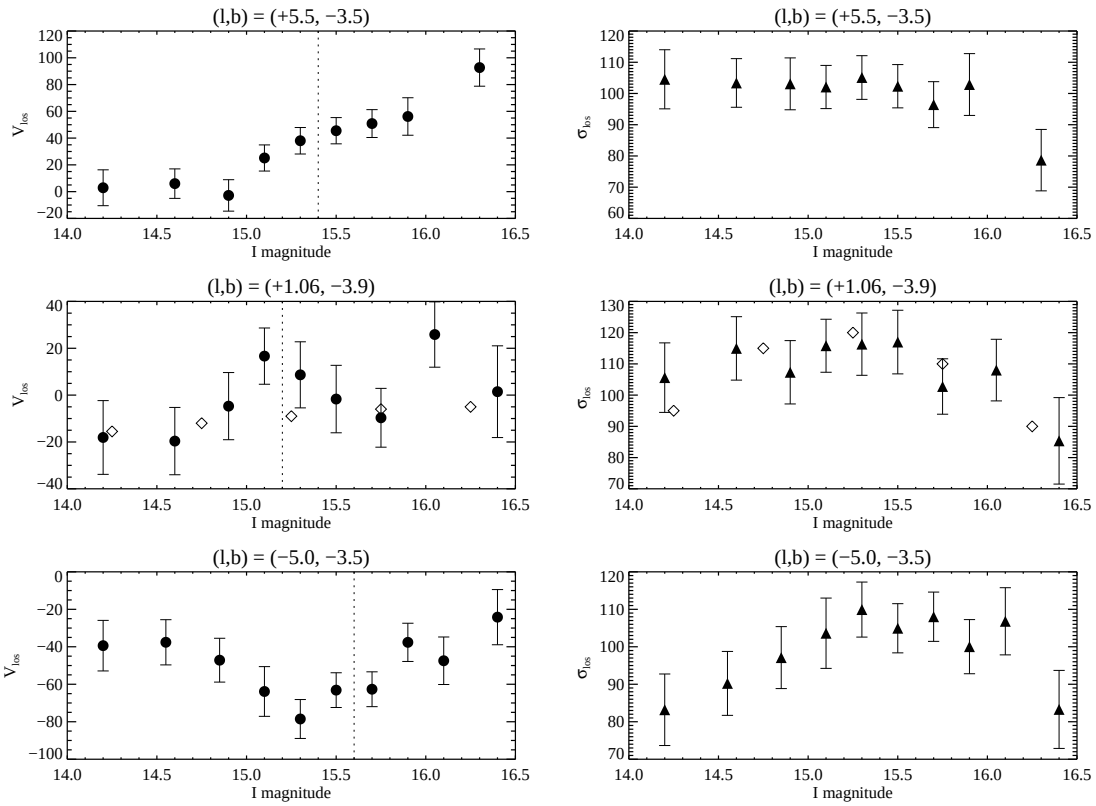

Figure 2.12 Line-of-sight radial velocity and dispersion as a function of I-band magnitude (or distance) of the bulge red clump giants for three LOS in the Galactic bar. The vertical dashed line shows the position of the peak magnitude about which the bright and faint samples were measured. Note that these are apparent magnitude not corrected for extinction. The open diamonds show Häfner et al. (2000)'s dynamical model.

Table 2.6 Mean equivalent width and dispersion for the Ca II λ8542 line in the bar RCGs

LOS	$<$ EW $>$ Å	$\sigma_{\rm EW}$ Å	N
(-5.0,-3.5)	3.68 ± 0.04	0.46 ± 0.04	804
(1.1,-3.9)	3.86 ± 0.05	0.68 ± 0.04	557
(5.5,-3.5)	3.28 ± 0.04	0.48 ± 0.04	738

which is consistent with a bulge that is more metal rich than the solar neighborhood. This has been the consensus of many previous studies in BW, for example Rich (1988). The factors affecting the measurement of FP equivalent widths and inferring [Fe/H] using the calcium infrared triplet method is addressed in detail in Paper II. For recent work on the metallicity of the Galactic bulge see Fulbright et al. (2006); Minniti & Zoccali (2008).

2.10 Discussion and Conclusions

In this paper we have presented measurements of the Ca II λ8542 absorption line using Fabry-Pérot imaging spectroscopy. This work shows the strength and reliability of this technique in measuring radial velocities for a large sample of stars with I-band magnitudes ranging from 10.0 – 16.5. Past investigations have mostly used red giants to study the bar's stellar kinematics. Our work is the first to measure the kinematics of red clump giants, which are more numerous in the inner galaxy than the M and K giants. The main focus of this paper is to present the data and preliminary interpretations, but full interpretation will only be possible with extensive modeling that we will present in Paper III.

We obtained radial velocities for three LOS in the MW bar that include two offset positions at $l \simeq \pm 5^{\circ}$and the central field of BW. The large sample size enabled high precision measurements of the first four moments of the velocity distributions for the first time. The symmetric moment h_4 is significantly non-zero, and its negative value

indicates that the distributions are flat-topped rather than peaked. This seems consistent with a model of the bar with stars in elongated orbits forming two streams at different mean radial velocities, broadening and flattening the total distribution. Because our sample of bar RCGs is essentially complete, the continuity equation suggests that the number of stars in the two streams should be the same. Table 2.5 shows that this is the case within the Poisson noise. We then expect no asymmetry in the velocity distribution function, and our measures of h_3 are indeed consistent with zero.

When we divide our sample into bright and faint samples we detect a clear kinematic signature of streaming motions about the bar. The stellar streams have velocity difference of about 35 km s^{-1} at $l = \pm 5^{\circ}$. There is no indication of these streams in BW, perhaps because they are masked by a spheroidal bulge component. The larger velocity dispersion in BW is consistent with this interpretation. Our large sample size allows us to take the first step towards measuring the LOS kinematics as a function of apparent magnitude (or distance) using the RCGs. As Häfner et al. (2000) points out, these measurements can provide powerful constraints on dynamical models of the inner Galaxy. With larger data sets it will be possible to detect the transition from disk to bar, and measure the bar's thickness.

The technique of FP imaging spectroscopy has allowed us to measure the radial velocities samples that are an order of magnitude larger (at individual LOS) than previous studies. This large sample allows us to determine the kinematics of various stellar populations: bar RCGs, bar M-giants and the disk main sequence stars. Our measurements show that the RCG and M-giant populations have the same $< V_{\rm los} >$ but their dispersions differ by about 10 km s^{-1}. The kinematics of the DMS population suggests that most of these stars belong to the Sagittarius spiral arm.

In addition to the kinematic measurement, we have used the FP spectra to measure the Ca II λ8542 line strengths. We can use these results to measure the metallicities of the individual stars. Metallicity distributions for several LOS in the bar/bulge can

provide strong constraints on the chemical evolution models that can determine the star formation rate, initial mass function, and formation time scale (e.g. Matteucci & Romano 1999; Zoccali et al. 2007) for the inner Galaxy. Our measurements indicate a gradient in mean and dispersion of equivalent width as a function of Galactic longitude, and a clear difference in the mean line strengths between the disk and bulge/bar. The metallicity measurements will be the subject of Paper II.

Motivated by the success of this project, we plan to use the FP system on the 10-m class SALT to obtain a much more extensive determination of the kinematics and metallicity of stars in the inner Galaxy. SALT's much greater aperture and larger FOV will enable us to measure $\gtrsim$ 2000 stars along a single LOS in an hour of observing time. We will investigate at least 10 LOS along the major axis of the bar, obtaining 15000 – 20000 stellar spectra. This data set will provide the basis for models of the structure and chemical evolution of the Galactic bar and bulge. We can also investigate the long bar suggested by recent Spitzer observations (Benjamin 2008) and search for hypervelocity stars. This planned increase by another order of magnitude in the size of the data sample will revolutionize the studies of the inner Galaxy.

Bibliography

Alcock, C., Allsman, R. A., Alves, D. R., Axelrod, T. S., Becker, A. C., Bennett, D. P., Cook, K. H., Drake, A. J., Freeman, K. C., Geha, M., Griest, K., Lehner, M. J., Marshall, S. L., Minniti, D., Nelson, C. A., Peterson, B. A., Popowski, P., Pratt, M. R., Quinn, P. J., Stubbs, C. W., Sutherland, W., Tomaney, A. B., Vandehei, T., & Welch, D. L. 2000, ApJ, 541, 734

Armandroff, T. E., & Zinn, R. 1988, AJ, 96, 92

Benjamin, R. A. 2008, in Bulletin of the American Astronomical Society, Vol. 40, Bulletin of the American Astronomical Society, 266–+

Benjamin, R. A., Churchwell, E., Babler, B. L., Indebetouw, R., Meade, M. R., Whitney, B. A., Watson, C., Wolfire, M. G., Wolff, M. J., Ignace, R., Bania, T. M., Bracker, S., Clemens, D. P., Chomiuk, L., Cohen, M., Dickey, J. M., Jackson, J. M., Kobulnicky, H. A., Mercer, E. P., Mathis, J. S., Stolovy, S. R., & Uzpen, B. 2005, ApJ, 630, L149

Binney, J., Gerhard, O. E., Stark, A. A., Bally, J., & Uchida, K. I. 1991, MNRAS, 252, 210

Bissantz, N., Debattista, V. P., & Gerhard, O. 2004, ApJ, 601, L155

Bissantz, N., & Gerhard, O. 2002, MNRAS, 330, 591

Blitz, L., & Spergel, D. N. 1991, ApJ, 379, 631

Buckley, D. A. H., Hearnshaw, J. B., Nordsieck, K. H., & O'Donoghue, D. 2003, in Presented at the Society of Photo-Optical Instrumentation Engineers (SPIE) Conference, Vol. 4834, Discoveries and Research Prospects from 6- to 10-Meter-Class Telescopes II. Edited by Guhathakurta, Puragra. Proceedings of the SPIE, Volume 4834, pp. 264-275 (2003)., ed. P. Guhathakurta, 264–275

Cabrera-Lavers, A., Gonzalez-Fernandez, C., Garzon, F., Hammersley, P. L., & Lopez-Corredoira, M. 2008, ArXiv e-prints, 809

Clarkson, W., Sahu, K., Anderson, J., Smith, T. E., Brown, T. M., Rich, R. M., Casertano, S., Bond, H. E., Livio, M., Minniti, D., Panagia, N., Renzini, A., Valenti, J., & Zoccali, M. 2008, ApJ, 684, 1110

de Vaucouleurs, G. 1964, in IAU Symposium, Vol. 20, The Galaxy and the Magellanic Clouds, ed. F. J. Kerr, 195–+

Debattista, V. P., & Sellwood, J. A. 2000, ApJ, 543, 704

Debattista, V. P., & Williams, T. B. 2004, ApJ, 605, 714

Deguchi, S. 2001, in Astronomical Society of the Pacific Conference Series, Vol. 228, Dynamics of Star Clusters and the Milky Way, ed. S. Deiters, B. Fuchs, A. Just, R. Spurzem, & R. Wielen, 404–+

Deguchi, S., Fujii, T., Matsumoto, S., Nakashima, J.-I., & Wood, P. R. 2001, PASJ, 53, 293

Dubath, P., Meylan, G., & Mayor, M. 1997, A&A, 324, 505

Duquennoy, A., & Mayor, M. 1991, A&A, 248, 485

Dwek, E., Arendt, R. G., Hauser, M. G., Kelsall, T., Lisse, C. M., Moseley, S. H., Silverberg, R. F., Sodroski, T. J., & Weiland, J. L. 1995, ApJ, 445, 716

Freeman, K. C. 1996, in Astronomical Society of the Pacific Conference Series, Vol. 91, IAU Colloq. 157: Barred Galaxies, ed. R. Buta, D. A. Crocker, & B. G. Elmegreen, 1–+

Freudenreich, H. T. 1998, ApJ, 492, 495

Frogel, J. A. 1988, ARA&A, 26, 51

Fulbright, J. P., McWilliam, A., & Rich, R. M. 2006, ApJ, 636, 821

Gebhardt, K., Pryor, C., Williams, T. B., & Hesser, J. E. 1994, AJ, 107, 2067

Gerhard, O. E. 1993, MNRAS, 265, 213

Gerhard, O. E. 1999, in Astronomical Society of the Pacific Conference Series, Vol. 182, Galaxy Dynamics - A Rutgers Symposium, ed. D. R. Merritt, M. Valluri, & J. A. Sellwood, 307–+

Ghavamian, P., Rakowski, C. E., Hughes, J. P., & Williams, T. B. 2003, ApJ, 590, 833

Habing, H. J., Sevenster, M. N., Messineo, M., van de Ven, G., & Kuijken, K. 2006, A&A, 458, 151

Häfner, R., Evans, N. W., Dehnen, W., & Binney, J. 2000, MNRAS, 314, 433

Hartigan, P., Morse, J., Palunas, P., Bally, J., & Devine, D. 2000, AJ, 119, 1872

Howard, C. D., Rich, R. M., Reitzel, D. B., Koch, A., De Propris, R., & Zhao, H. 2008, ArXiv e-prints, 807

Lewis, J. R., & Freeman, K. C. 1989, AJ, 97, 139

Liszt, H. S., & Burton, W. B. 1980, ApJ, 236, 779

Mao, S., & Paczyński, B. 2002, MNRAS, 337, 895

Matteucci, F., & Romano, D. 1999, Ap&SS, 265, 311

Minniti, D., Olszewski, E. W., Liebert, J., White, S. D. M., Hill, J. M., & Irwin, M. J. 1995, MNRAS, 277, 1293

Minniti, D., White, S. D. M., Olszewski, E. W., & Hill, J. M. 1992, ApJ, 393, L47

Minniti, D., & Zoccali, M. 2008, 245, 323

Mould, J. R. 1983, ApJ, 266, 255

Ng, Y. K., Bertelli, G., Chiosi, C., & Bressan, A. 1996, A&A, 310, 771

Osterbrock, D. E., & Martel, A. 1992, PASP, 104, 76

Paczynski, B., & Stanek, K. Z. 1998, ApJ, 494, L219+

Paczynski, B., Stanek, K. Z., Udalski, A., Szymanski, M., Kaluzny, J., Kubiak, M., & Mateo, M. 1994, AJ, 107, 2060

Palunas, P., & Williams, T. B. 2000, AJ, 120, 2884

Press, W. H., Teukolsky, S. A., Vetterling, W. T., & Flannery, B. P. 1992, Numerical recipes in FORTRAN. The art of scientific computing (Cambridge: University Press, —c1992, 2nd ed.)

Rangwala, N., Williams, T. B., Pietraszewski, C., & Joseph, C. L. 2008, AJ, 135, 1825

Rattenbury, N. J., Mao, S., Debattista, V. P., Sumi, T., Gerhard, O., & de Lorenzi, F. 2007a, MNRAS, 378, 1165

Rattenbury, N. J., Mao, S., Sumi, T., & Smith, M. C. 2007b, MNRAS, 378, 1064

Rich, R. M. 1988, AJ, 95, 828

—. 1990, ApJ, 362, 604

Rich, R. M., Reitzel, D. B., Howard, C. D., & Zhao, H. 2007, ApJ, 658, L29

Sellwood, J. A., & Wilkinson, A. 1993, Reports of Progress in Physics, 56, 173

Sharples, R., Walker, A., & Cropper, M. 1990, MNRAS, 246, 54

Sluis, A. P. N., & Williams, T. B. 2006, AJ, 131, 2089

Spaenhauer, A., Jones, B. F., & Whitford, A. E. 1992, AJ, 103, 297

Stanek, K. Z., Mateo, M., Udalski, A., Szymanski, M., Kaluzny, J., & Kubiak, M. 1994, ApJ, 429, L73

Stanek, K. Z., Udalski, A., Szymanski, M., Kaluzny, J., Kubiak, M., Mateo, M., & Krzeminski, W. 1997, ApJ, 477, 163

Stetson, P. B. 1987, PASP, 99, 191

—. 1994, PASP, 106, 250

Sumi, T. 2004, MNRAS, 349, 193

Sumi, T., Wu, X., Udalski, A., Szymański, M., Kubiak, M., Pietrzyński, G., Soszyński, I., Woźniak, P., Żebruń, K., Szewczyk, O., & Wyrzykowski, Ł. 2004, MNRAS, 348, 1439

Szymanski, M. K. 2005, Acta Astronomica, 55, 43

Terndrup, D. M., Sadler, E. M., & Rich, R. M. 1995, AJ, 110, 1774

Udalski, A., Szymanski, M., Kaluzny, J., Kubiak, M., & Mateo, M. 1992, Acta Astronomica, 42, 253

van Albada, T. S., & Sanders, R. H. 1982, MNRAS, 201, 303

van de Ven, G., van den Bosch, R. C. E., Verolme, E. K., & de Zeeuw, P. T. 2006, A&A, 445, 513

van der Marel, R. P., & Franx, M. 1993, ApJ, 407, 525

Weiner, B. J., & Sellwood, J. A. 1999, ApJ, 524, 112

Zánmar Sánchez, R., Sellwood, J. A., Weiner, B. J., & Williams, T. B. 2008, ApJ, 674, 797

Zhao, H. S. 1996, MNRAS, 283, 149

Zoccali, M., Lecureur, A., Barbuy, B., Hill, V., Renzini, A., Minniti, D., Momany, Y., Gómez, A., & Ortolani, S. 2007, 241, 73

Chapter 3

Fabry-Perot Absorption Line Spectroscopy of the Galactic Bar. I. Metallicities

3.1 Introduction

This is the second paper of the series on measurements of radial velocities and equivalent widths using the Ca II λ8542 line for a large sample of stars in the Galactic bar, based on Fabry-Pérot (FP) absorption line spectroscopy. In Paper I (Rangwala et al. 2009), we used FP imaging spectroscopy at three lines-of-sight (LOS) in the bar: $(l, b) \sim (\pm 5, -3.5)$ and Baade's Window (BW) to obtain a total of 2488 bar red clump giants (RCGs), 339 bar M giants (red giant branch), and 318 disk main sequence stars. This sample is an order of magnitude larger than any previous sample for a given LOS.

The existence of a bar in the Milky Way (MW) is now firmly established. Its photometric signature is seen as a distinct peanut-shaped bulge in the COBE maps (Dwek et al. 1995; Freudenreich 1998). The signature of the bar is also confirmed in the bulge red clump giant (RCG) population (Stanek et al. 1997), in microlensing (Alcock et al. 2000), and in stellar and gas kinematics (Howard et al. 2008; Rangwala et al. 2009; Weiner & Sellwood 1999). These morphological and dynamical observations strongly indicate a bar-like feature, formed from secular evolution processes. But detailed chemical abundance measurements (Rich 1988; Matteucci 1992; Ballero et al. 2007; Zoccali et al. 2007) in Baade's Window find an old, α-enhanced, and metal-rich population, indicating a bulge that was formed on a very short timescale with high star formation efficiency. To understand and resolve the issues related to the formation of structure

in the inner Galaxy, a variety of dynamical and chemical studies have been performed over many years and still continue. For recent progress in the studies of the Galactic bulge see the reviews by Minniti & Zoccali (2008) and Rich et al. (2007).

In Paper I, we showed that FP techniques are very efficient for simultaneously measuring high precision radial velocities of a large sample of stars. Our large radial velocity sample produced an accurate determination of the detailed shape of this velocity distribution in the bar and measured the difference in the radial streaming motions of the stars on the near and far sides of the bar. These observations provide strong constraints on the dynamical models of the bar (Debattista et al. in preparation).

The main goal of this paper is to test the suitability of FP spectroscopy for reliable and robust line strength measurements, and to determine the stellar metallicity distributions along the three LOS. The calcium triplet (CaT) lines in the cool giants have been established as reliable indicators of [Fe/H], and have been used extensively to infer the metallicities of globular clusters (Armandroff & Zinn 1988; Armandroff & Da Costa 1991; Zinn 1985; Rutledge et al. 1997; Cole et al. 2004; Carrera et al. 2007) and of dwarf spheroidal galaxies (Tolstoy 2005). These investigations have determined the calibration between the summed equivalent widths of the triplet and [Fe/H] using red giants in numerous globular clusters (GC) over a range of [Fe/H] ($-2.0 \lesssim$ [Fe/H] $\lesssim +0.5$ dex). We can apply similar techniques to use our Ca II λ8542 line strength measurements to obtain [Fe/H] for our large sample of stars. We demonstrate the reliability of our EWs by measuring the mean [Fe/H] of NGC 6522, a bulge globular cluster that is present in our BW field. We also determined a new calibration between the CaT index and [Fe/H] for the bulge RCGs by using recent high resolution [Fe/H] measurements by Zoccali et al. (2007), and apply this calibration to infer metallicity for our sample.

Measuring the stellar metallicity distribution (SMD) from a large sample of stars can be a very useful tool for the chemical evolution models to constrain different formation scenarios for the bulge (e.g. Did it form inside-out or outside-in? What is the timescale

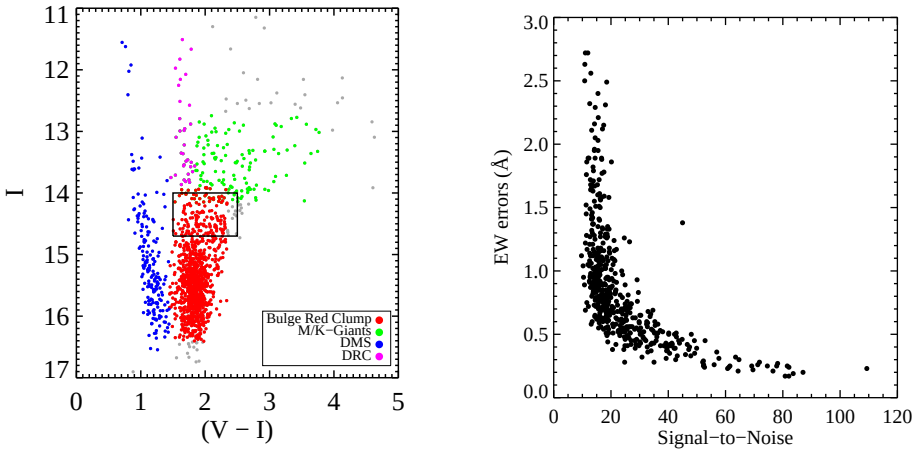

Figure 3.1 Left: CMD for $(l, b) = (-5.0, -3.5)$ LOS. We have radial velocity and EW_{8542} for every star on this plot. CMDs at the other two LOS have similar features. The rectangle shows the bulge sample selection of Zoccali et al. (2007). The I and V band photometry comes from the OGLE survey. Right: EW uncertainties as a function of S/N for $l = -5^\circ$ line-of-sight.

of its formation?). The SMD in the Baade's Window (BW) has been measured by many authors using both high and low-resolution spectroscopy and photometric data (Sadler et al. 1996; Fulbright et al. 2006; Zoccali et al. 2003, 2007). These measurements in BW find the bulge to be metal-rich and α-enhanced, supporting the formation model where the bulge was formed on a short timescale (less that a Gyr) with a high star-formation rate (Ballero et al. 2007). If there is a bar and a classical bulge then abundance studies in BW alone will not be sufficient to separate the two components. Looking for metallicity gradients along the bar can provide additional constraints on differences between the two components. Our measurements differ from previous works both in the large sample size and in including two positions along the major axis of the bar in addition to BW.

The combination of velocity and metallicity distributions can be used to detect the signature of tidal streams associated with disrupted satellites. The Sagittarius stream was discovered in the measurements of the bulge velocity distribution by Ibata et al. (1995). We report in this paper an indication of a possible tidal stream at our $l = +5.5^\circ$

LOS.

3.2 Observations and Data Reduction

The observations were made using the Rutgers Fabry-Pérot system on the CTIO 1.5m telescope. A total of 10 sub-fields were observed: four each at $l \simeq \pm 5^{\circ}$ (MM7B and MM5B fields respectively) and two in BW. The positions of these fields are listed in Table 1 of Paper I. We chose to observe the Ca II λ8542 line, which is one of the strongest features in the late-type stars like the RCGs, is not contaminated by the foreground ISM, and is relatively free of strong terrestrial emission lines. We used a medium-resolution etalon with a spectral response function that is well fit by a Voigt function with a FWHM of 4 Å, equivalent to approximately 140 km s^{-1} at 8500 Å. We typically scanned a range of 8530 – 8555 Å with wavelength steps of 1 Å.

The basic procedure in Fabry-Pérot (FP) imaging spectroscopy is to obtain a series of narrow-band images, tuning the interferometer over a range of wavelengths covering a spectral feature of interest. The data cube thus produced is analyzed to extract a short portion of the spectrum of each object in the field of view, using DAOPHOT (Stetson 1987) to measure a flux of each star in each image. For a field of view with many objects of interest, the technique can be extremely efficient.

The Ca II λ8542 absorption line is fit with a Voigt function to obtain the central wavelength, continuum, total area in the line, and the Gaussian and Lorentzian widths. A sub-sample of our spectra are shown in Figure 3.2, illustrating the range of equivalent widths (EW) measured. Our sample for three LOS consists a total of 2488 bar RCGs, $\sim$ 300 bar M-giants and $\sim$ 350 disk main sequence stars. To select these various stellar populations we used I and V band photometry, the majority of which comes from the OGLE catalogue (Szymanski 2005). The selections are shown in Figure 3.1 (left panel) and discussed in Paper I.

The right panel of Figure 3.1 shows the uncertainties of the EW measurements over

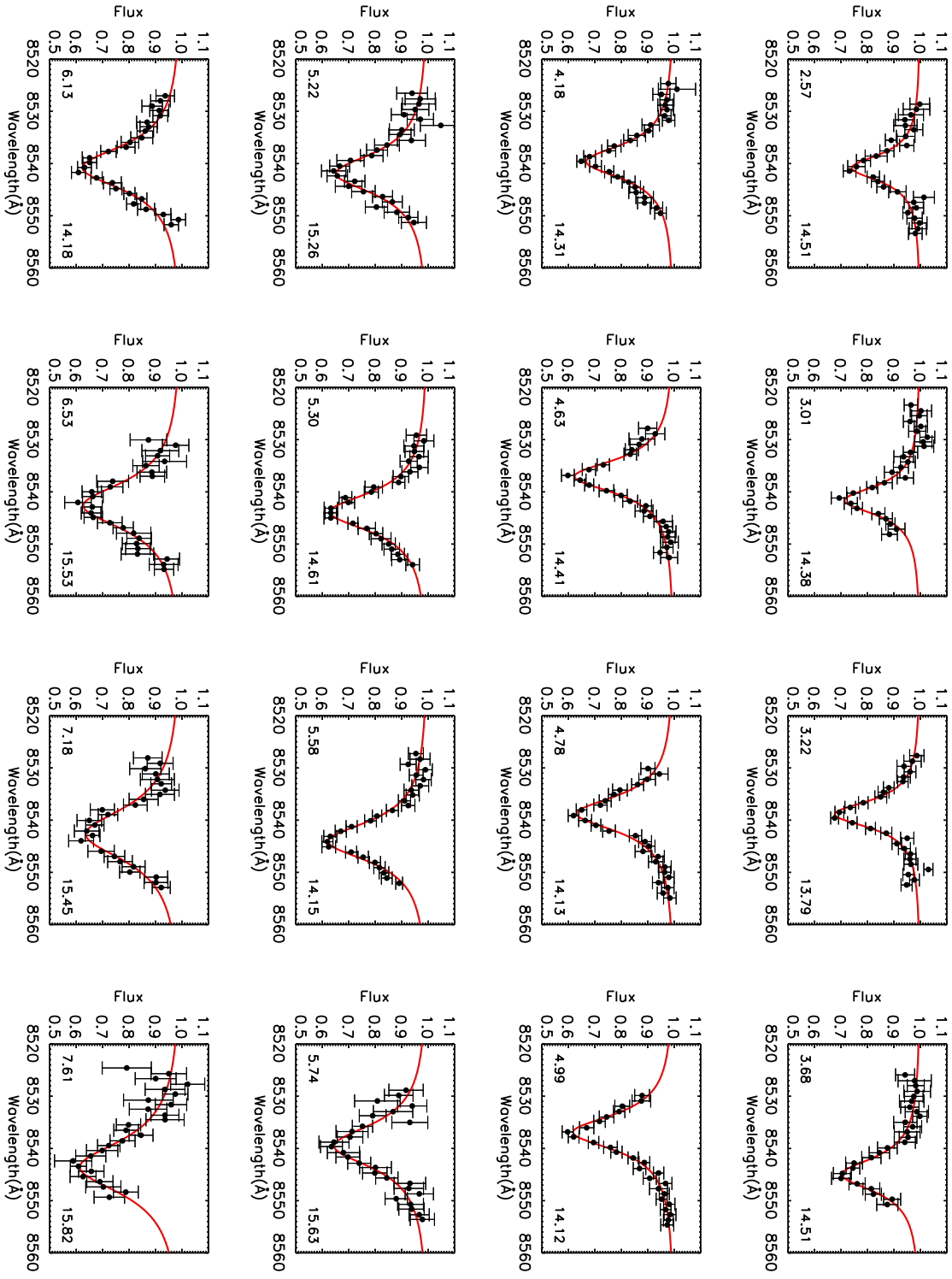

Figure 3.2 A sub-sample of Ca II λ8542absorption lines illustrating the range of EWs measured. Solid line is the Voigt fit. EW (lower left) and I-band magnitude (lower right) is listed for each spectrum.

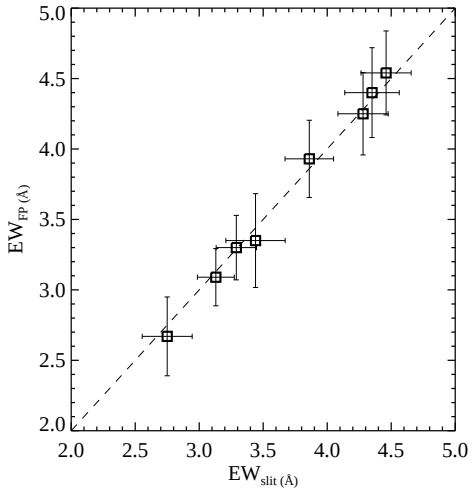

Figure 3.3 Comparing EWs of Ca II λ8542 line measured by fitting Voigt function to 25 Å bandpass (FP) and 60 Å bandpass (slit).

the S/N range of our sample. The median fractional uncertainty is 1/6th of the EW. As expected, the uncertainty increases when the S/N decreases, but there is a wide uncertainty range at S/N $\sim$ 20, which comes mostly from sampling different portions of the line in different stars (see Figure 3.2). Another source of uncertainty comes from the fact that we observe a limited part of the spectrum around the Ca II λ8542 line compared to slit spectra, which typically measure entire line profiles and surrounding continua. To investigate the effects of our limited spectral range, we generate 1000 random realizations of the spectrum of each of 8 red giants from the globular cluster 47 Tuc (provided by Andrew Cole; private comm.). We fit Voigt functions to these spectra over two different bandpasses: 25 Å (FP) and 60 Å (slit). The mean EW and standard deviation for each of the 8 stars is plotted in Figure 3.3. No bias is introduced in the EW due to the limited FP bandpass, but the uncertainty is larger by a factor of 1.5.

We only measure the single, strongest line of the triplet. The total EW of all three lines is $\sum \mathrm{W} = \mathrm{W}_{8498} + \mathrm{W}_{8542} + \mathrm{W}_{8662} = 2.21\mathrm{W}_{8542}$. The factor of 2.21 is verified using the data from 47 Tuc and was also confirmed by Andrew Cole (private comm.), who finds this factor to be the same over a wide range of metallicities. This factor is also

consistent with synthetic spectra, the solar spectrum (Mould 1976), and the spectra of many dwarf and giant stars (Jones et al. 1984).

3.3 Measurement of Equivalent Width and Comparison with Different Indices

In Paper I, we published measurements of the EW of the Ca II λ8542 line by fitting a Voigt function to the absorption line and integrating the fit over all wavelengths. We call this index W_∞ to indicate that the integration bandpass is from 0 to ∞. Our spectra are measured over a limited wavelength range, which could affect the continuum and EW measurements. In addition we need to assess the effects of our W_∞ definition, which differs from the indices used in previous investigations. We use both the synthetic spectral line database of Munari et al. (2005)[1] and also spectra of the red giants from 47 Tuc (provided to us by Andrew Cole, private comm.) to analyze these effects.

We compare our index to those of Cole et al. (2004) (C04 hereafter) and Carrera et al. (2007) (Ca07 hereafter). C04 measure the EW of all three of the calcium triplet lines, fitting each with the sum of a Gaussian and a Lorentzian, and then integrating the fit over a 20 Å bandpass. Ca07 use the same functional form as C04 but different, and wider continuum and line bandpasses[2]. Ca07 found no significant differences between their index and that of C04, but we will show below that there is a small systematic difference between them. These two indices differ from W_∞ in three ways: the functional form, the continuum definition, and the integration bandpass. We address the effects of each of these factors below.

We created a series of artificial profiles using a Voigt function with a range of Gaussian and Lorentzian widths, and then fitted them with the sum function. In every case the sum fit is indistinguishable from the Voigt profile and yields the same EW.

[1] http://archives.pd.astro.it/2500-10500/

[2] The line and continuum bandpass used by Ca07 are defined in Cenarro et al. (2001)

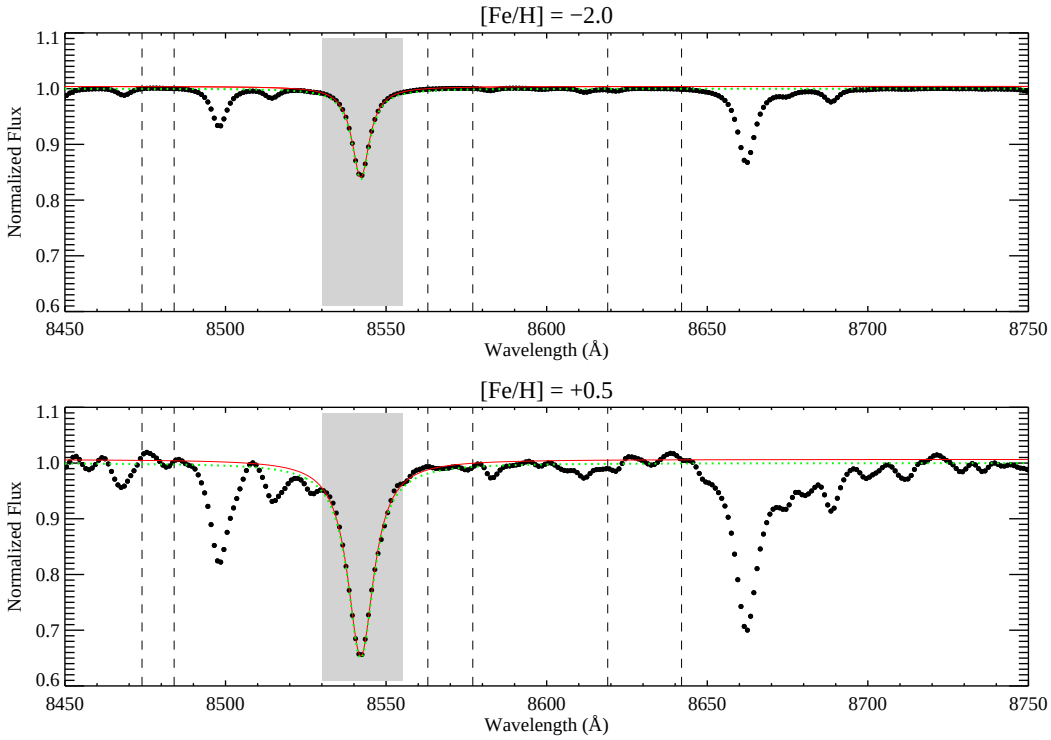

Figure 3.4 Synthetic spectra for two different metallicities are fit with a Voigt function using two different estimates of the continuum: (1) the continuum bands from Ca07 (red solid line) and (2) the continuum from the best-fit Voigt function (green dotted line). The shaded region shows the range (8530 Å – 8555 Å) over which we fit the Voigt function to our FP spectra. Vertical dashed lines show Ca07 continuum bands.

We also verified that fitting the 47 Tuc spectra with the two functional forms gives identical profiles and EW. We conclude that the value of the EW index is independent of the choice between these two functional forms. We choose to use the Voigt function because the intrinsic stellar line profile is a Voigt, our instrumental profile is a Voigt, and the convolution of the two is also a Voigt.

We generate synthetic spectra with the following stellar parameters: $T_{\rm eff} = 4750$ K, log (g) = 3.0 (in cm s^{-2}), $V_{\rm rot} = 5$ km s^{-1}, micro-turbulence = 2 km s^{-1} and [α/Fe] = 0.0. These values are consistent with Zhao et al. (2001)'s high-resolution spectroscopic measurements of the red clump giants in the solar neighborhood. Synthetic spectra were obtained for [Fe/H] = [-2.0, -1.5, -1.0, -0.5, 0.0, +0.5] dex, covering the entire range of metallicities available in the database. We then convolve these synthetic spectra with our instrumental profile, a Voigt of ~ 4 Å FWHM.

We fit the Ca II λ8542 line in the synthetic spectra with a Voigt function in two ways: first, in which the continuum is measured as the mean flux within several bands, using exactly the same procedure and definition as Ca07, and second, in which the continuum is one of the parameters of the Voigt function fit over a 25 Å bandpass from 8530 – 8555 Å to simulate our FP spectra. We fitted the spectra for all available metallicities (listed above), and show the fits for the highest and lowest [Fe/H] in Figure 3.4. The solid and dotted lines show the fits with the two different continuum definitions. The continuum windows of Ca07 are shown by vertical dashed lines. The differences in the two continuum levels are about 0.4% and 0.7% for the low and high [Fe/H], respectively and the FP-fit continuum is always lower than the Ca07 continuum. For an integration bandpass of 40Å the continuum difference would produce an EW difference of less than 0.3Å in even the strongest-lined stars. We will neglect this systematic difference, both because our random errors are relatively large (median error ~ 0.7 Å), and because our calibration will compensate for systematic effects.

Since the choice of fitting function and the continuum definition have at most a minor

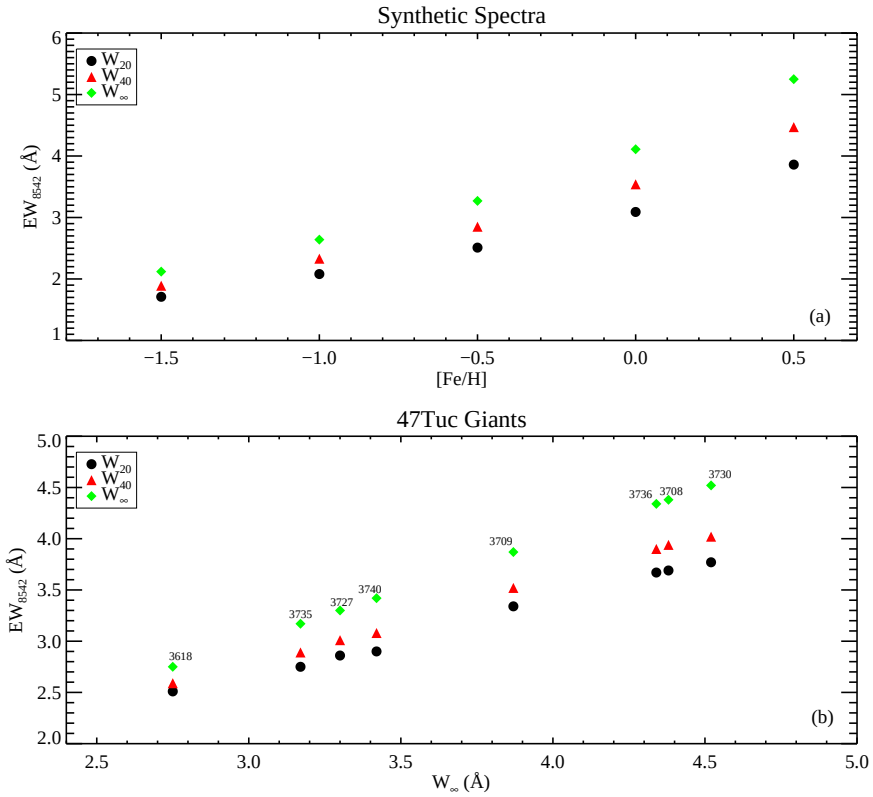

Figure 3.5 Top panel: W_∞(diamonds), W_{40} (triangles) and W_{20} (circles) are measured using synthetic spectra and plotted as a function of [Fe/H]. Bottom panel: The three indices are plotted as a function of W_∞ using spectra of 8 red giant stars from 47 Tuc. The points are labeled with the star ID.

effect on the line index, the choice of integration bandpass is the major contributor to the systematic differences between the index values. Collisional or pressure broadening in the stars atmospheres gives rise to strong damping wings on the calcium line absorption profiles. In metal rich stars, as much as 75% of the EW comes from the wings (Erdelyi-Mendes & Barbuy 1989), and in the Sun the wings extend out to at least 30 Å on either side of the line center (Smith & Drake 1988). Thus we expect that the measured values of the line indices will depend strongly on the spectral range over which the fitted profiles are integrated. We will denote the bandpass definitions of C04 and Ca07 by W_{20} and W_{40} respectively, and our integration of the entire profile as W_{∞}. Figure 3.5 compares these indices for the Ca II λ8542 line, measured in synthetic spectra with a range of metallicities, and also in the observed spectra of 8 red giants in 47 Tuc. Broader integration bandpasses produce systematically larger EW index values, and these differences increase with line strength (or metallicity). In the top panel of Figure 3.6 we show the measured equivalent width of the Ca II λ8542 line in one of the 47 Tuc stars as a function of integration bandpass. The first two points in the plot show W_{20} and W_{40}, respectively. The EW converges to W_{∞} for bandpasses greater than 200 Å.

In the middle panel of Figure 3.6 we compare the values of W_{∞} and W_{40}, measured for our entire sample of FP spectra at $l = -5°$. As expected from the tests shown in Figure 3.5, there is a tight, but non-linear, relation between the indices. We overplot the indices from the synthetic spectra of Figure 3.5a, showing that the indices measured from the limited-range FP data are in excellent agreement with those measured from more extensive, traditional spectra. We have used Monte Carlo simulations to estimate the uncertainties of W_{∞} and W_{40} in the fits to our FP data, and find that the fractional uncertainties of the two indices are identical. Thus it seems to make little difference which integration bandpass one chooses to use. Of course, to apply a previously-determined calibration of the CaT index to [Fe/H], one must use the same index definition. In the bottom panel of Figure 3.6 we show the calibration of W_{20} for

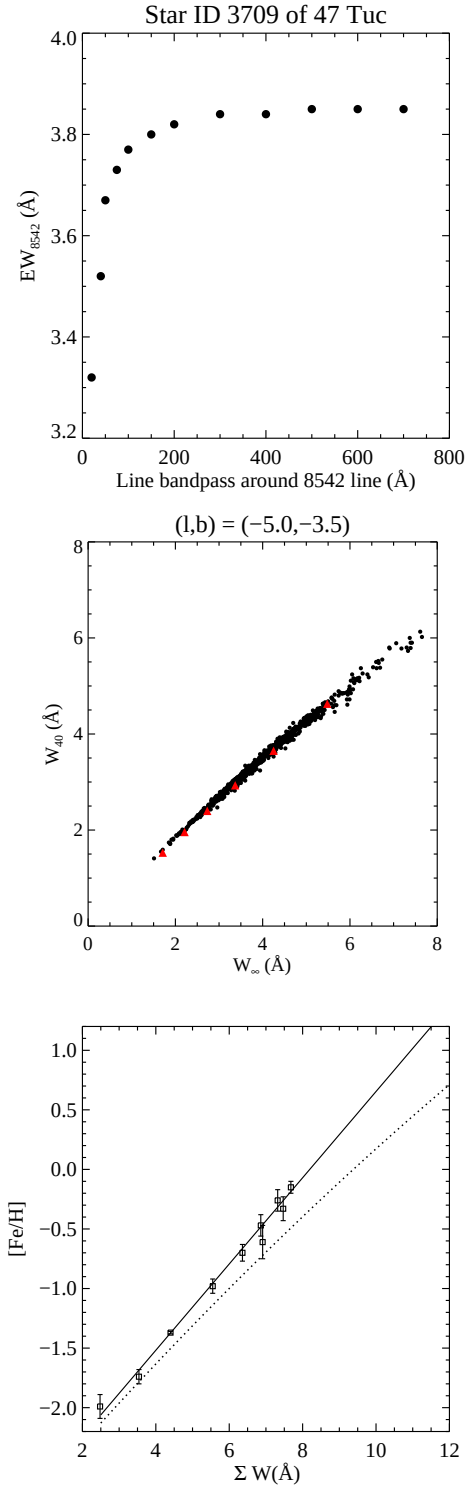

Figure 3.6 Top panel: EW as a function of line bandpass. Middle panel: W_∞ and W_{40} for our sample at $l = -5$. Red points are from synthetic spectra. Bottom Panel: Solid line: calibration of C04's index for a sample of globular clusters; dotted line: Calibration curve transformed to our index W_∞.

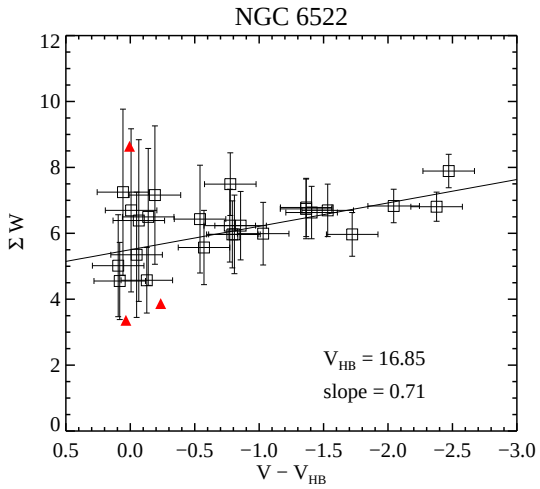

Figure 3.7 The summed EW varies linearly with V band magnitude. The solid line is the best linear fit. Red triangles indicate excluded stars.

globular clusters as measured by C04. We use the $W_\infty - W_{20}$ correlation to calculate the corresponding calibration relation for W_∞, shown by the dotted curve.

3.4 Comparison with high-resolution metallicities

3.4.1 Metallicity of NGC 6522

NGC 6522 is a bulge globular cluster that appears at the southwest edge of our BW field (see Figure 2 of Paper I). The stars from this cluster show up as a distinct kinematic feature in our velocity distribution (see Figure 8 of Paper I). We can use the EWs of these stars to measure the mean metallicity of this cluster via the calcium infrared triplet method. We will compare our measurement to the most recent high-resolution [Fe/H] determination for this cluster by Zoccali et al. (2008) (Zoc08 hereafter), in order to assess the accuracy of our procedures.

To isolate possible members of this cluster from the background bulge population we use the kinematics and photometry of the cluster. We identify the red giant branch of this cluster from the HST CMD (Piotto et al. 2002) and select the stars within 1-σ (7.9 km s^{-1}) of the cluster's mean velocity (-14.67 km s^{-1}). We find 28 possible members

of this cluster, majority of which fall within $2'$ of the cluster center. Compared to the mean EW at a given V magnitude, the EW of three stars deviates significantly (one with a relatively large EW and two with relatively small EWs). Because the cluster's velocity is very near the center of the bulge velocity distribution, the kinematic selection constraint cannot eliminate all of the bulge contamination. In addition, all three stars are near the faint end of the photometric distribution, where there is a higher probability of bulge contamination. We therefore exclude these three stars from the cluster sample. The three excluded stars are indicated by triangles in Figure 3.7.

To convert EWs to metallicity we follow the method in C04. For this analysis we will use W_{40} so that we can consistently use the calibration of C04 and compare to previous work. The first step is to measure the 'reduced equivalent width' to correct for the strong effects of stellar effective temperature and surface gravity in the red giants. This is given by:

$$\mathrm{W}' = \sum \mathrm{W} + \beta(\mathrm{V} - \mathrm{V_{HB}}) \tag{3.1}$$

where the introduction of the horizontal branch magnitude (V_{HB}) removes dependence on the cluster distance or reddening, and $\sum \mathrm{W} = 2.21 W_{40}$ is the summed EW of all three CaT lines. Figure 3.7 shows this relationship for $V_{\mathrm{HB}} = 16.85 \pm 0.20$ (Rutledge et al. 1997). $\sum \mathrm{W}$ increases linearly up the red-giant branch as expected. The best fit to the data is shown by the solid line with a slope of $\beta = 0.71 \pm 0.22$ Å mag^{-1}.

Within the 1-σ error our slope is in good agreement with previous measurements of Rutledge et al. (1997), Ca07 and C04 who measured it to be 0.64 ± 0.02, 0.647 ± 0.005 and 0.73 ± 0.04 respectively, using the data from numerous globular clusters.

The calibration between W$'$ and [Fe/H] as measured by C04 is:

$$[\mathrm{Fe/H}] = (-2.966 \pm 0.032) + (0.362 \pm 0.014)\mathrm{W}' \tag{3.2}$$

This calibration has a rms scatter of $\sigma = 0.07$ dex and is measured for metallicity range of $-2.0 \lesssim [\mathrm{Fe/H}] \lesssim +0.5$ dex (Carrera et al. 2007).

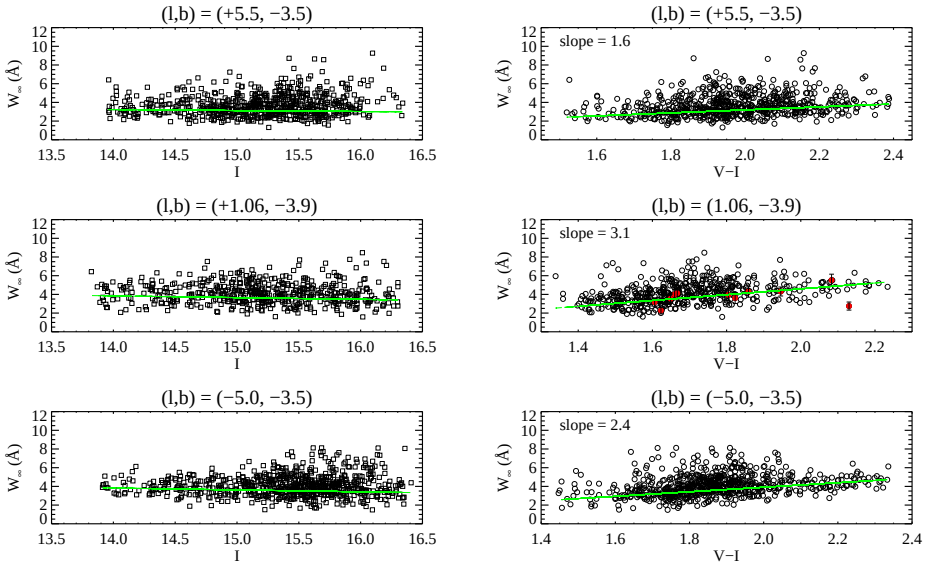

Figure 3.8 W_∞ as a function of color and I-band magnitude. The solid line is the best straight-line fit. Calibration stars indicated in red.

Using this calibration and $W' = 5.70 \pm 0.15$ Å (for $V_{HB} = 16.85$) we obtain $[Fe/H]_{NGC6522} = -0.90 \pm 0.10$ dex . For another value of $V_{HB} = 16.52 \pm 0.07$ as measured from the HST CMD of Sosin et al. (1997) for this cluster we get $W' = 5.96 \pm 0.15$ Å and $[Fe/H] = -0.81 \pm 0.10$ dex.

We compare this result with Zoc08 where they measure high-resolution abundances for stars in the Galactic bulge using VLT FLAMES-GIRAFFE spectrograph. Their sample consists of seven members from NGC 6522. The mean [Fe/H] from these seven stars is -0.91 ± 0.06 dex. Our measurement is in excellent agreement with this work. There is one star (OGLEID 412752) in common with both Zoc08 and our sample. For this star we get [Fe/H] = −0.84 dex and −0.94 dex (±0.42 dex) for lower and higher values of V_{HB} respectively, in agreement with -0.80 ± 0.15 dex as measured by Zoc08.

We also compare our result to Rutledge et al. (1997), who measured the calcium triplet index for 72 GCs. They get a lower [Fe/H] of -1.21 ± 0.04 using 9 possible members of this cluster. They use different weights for the EWs of the three calcium lines to get $W' = 3.47 \pm 0.11$. Converting our index to their system using Equation 3 of

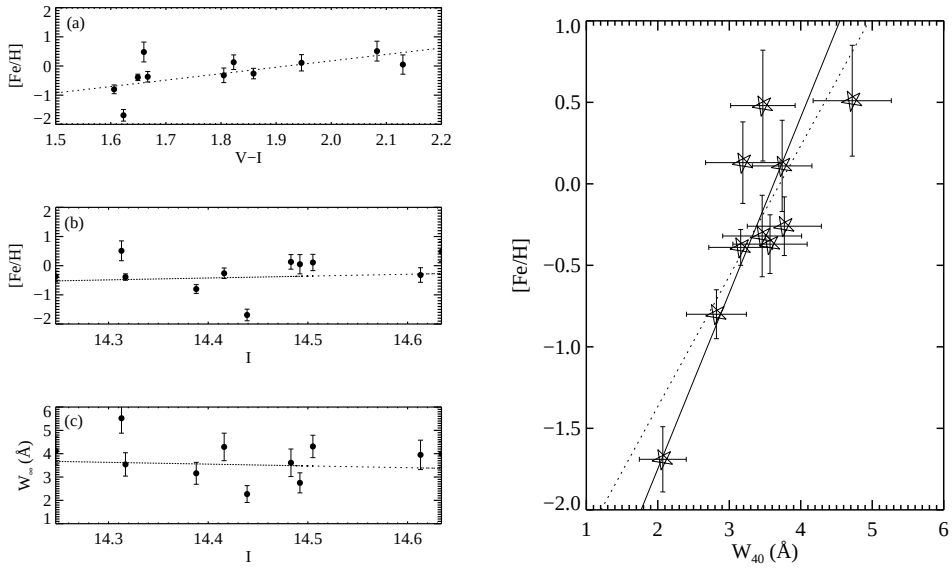

Figure 3.9 Left panel: (a) [Fe/H] as a function of V-I color; (b) I magnitude ; (c) EW as a function of I-band magnitude for the 10 calibration stars. Right panel: Calibration between [Fe/H] and CaT for the bulge RCGs.

Ca07 we get $W' = 4.08 \pm 0.12$, which does not agree with Rutledge's index. Our index converted to their system gives [Fe/H] $= -0.91$ dex using their calibration between W′ and [Fe/H]. Because NGC 6522 is a bulge cluster and has a velocity close to the mean of the bulge velocity distribution, it is very difficult to establish the membership for this cluster. Most of the stars that Rutledge et al. (1997) select as cluster members show large velocity deviations from the mean cluster velocity (even after including their velocity errors), suggesting that their sample may be significantly contaminated by bulge stars.

3.4.2 Ca II λ8542 – [Fe/H] calibration for the bulge stars

There are 11 bulge giants in our sample that have high-resolution [Fe/H] measurements from Zoc08. We can use this sample to define a calibration between CaT and [Fe/H] for the bulge giants, and then use this calibration to infer [Fe/H] for the rest of our sample. We identify these stars as red clump giants, the metal-rich equivalent of horizontal

branch stars, with a very narrow intrinsic luminosity distribution. We do not need to correct to "reduced equivalent width" as we did for the cluster giants in the previous section. To support this assumption we plot in Figure 3.8 W_∞ as a function of I-band magnitude (left panels) for our full RCG sample at all three LOS in the bar. There is no significant trend with luminosity. However, EW clearly does vary with the V-I color as shown in right panels of Figure 3.8. The slope of this relationship changes with the position along the bar, and is largest in BW. The 11 common stars are shown in red in Figure 3.8, and exhibit a similar trend in [Fe/H], as shown in Figure 3.9(a). Thus the change in EW with color in the RCGs reflects a real trend in metallicity, and not a luminosity-dependent variation as seen on the red giant branch. Therefore we do not make any corrections in our sample for this trend.

One of the common stars (with OGLEID 423286) has an anomalously low EW for a given (V-I) color compared to the rest of the sample and will not be used in determining the calibration relation. We plot [Fe/H] from Zoc08 against our W_{40} for the 10 remaining stars in the right panel of Figure 3.9. The solid line shows the best straight-line fit to the data using the uncertainties in both coordinates.

The calibrations for W_{40} and W_∞ are:

$$[\mathrm{Fe/H}] = (-3.828 \pm 0.131) + (0.475 \pm 0.154)(2.21\,\mathrm{W}_{40}) \tag{3.3}$$

and

$$[\mathrm{Fe/H}] = (-3.545 \pm 0.125) + (0.384 \pm 0.114)(2.21\mathrm{W}_{\infty}) \tag{3.4}$$

Here we separate the factor 2.21 for converting single-line EW measurement to the summed EW of the triplet, to facilitate comparison with previous calibrations, e.g. Equation 2 above from C04.

This is the first determination of the CaT to [Fe/H] calibration for the bulge RCGs. All previous measurements were done using red giants in globular clusters. The dotted line in the right panel of Figure 3.9 shows the globular cluster calibration (Equation

3.2), which deviates from the bulge calibration at low and high metallicities. The reduced χ^2 for the globular cluster calibration is greater by 1.5, suggesting that the bulge calibration may not the same as the globular cluster calibration.

In calibrating the calcium triplet EWs to [Fe/H] it is assumed that the ratio of [Ca/Fe] remains constant for all the stars. If instead [Ca/Fe] were to decrease as metallicity increases then the derived [Fe/H] will be underestimated. This ratio for the bulge K giants varies from $\sim +0.4$ to 0.0 dex as a function of [Fe/H] (Fulbright et al. 2007). This variation can affect the calibration but because our individual uncertainties are of the same order or larger, it will not significantly affect our measurements.

3.5 Stellar Metallicity Distributions

We use W_∞ in Equation 3.4 to infer metallcities for the RCG sample (all the points shown in red in Figure 3.1) to obtain the SMDs at three LOS in the bar. The SMDs are shown in Figure 3.10. In the BW SMD (middle panel) a distinct peak around -0.9 dex is from NGC 6522. The distribution is significantly broadened by our relatively large uncertainties. To take into account the effect of the individual errors we use maximum likelihood estimator (Pryor & Meylan 1993) to measure the true dispersion of these distributions. The mean and dispersion are listed in Table 3.1 along with the corresponding kinematics as measured in Paper I. Only statistical uncertainties are listed in this table. The calibration will introduce an additional systematic uncertainty of about 0.1 dex.

Previous observations of Fulbright et al. (2006) (also see Rich 1988; Sadler et al. 1996) show that the bulge metallicity distribution can range from -1.5 to $+1.0$ dex. Our SMDs have extended high metallicity tails. Most of the stars in these tails are at the faint end of our sample and have large EW uncertainties. Our calibrations extend only to [Fe/H] $= +0.5$ dex, and the analysis of section 3 suggests that at higher metallicity the calibration may become non-linear. Thus we do not believe that our observations

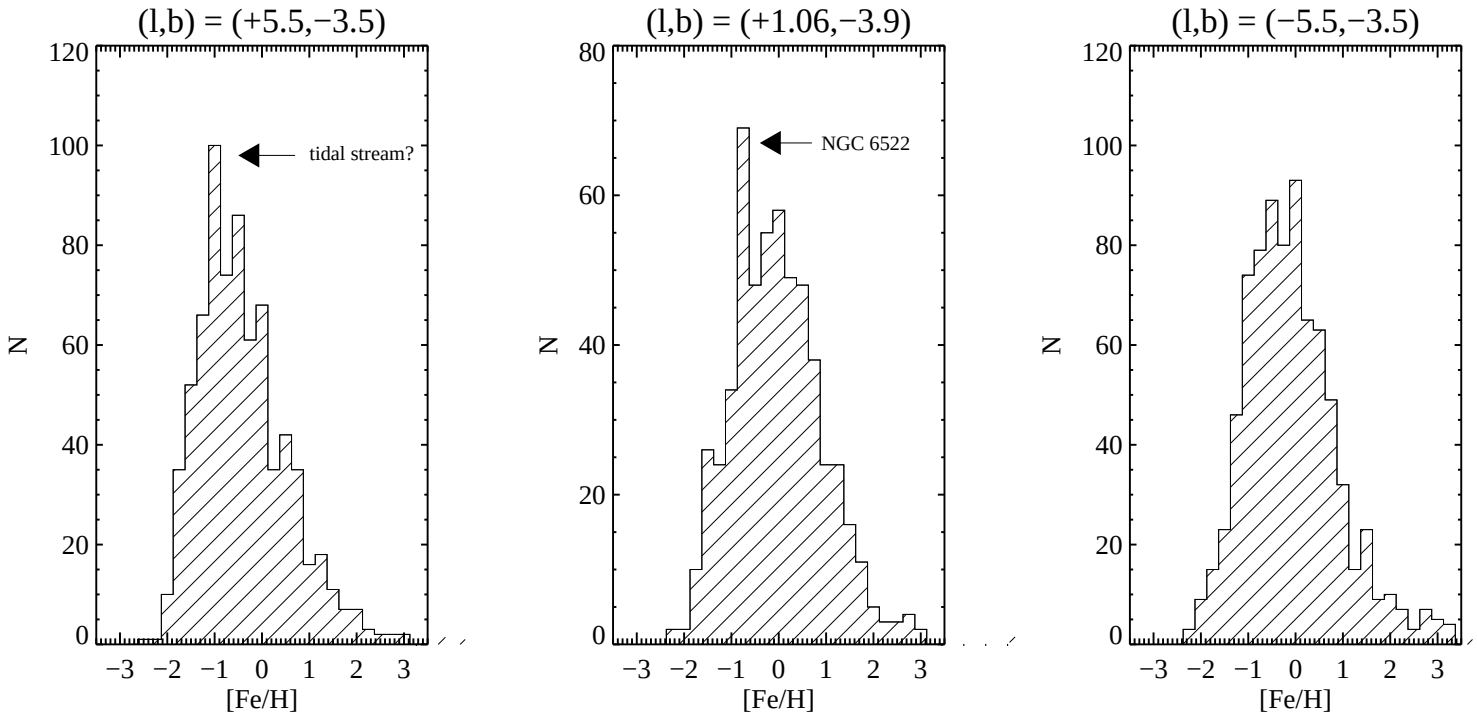

Figure 3.10 SMDs along the major axis of the bar.

Table 3.1 Mean metallicity and its dispersion, and kinematics of the RCGs in the bar for three LOS.

LOS (l,b)	$< [Fe/H] >$ (dex)	$\sigma_{[Fe/H]}$ [a] (dex)	$< V_{los} >$ km s^{-1}	$\sigma_{V_{los}}$ [a] km s^{-1}	N
(5.5,-3.5)	-0.55 ± 0.03	0.42 ± 0.03	30.73 ± 3.89	102.38 ± 2.39	738
(1.1,-3.9)	-0.09 ± 0.04	0.58 ± 0.04	-1.01 ± 5.42	112.62 ± 3.41	557
(-5.0,-3.5)	-0.17 ± 0.03	0.39 ± 0.03	-52.56 ± 3.85	102.30 ± 2.50	804

[a]The dispersion is measured using Maximum Likelihood Estimator

give reliable evidence for any stars with [Fe/H] $\gtrsim$ 1.0 dex. This conclusion is further supported by the comparison shown in Section 5.1 below, where SMDs with maximum [Fe/H] $\lesssim$ 1.0 dex, when convolved with our uncertainties, show similar extended tails.

The SMD at $(l, b) = (5.5, -3.5)$ shows an excess at [Fe/H] $= -1.0$ dex, significantly different from the mean [Fe/H] of the underlying distribution. The velocity distribution at this LOS from Paper I, reproduced here in the top panel of Figure 3.11, also shows an excess at $V_{los} = -36.5$ km s^{-1}, about 70 km s^{-1} away from the mean of the distribution. Since our measurements of velocity are more accurate than those of metallicity, we select the stars between -45 km s^{-1} and -28 km s^{-1}. The metallicity distribution of these stars is shown in the bottom panel of Figure 3.11, where the peak at -1.0 dex is much more evident. This feature may indicates the presence of a tidal stream or debris from a disrupted satellite.

Does this feature belong to the Sagittarius stream? The location and kinematics of the tidal debris of the Sagittarius dwarf galaxy have been traced by Majewski et al. (2004) and Martínez-Delgado et al. (2004). The Sagittarius stream passes through this LOS ($l, b = 5.5, -3.5°$), but is located at heliocentric distance of $\sim$ 28 kpc, on the other side of the Galaxy. The metallicity of -1.0 dex of our feature is consistent with the range of metallicity of the stars in the Sagittarius stream. The distance modulus to this portion of the stream is 17.24 mag; the V-band extinction from the Sun to this field is 1.94 mag (Sumi et al. 2004), and there is presumably a similar additional extinction

beyond this field to the stream. The V magnitude of the stars in our feature range from 16.0 to 17.5 with a mean of 17.2. So, if these stars were in the Sagittarius stream their absolute visual magnitudes would range from -4.8 to -3.7 with a mean of -4.0. Such stars are extremely rare MIa supergiants (Mihalas & Binney 1981), so it is highly improbable that our sample would contain so many of them. More conclusively, the expected heliocentric radial velocities of stars in the Sagittarius stream along our LOS is $+180 \pm 15$ km s^{-1}; the velocities of the stars in our feature are -36.5 ± 8 km s^{-1}. Thus we conclude that the cold kinematic feature that we detect is not associated with the Sagittarius stream. To confirm the existence of this stream and to better measure its properties will require additional spectroscopic observations over a larger field of view.

3.5.1 Comparison in Baade's Window

We compare our SMD in BW with Zoc08 and Fulbright et al. (2006) (Fb06 hereafter) in Figure 3.12. Our BW/bulge sample consists of 557 RCGs. The Zoc08 sample consists of 204 stars at the bright end of our RCG sample, and covers a very similar color range; their selection limits are indicated by the rectangle in Figure 3.1. They supplement their sample with 200 RCGs in BW (Lecureur et al. in prep.), but these latter measurements are not yet published so we can only make comparison to the former sample. The Fb06 bulge sample is obtained by the recalibration of the Sadler et al. (1996) sample that consists of about 320 RCGs.

Because the individual uncertainties of our sample are large, we convolve Zoc08 and Fb06 SMDs with our error distribution to make consistent comparisons. We generate 10000 random realizations (with replacement) of the Zoc08 and Fb06 samples, and add to them an error distribution that is randomly drawn from our observed error distribution. The solid histogram in both panels of Figure 3.12 is our SMD, and the dashed histograms show the Zoc08 (left panel) and Fb06 (right panel) SMDs. We

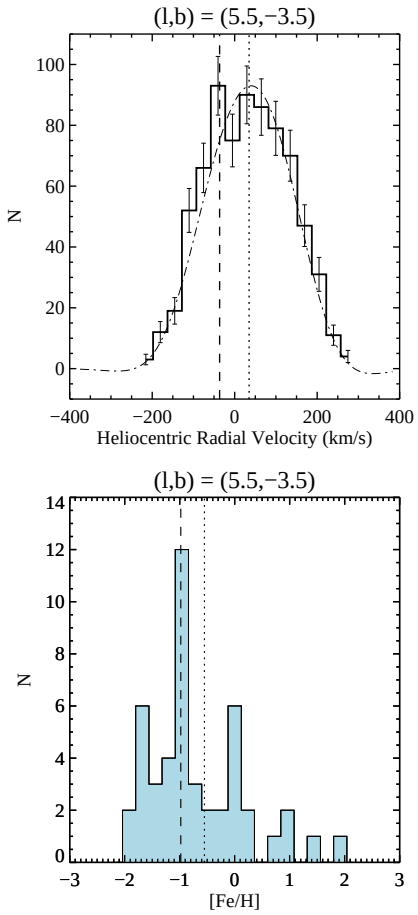

Figure 3.11 Possible signature of disrupted satellite: top panel: the velocity distribution of 738 stars with an excess around -35 km s^{-1}; bottom panel: the metallicity distribution of all 48 stars in this velocity peak. In both panels the dotted line indicates the mean of the distribution and the dashed line indicates the location of the excess.

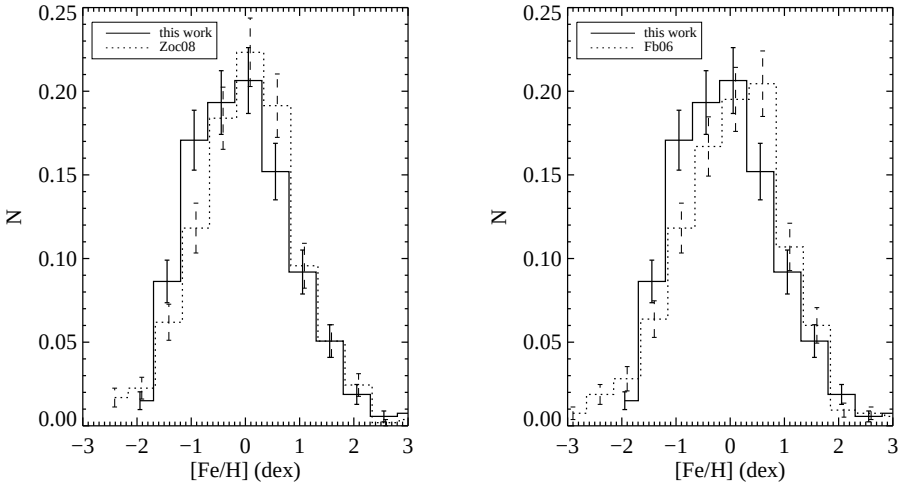

Figure 3.12 Comparing the stellar metallicity distributions to previous work in Baade's Window.

agree very well with both of these measurements. The major difference is an excess of stars around −0.9 dex in our SMD, due to the cluster NGC 6522. Since the center of this cluster is only 30 ″ from the edge of our field, we include a significant number of cluster stars in our sample. The sample of Fb06 discriminates against cluster stars by construction (Terndrup et al. 1995) and the photometric limits of Zoc08 select only a small part of the cluster's red giant branch. Thus we expect our sample to include higher proportion of stars from this cluster. Our mean metallicity in BW is −0.09 dex, close to solar, and agrees well with Zoc08 (∼ 0.0 dex) and Fb06 (−0.1 dex). Our dispersion in BW is 0.58 dex, comparable to the value of 0.52 dex calculated from the Fb06 sample. Both are larger than the dispersion of 0.40 dex measured by Zoc08.

3.5.2 Metallicity gradient along the Bar

The mean metallicity and dispersion are lower at the two offset positions in the bar compared to BW (see Table 3.1). Zoc08 and Minniti et al. (1995) find a gradient of about -0.25 dex along the minor axis of the bar/bulge between b = −4° and −12°. We report here the first measurements of metallicity gradients along the major axis of the

bar. We find a larger gradient towards $l = +5\ ^\circ$ (0.45 dex) than towards $l = -5^\circ$ (0.1 dex). The metallicity dispersion is larger in BW as compared to the offset positions and decreases almost equally, by ~ 0.2 dex in each direction. This trend correlates with the LOS velocity dispersion that is also higher in BW and decreases by equal amounts at the offset positions as shown in Paper I. The higher mean metallicity at the center of bar may suggest that we are seeing an older, metal rich bulge population in BW compared to the stars at $l = \pm 5$ in the bar.

3.6 Discussion and Conclusion

In this paper, we have presented EW measurements of the Ca II λ8542 line using FP absorption spectroscopy at three position along the major axis of the Galactic bar. This is the first attempt to use FP spectra for measuring stellar absorption line strengths. We show that reliable line strengths can be obtained for hundreds of stars with this technique, allowing future FP observations to measure accurate radial velocities and line strengths simultaneously from the same datacube.

We compare our CaT index with those of C04 and Ca07, and find that the major difference between them comes from the differences in the integration bandpass. This has a minor effect for weak lines but deviates non-linearly as the line strength increases, reflecting the strong damped wings of the CaT lines. We find the three indices to be tightly correlated, and the ratio of EW to its uncertainty remains constant for all of them. The differences between them does not affect any previous metallicity measurement, since each index was calibrated to [Fe/H] appropriately. We have investigated the effect of adding more samples to the FP data, and have found that the uncertainty of the EW can be reduced by a factor of two (i.e. to be comparable to the accuracy of similar S/N slit spectroscopy) by including as few as four extra samples on the red side of the absorption line (between 8555 – 8580 Å).

To test the reliability our EWs we derive the metallicity of NGC 6522, a bulge

globular cluster that is present in our BW field. We used the C04 calibration to infer the metallicity from our EWs. We obtained mean [Fe/H] for this cluster to be -0.91 dex, in excellent agreement with recent measurement from Zoc08. However, previous measurements of NGC 6522 have reported a relatively lower mean [Fe/H] of -1.28 ± 0.12 (Terndrup et al. 1998), -1.44 ± 0.15 (Zinn 1985) and -1.21 ± 0.04 (Rutledge et al. 1997), where the former two measurements were obtained using CMDs and the latter one was used the CaT method. A relatively moderate mean metallicity is surprising for this cluster as it has a very blue horizontal branch. This cluster is most probably one of the 'second parameter' bulge clusters, where the metallicity is not the sole factor in determining the HB morphology (Catelan 2000; Fusi Pecci & Bellazzini 1997). The second parameter could be the age of the cluster, mass lost on the RGB, rotation, helium abundance, etc. The bulge sample of Zoc08 also contains five stars from another bulge globular cluster NGC 6558 for which a detail analysis is presented in Barbuy et al. (2007). This bulge cluster was also found to be moderately metal poor (-0.97 dex) with a very blue horizontal branch. Their analysis suggested that age was the second parameter for this cluster. They found it to be old at 14 Gyrs, and α-enhanced. A complete chemical abundance analysis of NGC 6522 is being performed by the same group (Barbuy et al. in preparation). Any further analyses of second parameter issues in NGC 6522 is beyond the scope of this paper.

We use the EWs of 10 stars in our sample that also have high resolution [Fe/H] measurements to obtain the calibration between the EW of the Ca II λ8542 line and [Fe/H] for the RCGs in the Galactic bulge. We find this calibration to be marginally different from that of the globular clusters. We use this calibration to infer [Fe/H] for all the RCGs in our sample at three LOS in the bar to obtain the SMDs. The signature of NGC 6522 is detected in the BW SMD around -0.9 dex. We find the mean metallicity in BW to be close to solar, consistent with previous work, and find a metallicity gradient along the bar of up to 0.45 dex. The metallicity dispersion also

shows gradient of about 0.2 dex between BW and $l = \pm 5^{\circ}$ LOS. Pérez et al. (2009) found that the bars in external galaxies can have positive, negative, or null metallicity gradients. They argue that these measurements can constrain the models of structure formation and star formation history for the inner parts disk galaxies, and may also distinguish between a bar and a classical bulge. We expect that our measurements can similarly constrain models of the MW bar/bulge.

The velocity and metallicity distribution at $l = +5.5^{\circ}$ show a distinct feature at -36.5 km s^{-1} and -1.0 dex respectively. This is a previously unknown cold kinematic feature, not associated with the Sagittarius stream. Spectroscopic observation over a larger FOV along this LOS are required to confirm this feature. This will be possible from our future survey of the bar with SALT.

We plan to use the FP system on the 10-m class Southern African Large Telescope (SALT) to obtain a much more extensive determination of the kinematics and metallicity of stars in the inner Galaxy. SALT's much greater aperture and larger FOV will enable us to measure $\gtrsim 2000$ stars along a single LOS in an hour of observing time. We will investigate at least 10 LOS along the major axis of the bar, obtaining 15000 – 20000 stellar spectra in total. By slightly changing the observing strategy for scanning the absorption line we will obtain EW measurements of much higher precision than those of this paper. In addition we will select fields in BW that already have high-resolution [Fe/H] measurements to greatly improve the precision of the CaT to [Fe/H] calibration. Such a large sample of radial velocity and metallicities along several positions in the bar will be ideal to look other cold kinematic features from disrupted satellites, gradients in the shape of velocity and SMDs, and correlations between them, and search for hypervelocity stars.

Bibliography

Alcock, C., Allsman, R. A., Alves, D. R., Axelrod, T. S., Becker, A. C., Bennett, D. P., Cook, K. H., Drake, A. J., Freeman, K. C., Geha, M., Griest, K., Lehner, M. J., Marshall, S. L., Minniti, D., Nelson, C. A., Peterson, B. A., Popowski, P., Pratt, M. R., Quinn, P. J., Stubbs, C. W., Sutherland, W., Tomaney, A. B., Vandehei, T., & Welch, D. L. 2000, ApJ, 541, 734

Armandroff, T. E., & Da Costa, G. S. 1991, AJ, 101, 1329

Armandroff, T. E., & Zinn, R. 1988, AJ, 96, 92

Ballero, S. K., Matteucci, F., Origlia, L., & Rich, R. M. 2007, A&A, 467, 123

Barbuy, B., Zoccali, M., Ortolani, S., Minniti, D., Hill, V., Renzini, A., Bica, E., & Gómez, A. 2007, AJ, 134, 1613

Carrera, R., Gallart, C., Pancino, E., & Zinn, R. 2007, AJ, 134, 1298

Catelan, M. 2000, ApJ, 531, 826

Cenarro, A. J., Cardiel, N., Gorgas, J., Peletier, R. F., Vazdekis, A., & Prada, F. 2001, MNRAS, 326, 959

Cole, A. A., Smecker-Hane, T. A., Tolstoy, E., Bosler, T. L., & Gallagher, J. S. 2004, MNRAS, 347, 367

Dwek, E., Arendt, R. G., Hauser, M. G., Kelsall, T., Lisse, C. M., Moseley, S. H., Silverberg, R. F., Sodroski, T. J., & Weiland, J. L. 1995, ApJ, 445, 716

Erdelyi-Mendes, M., & Barbuy, B. 1989, A&AS, 80, 229

Freudenreich, H. T. 1998, ApJ, 492, 495

Fulbright, J. P., McWilliam, A., & Rich, R. M. 2006, ApJ, 636, 821

—. 2007, ApJ, 661, 1152

Fusi Pecci, F., & Bellazzini, M. 1997, in The Third Conference on Faint Blue Stars, ed. A. G. D. Philip, J. Liebert, R. Saffer, & D. S. Hayes, 255–+

Howard, C. D., Rich, R. M., Reitzel, D. B., Koch, A., De Propris, R., & Zhao, H. 2008, ApJ, 688, 1060

Ibata, R. A., Gilmore, G., & Irwin, M. J. 1995, MNRAS, 277, 781

Jones, J. E., Alloin, D. M., & Jones, B. J. T. 1984, ApJ, 283, 457

Majewski, S. R., Kunkel, W. E., Law, D. R., Patterson, R. J., Polak, A. A., Rocha-Pinto, H. J., Crane, J. D., Frinchaboy, P. M., Hummels, C. B., Johnston, K. V., Rhee, J., Skrutskie, M. F., & Weinberg, M. 2004, AJ, 128, 245

Martínez-Delgado, D., Gómez-Flechoso, M. Á., Aparicio, A., & Carrera, R. 2004, ApJ, 601, 242

Matteucci, F. 1992, Memorie della Societa Astronomica Italiana, 63, 301

Mihalas, D., & Binney, J. 1981

Minniti, D., Olszewski, E. W., Liebert, J., White, S. D. M., Hill, J. M., & Irwin, M. J. 1995, MNRAS, 277, 1293

Minniti, D., & Zoccali, M. 2008, 245, 323

Mould, J. R. 1976, ApJ, 210, 402

Munari, U., Sordo, R., Castelli, F., & Zwitter, T. 2005, A&A, 442, 1127

Pérez, I., Sánchez-Blázquez, P., & Zurita, A. 2009, A&A, 495, 775

Piotto, G., King, I. R., Djorgovski, S. G., Sosin, C., Zoccali, M., Saviane, I., De Angeli, F., Riello, M., Recio-Blanco, A., Rich, R. M., Meylan, G., & Renzini, A. 2002, A&A, 391, 945

Pryor, C., & Meylan, G. 1993, 50, 357

Rangwala, N., Williams, T. B., & Stanek, K. Z. 2009, ApJ, 691, 1387

Rich, R. M. 1988, AJ, 95, 828

Rich, R. M., Howard, C., Reitzel, D. B., Zhao, H., & de Propris, R. 2007, ArXiv e-prints, 710

Rutledge, G. A., Hesser, J. E., & Stetson, P. B. 1997, PASP, 109, 907

Sadler, E. M., Rich, R. M., & Terndrup, D. M. 1996, AJ, 112, 171

Smith, G., & Drake, J. J. 1988, MNRAS, 231, 115

Sosin, C., Piotto, G., Djorgovski, S. G., King, I. R., Rich, R. M., Dorman, B., Liebert, J., & Renzini, A. 1997, in Stellar Ecology: Advances in Stellar Evolution,, 92–95

Stanek, K. Z., Udalski, A., Szymanski, M., Kaluzny, J., Kubiak, M., Mateo, M., & Krzeminski, W. 1997, ApJ, 477, 163

Stetson, P. B. 1987, PASP, 99, 191

Sumi, T., Wu, X., Udalski, A., Szymański, M., Kubiak, M., Pietrzyński, G., Soszyński, I., Woźniak, P., Żebruń, K., Szewczyk, O., & Wyrzykowski, Ł. 2004, MNRAS, 348, 1439

Szymanski, M. K. 2005, Acta Astronomica, 55, 43

Terndrup, D. M., Popowski, P., Gould, A., Rich, R. M., & Sadler, E. M. 1998, AJ, 115, 1476

Terndrup, D. M., Sadler, E. M., & Rich, R. M. 1995, AJ, 110, 1774

Tolstoy, E. 2005, 118

Weiner, B. J., & Sellwood, J. A. 1999, ApJ, 524, 112

Zhao, G., Qiu, H. M., & Mao, S. 2001, ApJ, 551, L85

Zinn, R. 1985, ApJ, 293, 424

Zoccali, M., Hill, V., Lecureur, A., Barbuy, B., Renzini, A., Minniti, D., Gómez, A., & Ortolani, S. 2008, A&A, 486, 177

Zoccali, M., Lecureur, A., Barbuy, B., Hill, V., Renzini, A., Minniti, D., Momany, Y., Gómez, A., & Ortolani, S. 2007, 241, 73

Zoccali, M., Renzini, A., Ortolani, S., Greggio, L., Saviane, I., Cassisi, S., Rejkuba, M., Barbuy, B., Rich, R. M., & Bica, E. 2003, A&A, 399, 931

Chapter 4

Fabry-Perot System for 10-m Class Southern African Large Telescope

The material in this chapter also appears in print as "An Imaging FABRY-PROT System for the Robert Stobie Spectrograph on the Southern African Large Telescope", Rangwala et al. 2008, AJ, 135, 1825.

4.1 Introduction

The Southern African Large Telescope (SALT) is a 10-meter class telescope owned and operated by an international consortium of partners. The telescope design (Stobie, Meiring & Buckley (2000); Swat et al. (2003); Buckley et al. (2003)) is a modification of the Hobby-Eberly Telescope, employing a multi mirror spherical primary that is held fixed during an observation. A prime-focus tracker follows the image and contains a spherical aberration corrector and instruments. The Robert Stobie Spectrograph (RSS) Burgh et al. (2003); Nordsieck et al. (2003); Kobulnicky et al. (2003); Smith et al. (2006) is a prime-focus spectrograph providing long-slit, multi-object, and imaging spectroscopic modes, together with polarimetric capability. The RSS was designed, built and commissioned as a collaboration between groups from the University of Wisconsin and Rutgers University.

One of the goals of the RSS is to provide imaging spectroscopic capabilities for SALT, using Fabry-Pérot (FP) technology. The Rutgers group has extensive experience in this field, having provided the Rutgers Fabry-Pérot (RFP) instrument Schommer et

al. (1993) at the Cerro Tololo Observatory for many years, and designing a new FP instrument, ARIES, for the SOAR telescope Cecil (2000). The RSS FP system represents an evolution of these designs, adapted for the characteristics of the SALT telescope and the scientific requirements of the SALT partners. The major design goals of the system are to provide spectroscopic imaging over the full $8'$ field of view of the telescope, at a variety of spectral resolutions ranging from 500 to 12500, over the wavelength range from 430 to 860 nm.

The use of FP technology in astronomy for imaging spectroscopy has evolved over the years and is now being successfully employed on a regular basis by many groups around the world for galactic and extragalactic studies. The first use of the FP in astronomy was by Fabry himself (Buisson, Fabry & Bourget (1914)) to study the Orion nebula. De Vaucouleurs developed the "galaxymeter" (de Vaucouleurs, de Vaucouleurs & Pence (1974)) for measuring galaxy rotation curves. In the 1980s, a series of Taurus FP systems were developed and used at several large telescopes (Atherton et al. (1982)). Other systems followed, including the Ohio state imaging FP spectrometer (Richard et al. (1995)), the Goddard FP imager (Gelderman, Woodgate & Brown (1995)), the Hawaii imaging FP interferometer (Bland & Tully (1989)), and the Wisconsin H-alpha imager (Tufte et al. (1998)). The Taurus tunable filter (Bland-Hawthorn & Jones (1998)) pioneered the use of FP techniques for lower resolution studies, followed by the NACO FP tunable filter at VLT (Hartung et al. (2004)) and the Magellan-Maryland tunable filter. The UNSWRIF system (Ryder et al. (1998)) extends FP technology into the near infrared.

This paper documents the design of the SALT RSS FP system and its characteristics as measured in our laboratory. It is organized as follows: in section 4.2 we review the basic properties of the FP interferometer; in section 4.3 we present the design of the FP subsystem for the SALT RSS; we present the results of our laboratory testing of the FP etalons in section 4.4; we discuss the unanticipated effects of the coatings in section 4.5

and conclude in section 5. In a subsequent paper we plan to describe the commissioning of the FP subsystem on SALT and document its performance characteristics in the observing environment.

4.2 Basic Principles and Characteristics of a Fabry-Pérot Interferometer

4.2.1 Ideal Fabry-Pérot

A FP etalon consists of a pair of parallel glass plates and works on the principle of multiple beam interference. High reflectivity coatings are applied to the inner surfaces of the plates, and anti-reflection coatings are applied to the outer surfaces. Light entering the etalon at an angle θ will undergo multiple reflections between the plates, resulting in an interference pattern, subject to the following condition:

$$2d\cos\theta = N\lambda \tag{4.1}$$

where d is the gap between the plates, θ is the incident angle relative to the plate normal, N is the order of interference, and λ is the wavelength of the light in the gap medium ($\lambda = \lambda_0/\mu$, where λ_0 is the wavelength in vacuum and μ is the refractive index). The separation between any two consecutive orders of interference is called the free spectral range (FSR), which is related to the gap by

$$FSR = \frac{\lambda^2}{2d} \tag{4.2}$$

The transmission function of an ideal FP is an Airy function (top panel of Figure 4.1) given by

$$I_T = I_0 \frac{T^2}{(1-R)^2} \frac{1}{1 + F\sin^2(\Delta/2)} \tag{4.3}$$

where I_0 is the intensity of the incident beam, R and T are the reflectance and transmittance of the high reflectance coatings, $\Delta = 4\pi d\cos\theta/\lambda$ is the phase difference between

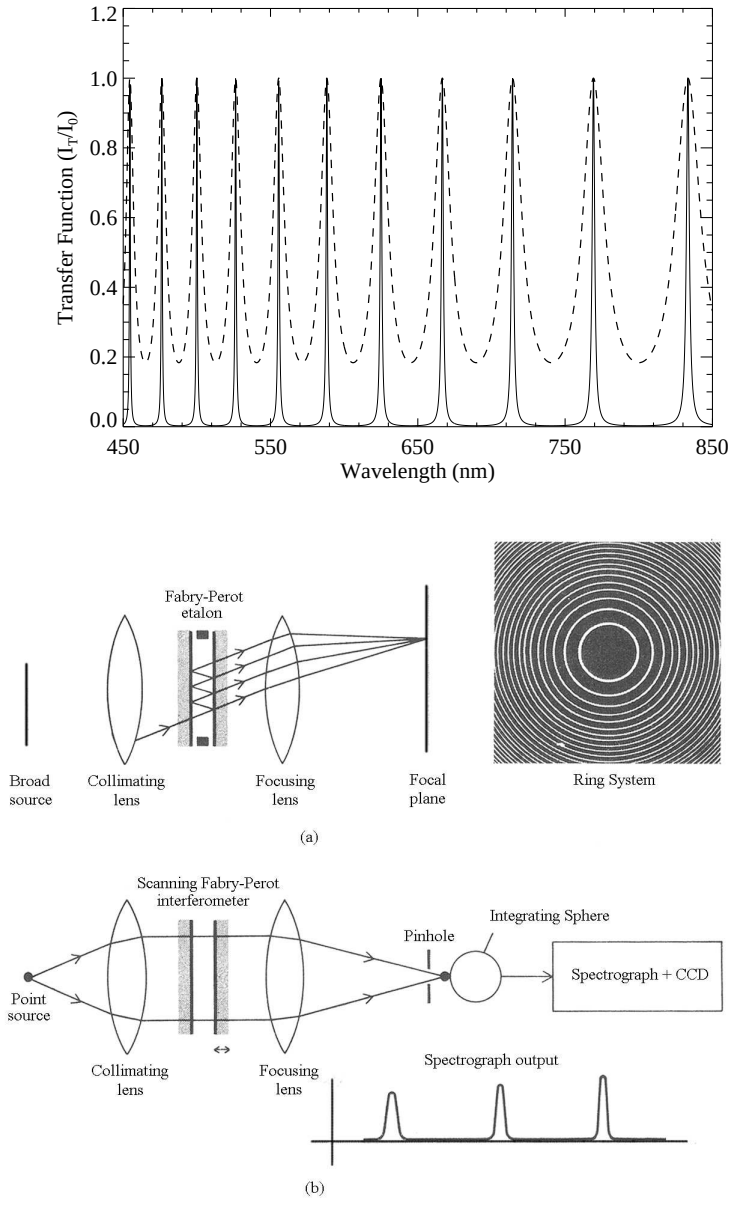

Figure 4.1 Top: The Airy function (eq. 4.3) transmission profiles of ideal Fabry-Pérot etalons with $d = 5\mu$m and $R = 0.8$ (solid) & 0.45 (dashed). Note that the FSR increases as wavelength increases. Bottom: Figure taken from Fowles (1989) (used with permission): (a) an extended source of light produces a concentric ring pattern and (b) laboratory setup for measuring etalon properties.

two successive reflections, and $F = 4R/(1-R)^2$. (Note that ideal coatings will have no absorption or scattering, so $T = 1 - R$ and the peak transmission of the etalon is 100%.)

Finesse is a measure of sharpness of the interference fringes and is measured experimentally by the ratio of the FSR to the full width at half maximum (FWHM) of the transmission profile. For an ideal etalon, the finesse is determined solely by the reflectance R and is termed the "reflectance finesse", $\mathcal{F}_R$:

$$\mathcal{F}_R = \frac{\pi}{2}\sqrt{F} = \pi\frac{\sqrt{R}}{(1-R)} \tag{4.4}$$

The spectral resolving power of the FP is given by

$$\mathcal{R} \equiv \frac{\lambda}{\delta\lambda} = N\mathcal{F}_R \tag{4.5}$$

Therefore the resolving power can be increased by either increasing the order of the interference ($N \propto 2d/\lambda$) or by increasing the reflectance of the coatings.

In the case of an extended monochromatic light source the interference pattern takes the form of a ring of radius r, with $\lambda \propto 1/r^2$. If the illumination subtends a sufficiently large range of angles θ, then multiple concentric rings of successive orders are formed (bottom panel of Figure 4.1(a)). The transmitted wavelength can be selected by either changing the gap spacing (mechanical scanning) or by changing the index of the medium in the gap (pressure scanning). In this way the FP etalon acts as a tunable narrow band filter.

4.2.2 Practical Fabry-Pérot

Practical high-reflectance coatings will have some non-zero absorption coefficient A, making the transmission $T = 1 - R - A$. The expression for the etalon transmission is still given by equation 4.3, but the maximum transmission is no longer 100%. The effect of absorption is to lower the transmission of the fringes, but does not affect the finesse or spectral resolution of the etalon. To minimize the absorption A, most current

astronomical FP systems employ multi-layer dielectric coatings. A typical value of A for such coatings is 0.005; for $R = 0.90$, the maximum transmission is reduced to 90%. It is usually desirable for the coatings to have as broad a spectral bandwidth as possible; current designs can achieve an octave in bandwidth, but typically degrade rapidly at longer or shorter wavelengths.

While the plates of the FP interferometer are highly polished, they are not perfectly flat. This non-flatness gives rise to a defect finesse ($\mathcal{F}_D$). The effective finesse, $\mathcal{F}$, of the etalon is then the combination of the reflectance finesse and the defect finesse given by

$$\frac{1}{\mathcal{F}^2} = \frac{1}{\mathcal{F}_R^2} + \frac{1}{\mathcal{F}_D^2} \tag{4.6}$$

Three common types of defects are: (1) curvature in the plates ($\mathcal{F}_{Dc}$), (2) surface irregularities or plate roughness ($\mathcal{F}_{Dr}$) and (3) departure from parallelism ($\mathcal{F}_{Dp}$). Atherton et al. (1981) give the following expressions for these defects:

$$\mathcal{F}_{Dc} = \frac{\lambda}{2\delta t_c} \tag{4.7}$$

$$\mathcal{F}_{Dr} = \frac{\lambda}{4.7\delta t_r} \tag{4.8}$$

$$\mathcal{F}_{Dp} = \frac{\lambda}{\sqrt{3}\delta t_p} \tag{4.9}$$

where δt_c, δt_r, δt_p are measures of the deviations for their respective defects. The expression for $\mathcal{F}_{Dc}$ assumes spherical curvature; in general, the curvature can have a complicated shape. The total defect finesse is the combination of all the above defects

$$\frac{1}{\mathcal{F}_D^2} = \frac{1}{\mathcal{F}_{Dc}^2} + \frac{1}{\mathcal{F}_{Dr}^2} + \frac{1}{\mathcal{F}_{Dp}^2} \tag{4.10}$$

In addition to physical defects, optical effects in multi-layered reflection coatings can produce additional *apparent* distortions of the plates. This effect is discussed in detail in later sections. Any departure from flatness, either physical or apparent, will lower the overall finesse, spectral resolution and transmitted intensity of the etalon.

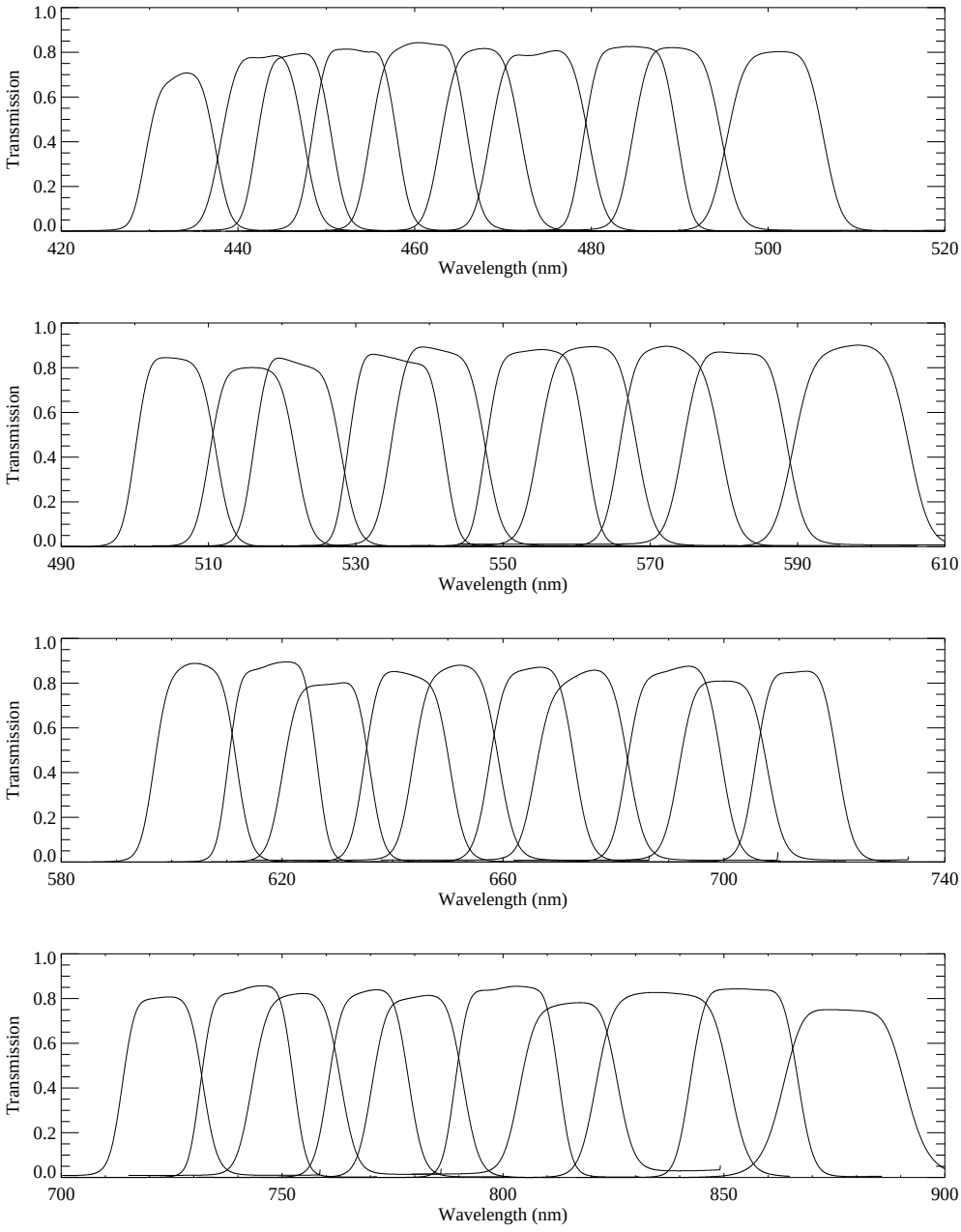

Figure 4.2 Transmission curves of the order selecting interference filter set

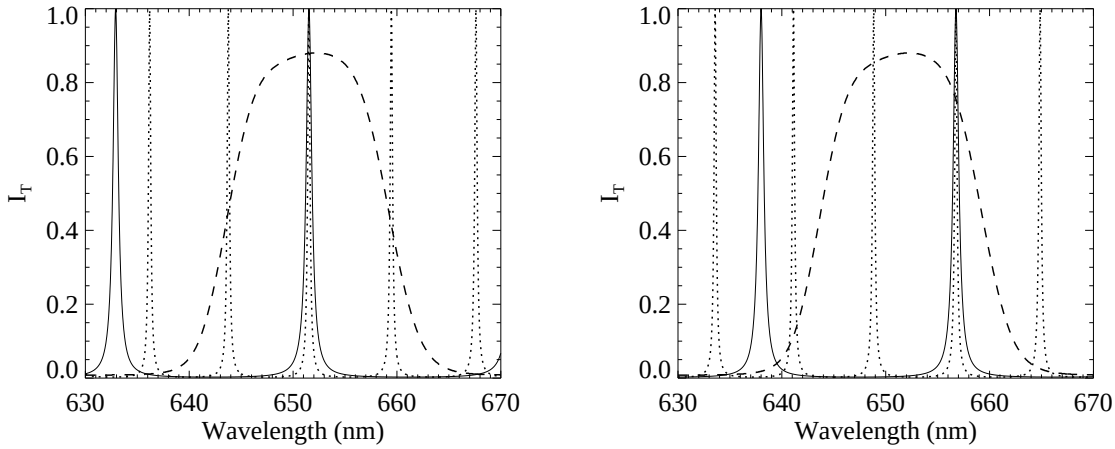

Figure 4.3 Order selection with interference filter and dual etalons. Solid curve: SG etalon; dashed curve: filter; dotted curve: MG etalon.

4.3 FP System for SALT

The design goals for the SALT FP system are to provide spectroscopic imaging over a wide range of wavelengths and spectral resolutions, while fitting within the size, weight, and budget constraints of the RSS. A survey of the SALT user community showed there was interest in programs at wavelengths extending from the ultraviolet atmospheric limit to the near-infrared. We could not accommodate this wide spectral range with a single set of etalon coatings, and chose a bandwidth of $430 - 860$ nm, leaving the range of shorter wavelengths for a possible future set of etalons. The SALT user survey also showed interest in a wide range of spectral resolutions, so we decided on a system employing three etalons, with gap spacings of 5, 27, and 135 μm, providing spectral resolutions at 650 nm of 500, 2500, and 12500, respectively. We shall subsequently refer to these etalons as SG, MG, and LG (for small, medium and large gap). The diameter of the collimated beam in the RSS is 150 mm, so etalons with this clear aperture are required. It is difficult to obtain etalon plates of this size with surface quality better than $\lambda/100$, so $\mathcal{F}_D \sim 50$. We chose a reflectance $R = 0.90$ for the coatings, giving $\mathcal{F}_R = 30$, and the combined effective finesse $\mathcal{F} \sim 25$.

A blocking filter is required to select the desired transmission order of the FP etalon.

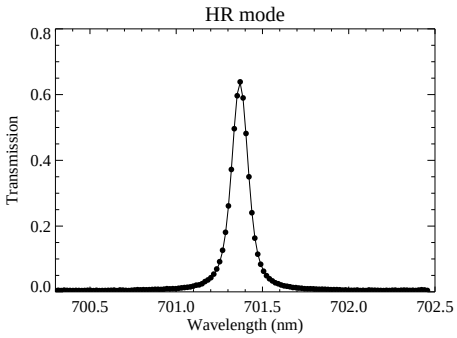

Figure 4.4 Transmission profile of the LG etalon is well represented by a Voigt function (solid line)

For the low resolution etalon SG, with larger FSR, a reasonable number of standard interference filters can be used to isolate the orders. We designed a set of filters to isolate each of the orders of the SG etalon within our wavelength range. The filters are 4-period designs to give relatively flat-topped transmission profiles with steep sides. The design goal is to choose filter central wavelengths and widths so that in the worst case, when the etalon is tuned to the cross-over wavelength between adjacent filters, the filter adequately suppresses the transmission of the neighboring order of the etalon. The filter set consists of 40 filters, whose measured transmission curves are shown in Figure 4.2.

The transmissions are typically 80% or better, less at the crossover wavelengths between adjacent filters. Since the etalon FSR increases with wavelength, the filters are narrower and more closely spaced at the short wavelength end of the range. Manufacturing tolerances have produced some gaps in the set where the transmission at the crossover wavelength is unacceptably low; additional filters will be purchased in the future to fill these gaps.

An example of the filter blocking for the SG etalon is shown in Figure 4.15, where the solid curve is the transmission of an ideal etalon of gap 11 μm and the dashed curve is the measured transmission of one of the filters. The left panel shows the etalon tuned to the central wavelength of the filter, and the adjacent orders are highly blocked. The

right panel shows the worst case when the etalon is tuned to the crossover wavelength to the next filter, and the "parasitic light" leakage of the adjacent order is a few percent.

For the higher resolution etalons with their smaller FSR, the blocking scheme discussed above becomes impractical, requiring a very large number of narrow (hence expensive and lower peak transmission) filters. We thus decided to employ a dual etalon system for the higher resolution modes. Either the MG or LG etalon is used in series with the SG etalon and one of the blocking filters discussed above. The SG etalon is tuned to the same wavelength as the higher resolution etalon, and suppresses its adjacent orders. As above, the filter suppresses the adjacent orders of the SG etalon. The scheme is illustrated in Figure 4.15, where an idealized MG etalon (27 μm gap) transmission is shown by the dotted curve. The total transmission (not shown in the figure for clarity) is the product of the three curves. Parasitic light is highly suppressed in the medium resolution mode. In the highest resolution mode, the wings of the SG transmission do not fully block the adjacent orders of the LG etalon, producing parasitic light of typically 5%. The dual etalon design makes it possible to select any desired wavelength within the coating bandpass, and at any of the etalon resolutions, with a limited number (40) of interference filters.

We selected IC Optical Systems Ltd (ICOS) to supply the etalons and their controllers. Each etalon is controlled by a three-channel system that uses differential capacitance micrometers and piezo-electric actuators, incorporated into the etalon, to monitor and correct errors in plate parallelism and spacing. Two channels (X and Y) control the parallelism using capacitor pairs optically contacted to the etalon plates. The third channel (Z) sets and maintains the spacing between the plates by comparing another capacitor optically contacted to the plates to a fixed-gap reference capacitor. Since all the measurements are differences between air-gap capacitors within the ambient etalon environment, they are highly stable and relatively immune to the influence of changing temperature, humidity, etc. The system can move the plates over a range

of ~ 6 μm with a resolution of 0.49 nm.

The range of the piezo-electric actuators is sufficient to change the gap of the SG etalon by a factor of two, allowing this etalon to be operated in two different spectral resolution modes. Thus the system provides four distinct spectral resolutions. Setting the SG etalon to its smallest gap ($\sim$5 μm) produces the Tunable Filter (TF) mode with $\mathcal{R} \sim 350$, and setting it to its largest gap ($\sim$11 μm) produces the Low Resolution (LR) mode with $\mathcal{R} \sim 750$. For the larger gap etalons, the piezo actuators cannot change the gap enough to produce significantly different resolutions, and we choose to operate the etalons near their largest gap settings for maximum resolution. Setting MG etalon to its largest gap ($\sim$28 μm) produces Medium Resolution (MR) mode, with $\mathcal{R} \sim 1500$. Setting LG to its largest gap ($\sim$136 μm) produces High Resolution (HR) mode, with $\mathcal{R} \sim 8500$. Details on these modes are presented in section 4.4.

4.4 Lab Testing

The characterization and calibration of the FP system was carried out in our lab at Rutgers University. The test setup, shown schematically in right panel of Fig. 4.1(b), consisted of a pair of telescopes, each with 1200 mm focal length and 150 mm aperture, used as a collimator and a camera. The etalons were mounted on a slide that allowed them to be positioned into and removed from the collimated beam. The light source used was a 100 W quartz halogen lamp. The transmitted light was fed into an integrating sphere that illuminated the entrance slit of a 0.5m spectrograph with a CCD detector. The spectrograph allows to measure the transmission profile of the FP over several orders in a single spectrogram. A typical output transmission profile as shown in Figure 4.4 was fit very well by a Voigt function, providing the central wavelength and FWHM of each individual order. The spectrograph used three gratings that provided spectral resolutions of 0.25 nm, 0.08 nm, and 0.04 nm. The TF and LR modes, with 13 and 26 orders respectively, were measured with the 0.25 nm resolution. The MR

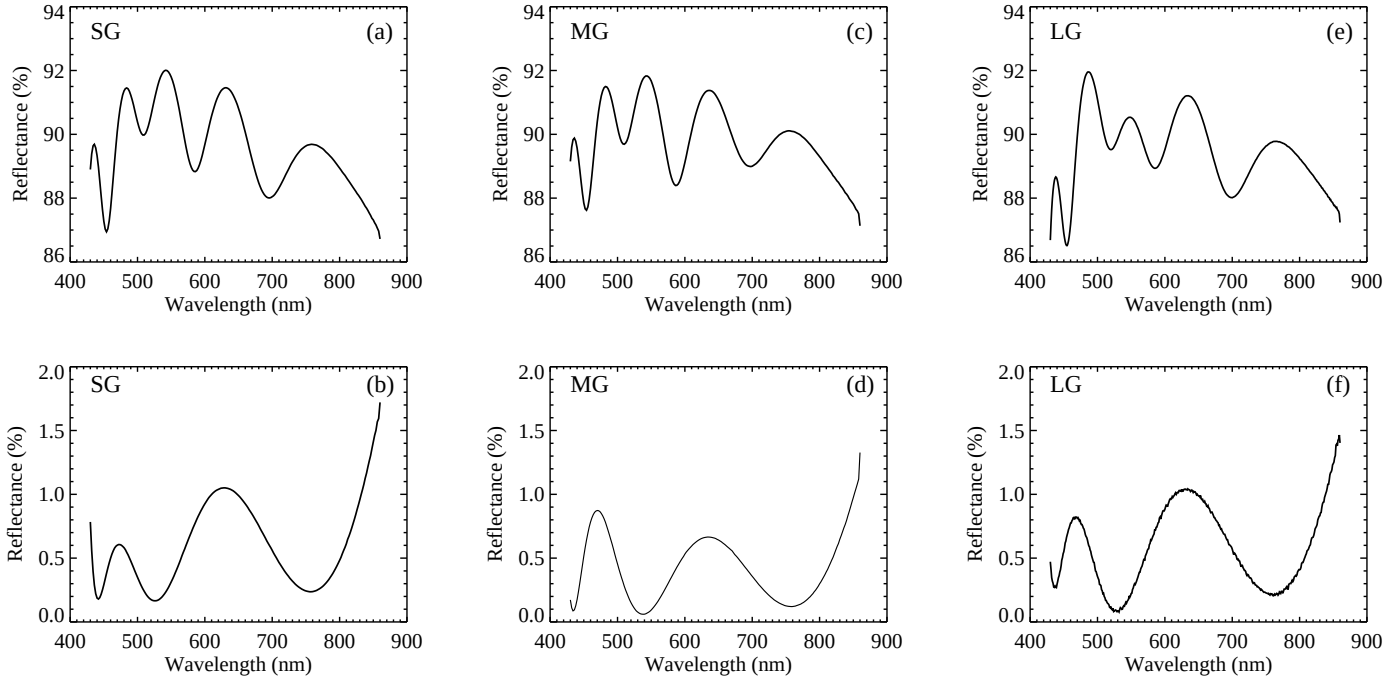

Figure 4.5 High reflection and anti-reflection coating curves of the etalon plates, provided by ICOS.

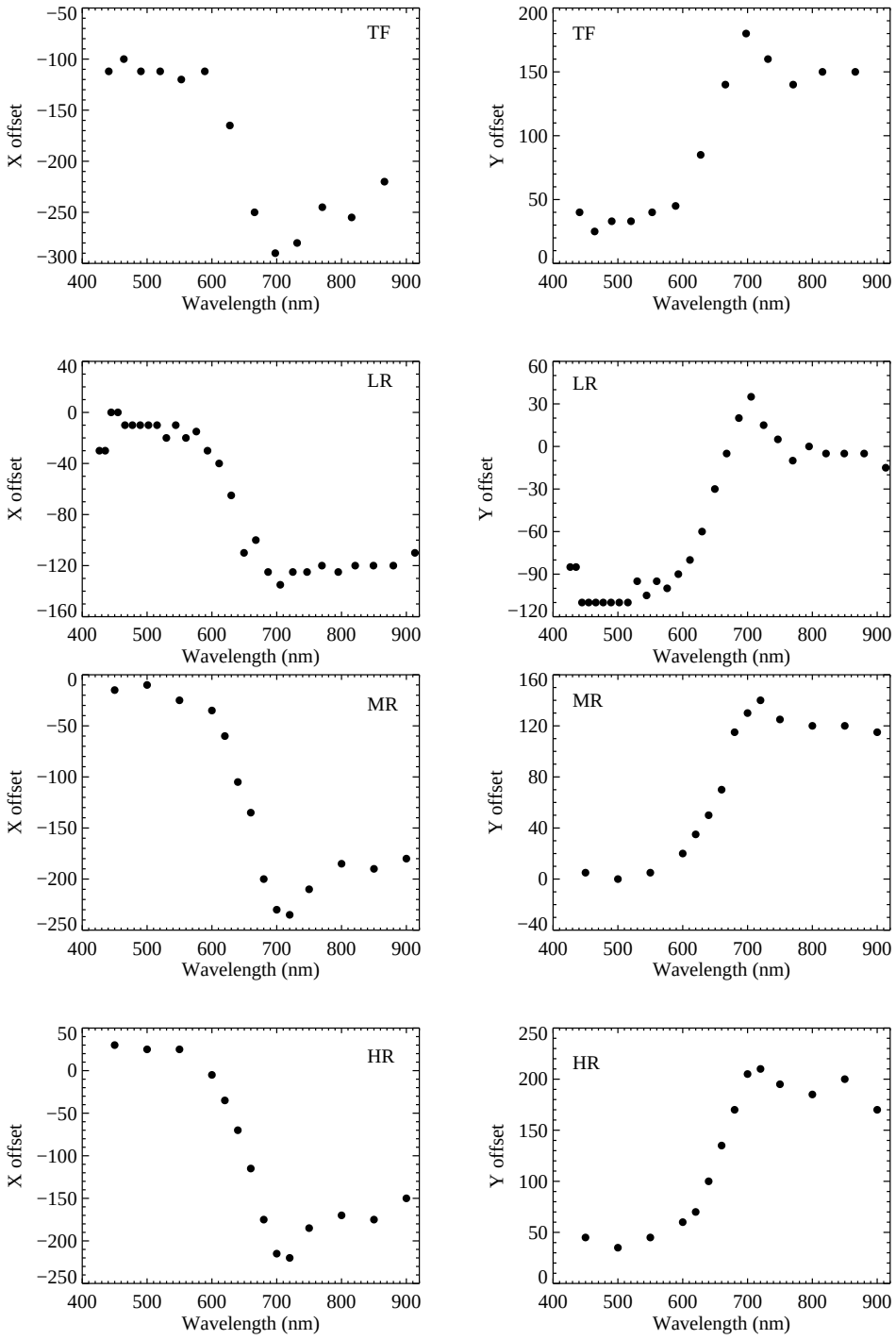

Figure 4.6 X and Y parallelism curves for the four spectral modes show that the parallelism settings are wavelength dependent with maximum variation between 600 nm and 720 nm.

mode with 72 orders was measured with a combination of the 0.25 nm and 0.08 nm resolution. The HR mode with 330 orders was measured with a combination of the 0.08 nm and 0.04 nm resolution. The measured characteristics of all modes and orders are listed in Table 4.1.

We do not have the facilities in our lab to measure directly the properties of the etalon coatings. Figure 4.5 shows the measurements supplied by ICOS of the high reflection coatings at the etalon gaps and the anti-reflection coatings on the outer surfaces for each of the three etalons. The coatings meet our specifications of $90 \pm 4\%$ and $< 1\%$, respectively.

4.4.1 Results

Parallelism, FSR and Effective Gap

The two plates of the etalon should be as parallel to each other as possible in order to achieve maximum resolution and transmission. The parallelism is adjusted by changing the X and Y offsets of the controller, the optimal values of which are obtained when the transmission profiles are most symmetric and sharpest[1]. These values of X and Y are listed in Table 4.1 and plotted in Figure 4.6. The precision of our determination of the optimum parallelism setting is ± 10 units. For an ideal etalon, the parallelism settings will be wavelength independent. However, we found that in all four modes the parallelism settings are constant at shorter wavelengths, vary between 600 – 750 nm, and are again constant (but at different values) at longer wavelengths. As seen in Figure 4.6, the shapes of the parallelism setting curves are remarkably similar for all three etalons and all four resolution modes.

The effective gap of the etalon can be determined by measuring the FSR between a pair of consecutive transmission orders, and applying equation 4.2. The results,

[1]The control system settings can be affected by environmental conditions like temperature and humidity. More testing will be carried out in the telescope environment during the commissioning of the instrument to check its stability.

Table 4.1 Properties of the TF, LR, MR and HR modes.

Wavelength (nm)	FWHM (nm)	FSR (nm)	finesse	resolution	gap (d) (nm)	X offset	Y offset
440.875	1.595	23.270	14.60	276	4.18	-112	40
464.144	1.823	24.810	13.60	255	4.34	-100	25
490.500	1.663	28.040	16.90	295	4.29	-112	33
520.218	1.888	31.160	16.50	276	4.34	-112	33
552.812	1.912	34.410	18.00	289	4.44	-120	40
589.043	2.353	37.440	15.90	250	4.63	-112	45
627.701	1.973	38.380	19.50	318	5.13	-165	85
665.800	2.033	35.040	17.20	327	6.33	-250	140
697.783	1.874	32.830	17.50	372	7.42	-290	180
731.461	1.847	36.280	19.60	396	7.37	-280	160
770.346	2.093	42.060	20.10	368	7.05	-245	140
815.590	2.514	47.930	19.10	324	6.94	-255	150
866.214	3.093	50.620	16.40	280	7.41	-220	150
			LR Mode				
426.480	1.173	8.930	7.60	364	10.18	-30	-85
435.412	0.621	9.310	15.00	701	10.18	-30	-85
444.605	0.660	10.000	15.20	674	9.88	0	-110
454.946	0.703	10.650	15.10	647	9.72	0	-110
465.886	0.699	11.220	16.10	667	9.67	-10	-110
477.368	0.612	11.760	19.20	780	9.69	-10	-110
489.406	0.630	12.360	19.60	777	9.69	-10	-110
502.079	0.677	13.010	19.20	742	9.69	-10	-110
515.371	0.710	13.690	19.30	726	9.70	-10	-110
529.743	0.706	14.380	20.40	750	9.76	-20	-95
544.213	0.698	15.080	21.60	780	9.82	-10	-105
559.896	0.751	15.840	21.10	746	9.90	-20	-95

Note. — Table 4.1 is published in its entirety in the electronic edition of the *Astronomical Journal*. A portion is shown here for guidance regarding its form and content.

displayed in the left panels of Figure 4.7, show that in all four modes, the effective gap increases by about 3 μm in the same 600 – 750 nm wavelength range in which the parallelism settings change. Plotting the FSR as a function of wavelength, shown in the right panels of Figure 4.7, illustrates the same effect. The dashed and dot-dashed curves are plots of equation 4.2 for the best-fit values of the gap at short and long wavelengths, respectively. In all four modes at short wavelengths the FSR exhibits the quadratic increase with wavelength characteristic of a fixed gap. Between 600 nm and 750 nm the curves show inflections. At longer wavelengths the FSR curve again becomes quadratic, but with a larger fixed gap. Again, the shape of the change of the effective gap is remarkably similar for all the etalons.

The variation of effective gap and parallelism with wavelength is most likely due to the complex structure of the high reflective coatings that are required to achieve the broad bandwidth from 430 nm to 860 nm of our specification. Similar wavelength dependent effects were also seen by Ryder et al. (1998) with 70 mm aperture etalons. This unexpected behavior of the coatings will have effects on other properties of the etalon as well and is discussed in detail in section 4.5.

Plate Flatness

As discussed in section 4.2.2, the finesse and resolution can be affected by deviations from plate flatness. We measured the effective shape of the plates along the X and Y axis of the etalon by reducing the illuminating aperture of the collimated beam to 25 mm diameter and recording spectra of the etalon transmission at a series of positions across the etalon. The measuring positions were spaced by steps of approximately 20 mm, producing 7 locations along the axis. The etalon was then physically rotated 90° to measure along the other axis. The effective gap at each position was determined using equation 4.1. The shape of the plates is expressed as the change in the gap from that at the center of the plates. The measurements are plotted in Figure 4.8.

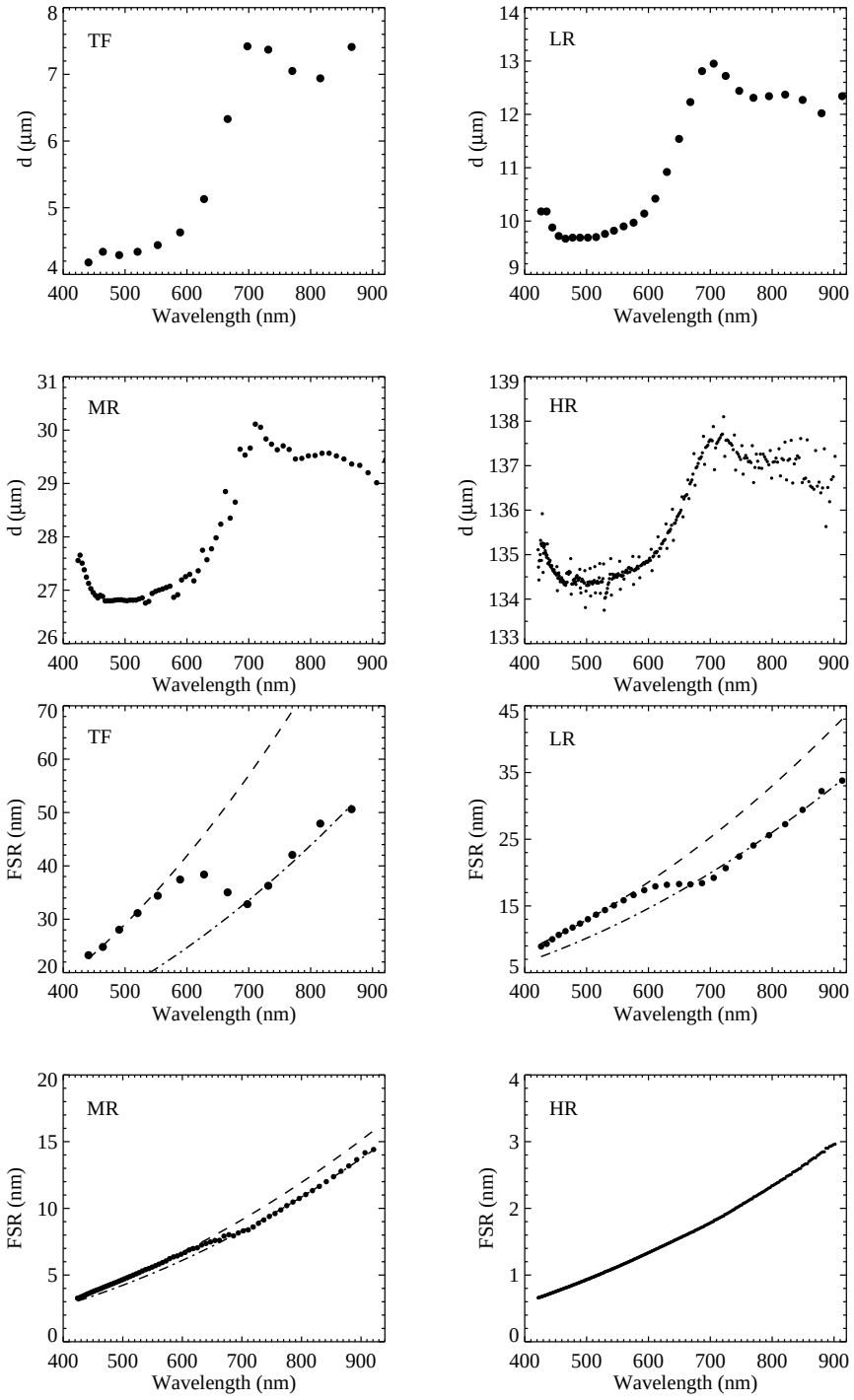

Figure 4.7 Left: The effective gap also shows wavelength dependence with maximum variation between 600 nm and 720 nm. Right: FSR changes quadratically with wavelength for a fixed d. The FSR curve shows inflection between 600 nm and 720 nm because the effective gap changes.

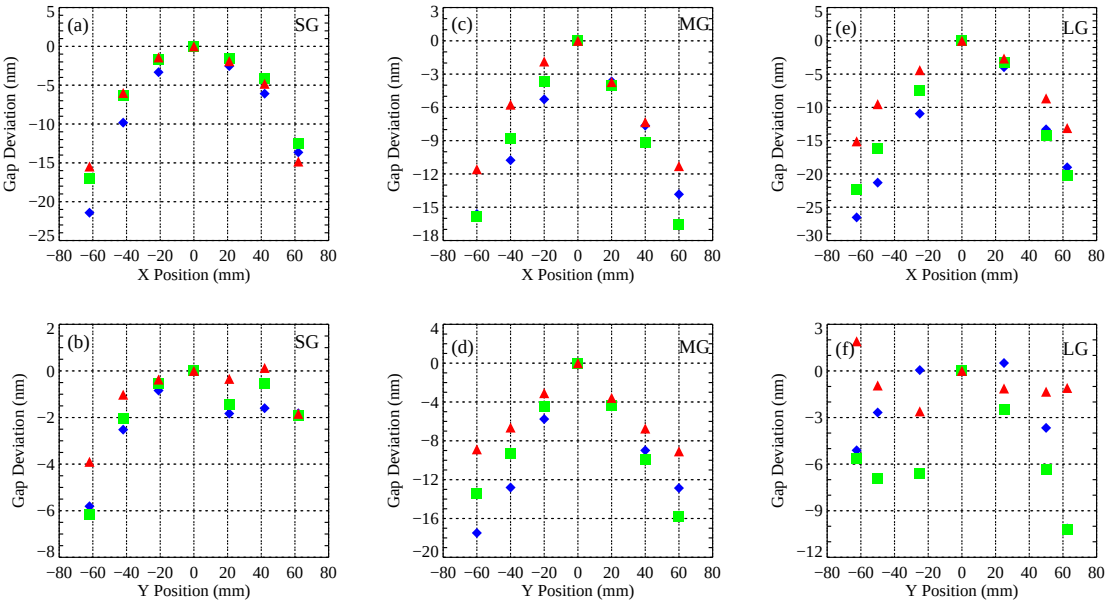

Figure 4.8 Measurements of the effective shape of the etalon plates for the three etalons. The red triangles, green squares and blue diamonds show the relative gap at 850, 650 and 500 nm respectively.

For all three etalons, the effective gap decreases away from the center. Moreover, this trend is generally wavelength dependent with the plates somewhat flatter in the red than in the blue.

For the SG etalon, the plates exhibit roughly spherical curvature of approximately 15 nm along the X-axis, but are flat along the Y-axis to within ±1 nm over most of the aperture, with a turned-down edge of about 6 nm on one side. The weighted RMS deviation from the center (weighting by the area of annular sectors) is about 8 nm at 650 nm ($\lambda/80$). For the MG etalon, the effective shape along both the X and Y axes is more conical (i.e. the gap decreases roughly linearly with radius), with a weighted RMS deviation of 12.2 nm ($\lambda/54$). Finally for the LG etalon, the deviation along the X-axis is greater and more conical in the blue, smaller and more spherical in the red. Along the Y-axis the plates are effectively flat and show no distinct shape. Therefore the overall shape of the plates resembles that of a half cylinder. The weighted RMS deviation at 650 nm is 13 nm ($\lambda/50$).

The effective shape measured here is not representative of the actual physical flatness of the plates since interferograms of the plates taken by ICOS after polishing but before coating showed flatness of $\lambda/100$ or better for all the plates. As discussed in Section 4.5, this apparent curvature is likely due to an optical effect of the reflection coatings.

Finesse and Resolving Power

The significant deviations from flatness discussed in the previous section produce lower than expected finesse and spectral resolution. If the only contribution to the total finesse comes from $\mathcal{F}_R$, then using $R \sim 0.9$ (the average value from the coating curves in Figure 4.5) and equation 4.4 we would expect a finesse of $\mathcal{F} \sim 30$. But the measured finesse is less than the expected finesse because of the contribution of defect finesse. The measured finesse for each of the three etalons is plotted as a function of wavelength in Figure 4.9.

For each etalon, we calculate a finesse curve using $\mathcal{F}_R$ from the measured reflectivity, $\mathcal{F}_D$ for spherical curvature, and equation 4.6. We assume the amplitude of the curvature defect is constant with wavelength. Then we either use the measured weighted RMS value discussed in the previous section, producing the dotted curves in the figure, or adjust the amplitude to optimize the fit, producing the solid curves.

For the SG etalon, the curve based on the measured defect amplitude of $\lambda/80$ has the correct shape, but overestimates the actual finesse values. Adjusting δt_c to be 10.8 nm ($\lambda/60$ at 650 nm) in equation 4.7 yields the solid curve that fits the measured finesse very well. This is our best definition of the effective flatness of the plates for this etalon.

For the MG and LG etalons the shapes of the calculated curves do not agree as well with the measured finesse distributions. As noted in the previous section, both the shape and the amplitude of the surface defects change with wavelength, and these complications are not included in the calculations. For both etalons the solid curve

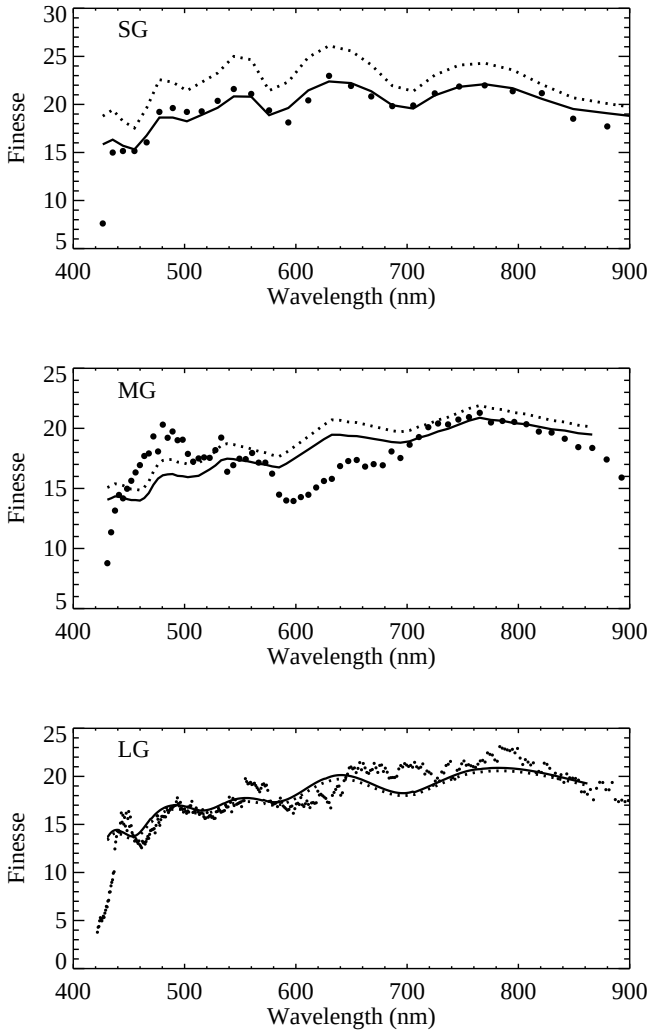

Figure 4.9 Finesse as a function of wavelength. Points represent the measured finesse. The curves are calculated from the reflectivity and measured (dotted) or fitted (solid) defect amplitude.

λ (nm)	R	d (μm)	$I_T^{c\,\mathrm{theory}}$ (%)	I_T^{obs} (%)
440.0	0.892	4.18	68	66
455.2	0.886	4.34	72	68
505.0	0.912	4.29	64	57
555.0	0.916	4.44	65	58
579.0	0.888	4.63	79	72
641.5	0.914	5.13	72	63
665.1	0.896	6.33	80	63
705.2	0.880	7.42	86	75
735.2	0.892	7.37	84	77
783.5	0.896	7.05	85	78
815.2	0.885	6.94	88	81

Table 4.2 This table makes comparison between the transmitted intensity calculated from equation 4.14 (column 4) and the observed transmission values for the LR mode (column 5).

is calculated with a flatness of $\sim \lambda/49$ at 650 nm, which is very close the measured weighted RMS deviations of $\lambda/54$ and $\lambda/50$.

The spectral resolution listed in Table 4.1 is calculated using $\lambda/FWHM$. It is related to the total finesse by equation 4.5. Thus the lower than expected total finesse produces lower resolving power for all three etalons. Figure 4.10 shows the spectral resolution as a function of wavelength for all four resolution modes. The spectral resolution for the LR, MR and HR modes is 780, 1500 and 8500 at 650 nm, respectively. Because these modes operate at their largest possible gap setting, there is no way to increase the resolving power. The lowest resolution TF mode has a resolving power of 350 at 650 nm. Since it is unwise to operate the etalon with a smaller gap (to avoid bringing the plates into contact and damaging the plates and/or their coatings), this is the lowest resolution available.

Transmission

The deviation of the plates from flatness also produces a decrement of the peak transmission. For an ideal FP interferometer, the transmitted amplitude can be written

as:

$$U_t = T\sum_{m=0}^{\infty} R^m \exp\left(i\frac{4\pi}{\lambda} md\mu\cos\theta\right) \tag{4.11}$$

where $T = 1 - R$ in absence of absorption. The product $U^{\dagger}U$ gives the following transmitted intensity (Vaughan 1989):

$$I_t = \frac{T^2}{1-R^2}\left(1 + 2\sum_{m=1}^{\infty} R^m \cos(\frac{4\pi md}{\lambda})\right) \tag{4.12}$$

assuming $\mu = 1$ and $\theta = 0°$. This is basically the Airy function shown in Figure 4.1 (left panel). For a deviation from flatness in the form of spherical curvature, the transmitted amplitude has the following form discussed by Mahapatra & Mattoo (1986):

$$U_t^c = T\sum_{m=0}^{\infty} R^m \frac{\sin(2\pi mc/\lambda)}{2\pi mc/\lambda}\exp\left[i\frac{2\pi m}{\lambda}(2d + c)\right] \tag{4.13}$$

where c is the maximum deviation from a plane surface. Multiplying this by its complex conjugate gives the following transmitted intensity:

$$I_t^c = T^2\sum_{m=0}^{\infty} R^{2m}\frac{\sin(m\psi)}{m\psi}\left\{1 + 2\sum_{k=1}^{\infty} R^k\cos(k\phi)\frac{m}{m+k}\frac{\sin((m+k)\psi)}{\sin(m\psi)}\right\} \tag{4.14}$$

where

$$\psi = \frac{2\pi c}{\lambda} \qquad \text{and} \qquad \phi = \frac{4\pi d}{\lambda}(1 + \frac{c}{2d}) \tag{4.15}$$

equation 4.14 reduces to equation 4.12 for $c = 0$. Figure 4.11 shows the decrement in the transmitted intensity as c increases. Notice that the plate curvature also broadens and shifts the transmission peak.

We measure the transmission from the ratio of two spectra: one with the etalon in the collimated beam and the other with the etalon replaced by a 150 mm clear aperture. The measured transmitted intensities for selected orders in the TF mode are listed in column 5 of Table 4.2. The theoretical transmitted intensity is calculated using equation 4.14 with $c = \delta t_c = \lambda/80 = 8$ nm at 650 nm (taken from section 4.4.1 for the SG etalon) and is listed in column 4 of Table 4.2. Although equation 4.14 does not account fully for the complicated effective curvature of the etalon plates, the calculated

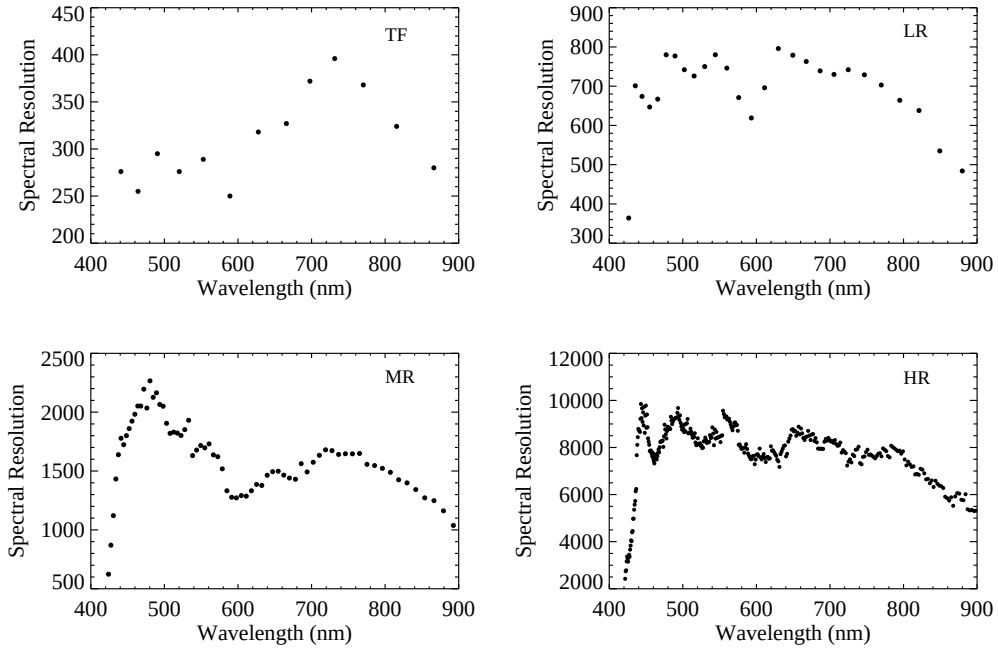

Figure 4.10 Plots of spectral resolution for the four spectral modes. The filled circles are the measured resolution for the individual orders.

transmissions compare reasonably well with those observed. The difference between the measured and calculated transmitted intensity can be used to estimate the value of absorption, A, of the coatings. We find $A \sim 0.5\%$, a typical value for multi-layer dielectric high-reflection coatings.

Wavelength Calibration

The etalon is scanned in wavelength by changing the controller Z offset value, which causes the gap size, d, to change. In the lab, we take spectra of the etalon's transmission at a range of Z settings to calibrate the Z – wavelength relation. (At the telescope, a different calibration procedure is used, where the etalon is tuned to the wavelengths of several emission lines from spectral lamps and the resulting ring patterns are measured.) We find that a low-order polynomial provides an excellent fit to the wavelength

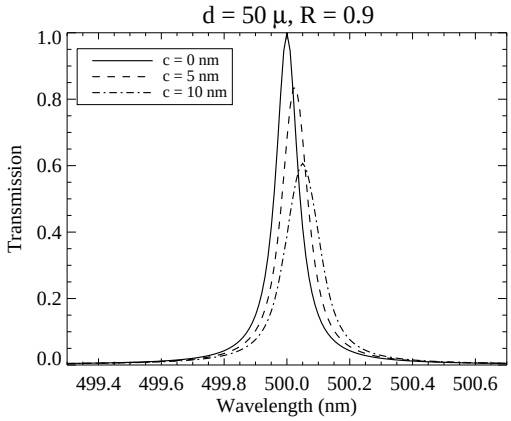

Figure 4.11 The effect of plate curvature on transmitted intensity

calibration:

$$\lambda = A + BZ' + CZ'^2 + DZ'^3, \tag{4.16}$$

where

$$Z' = \frac{Z}{1000} \tag{4.17}$$

The scanning range of the Z offset (-2048 to $+2047$) is sufficient to cover several FSRs of an etalon. For the MG and LG etalons we use this to limit the number of orders calibrated for operational simplicity while retaining the ability to tune to any desired wavelength within the available bandpass (430 to 900 nm). We calibrate 12 orders of MG and 54 of LG. Over the full Z range a cubic polynomial fits best, with residuals of less than 1/40 of the FWHM. We operate the SG etalon in two modes: TF and LR, near the minimum and maximum gap, respectively. To maintain these extremes, we limit the Z range to that required to scan a single order (-1.250 to -0.750 and $+1.260$ to $+2.000$ respectively) and calibrate every order: 13 in TF and 27 in LR. Over these restricted scanning ranges a quadratic polynomial provides an excellent fit, with residuals less than 1/50 of the FWHM.

The A coefficient is the wavelength 'zero point' and can vary with time, temperature, humidity and other environmental factors. Its stability will be studied extensively in the telescope environment during commissioning. We expect that a single zero point

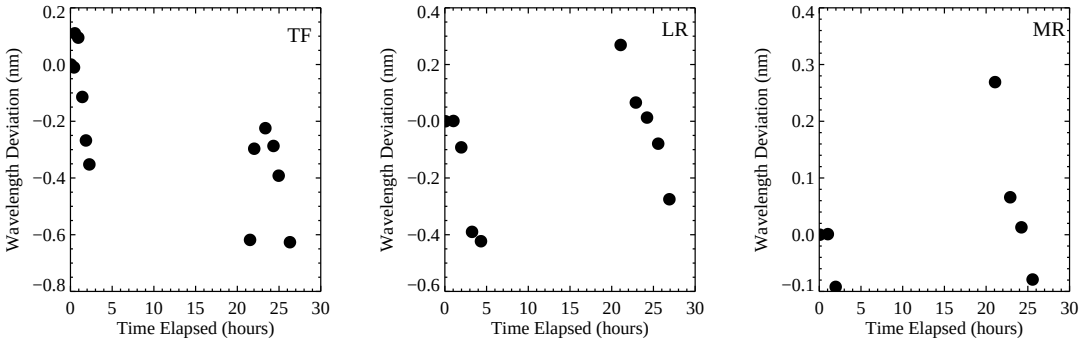

Figure 4.12 Temporal stability of the etalon zero point for TF, LR and MR modes

calibration will be required on hourly time scales while observing. Our experience suggests that the B, C and D coefficients will be very stable, requiring no more than weekly or monthly recalibration.

Stability

The wavelength stability, which is essentially the stability of the zero point A, of the etalons was measured by taking a series of spectra over a period of more than 24 hours. During this period the etalon and the controller were undisturbed mechanically and electrically and the environmental conditions (like temperature) were held approximately constant. The measurements, plotted in Figure 4.12, were carried out for the TF, LR and MR modes only. The wavelength drift for these modes were smooth and typically ~ 0.1 nm per hour. Over the entire period of measurement the RMS wavelength fluctuations in the TF, LR and MR modes were 0.24 nm, 0.22 nm, and 0.071 nm, respectively. Note an abrupt jump of 0.3 nm in the zero point of LR mode between hour 2 and 3; there was a power failure in the lab which caused the controller to reset.

Additionally, the RMS FWHM fluctuations over the entire period were 0.075 nm in TF, 0.033 nm in LR and 0.021 nm in MR modes. For the MR mode, we also measured the parallelism stability over a 7-day period. The RMS variations in the X and Y offsets over this period were 4.1 units and 2.4 units, respectively. These drifts are insignificant

because the uncertainty in determining the optimum parallelism is at least 5 units. The wavelength and parallelism stability may change with variable environmental conditions and hence will be tested at the telescope during commissioning.

4.5 Discussion: Effect of Phase Dispersion on Multi-layer Broadband Coatings

Our laboratory testing uncovered three unexpected results: wavelength-dependent parallelism changes, wavelength-dependent gap changes, and significant apparent plate curvature. We believe that all of these phenomena arise from effects in the multi-layer broadband reflection coatings of the etalons.

4.5.1 Broadband Multi-Layer Coating Design

Although the exact coating structure of our etalons is proprietary information and we are unable to present it here, we have been given access to some of the design details to simulate the properties of the real coating using multi-layer design software. The coatings comprise 16 layers of Zinc Sulphide and Cryolite and are deposited without heating the substrates. The total thickness of the coating is 1331 nm.

The evolution of coating design from the simple quarter-wave layer AR coating to the fully optimized broadband multi-layer has been facilitated by the advent of proprietary and commercial coating design algorithms. Nevertheless, coating design and deposition is still an art as well as a science, requiring experience and an intimate knowledge of the performance and properties of the coating vendors deposition chamber.

An early scheme for extending the spectral range of coatings was to combine two quarter-wave stacks on top of each other, with the two stacks optimized for different wavelength bands. To minimize scattering effects, which are usually more severe at shorter wavelengths, the upper stack was designed to reflect the shorter wavelengths,

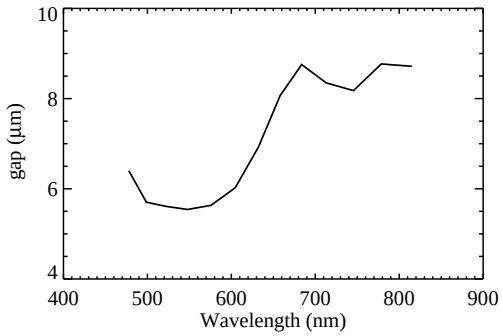

Figure 4.13 Predicted effective gap variation with wavelength, based on our coating design and a 5 μm air gap.

while the lower stack reflected the longer wavelengths. Thus longer wavelengths penetrated deeper into the coatings, giving rise to a larger effective gap at these wavelengths. While such design techniques are no longer necessary, it appears that the fully optimized coating covering our spectral range of 430–860 nm shows relics of this approach. Our measurements indicate that the transition occurs in the 600 to 720 nm wavelength region with the additional path as large as that due to the optical thickness of 2.6 μm of coating material. We have simulated this effect for our coating designs with a 5 μm air gap, producing the curve in Figure 4.13. Comparison with Figure 4.7 shows an excellent agreement of this prediction with our measurements of the effective gap. Ryder et al. (1998) observe similar effects for etalons coated for the near infrared.

4.5.2 Phase-Dispersion

In multi-layer dielectric reflectors, a wavelength-dependent phase shift (β) occurs upon reflection. Ramsay & Ciddor (1967) investigated the effect of phase-shift dispersion ($\partial\beta/\partial\lambda$) in multi-layer dielectric reflectors on the apparent shape of the reflecting surface. They report an experiment where a plate with a physical surface of $\lambda/60$ concave, when coated with a standard multi-layer reflector, showed an effective surface shape of $\lambda/60$ concave at wavelength 546 nm, flat at 588 nm, and $\lambda/10$ convex at 644 nm! The phase-shift dispersion can amplify the effects of slight irregularities in the coating

thickness or the substrate surface to produce a significant, and wavelength dependent, change in the apparent shape of the surface. Ramsay & Ciddor (1967) present a result from Giacomo (1958):

$$t_i \frac{\partial N}{\partial t_i} = -\left(\frac{4t}{\lambda} - \frac{\lambda \partial \beta}{\pi \partial \lambda}\right) \tag{4.18}$$

where t is the geometrical thickness of a multi-layer stack, i refers to the different layers and N is the interference order related to gap by equation 4.1 of this paper. The term $\frac{4t}{\lambda}$ is the geometric effect, and is independent of the phase dispersion in the coatings. Figure 4.14 shows the expected phase-shift curve as a function of wavelength for our coating design. Using this phase dispersion and $t = 1331$ nm, Equation 4.18 is plotted in the right panel of Figure 4.14; for comparison, we also show the geometrical term alone.

It is apparent from Equation 4.18 that the phase dispersion term can reduce or cancel the geometrical term, decreasing the sensitivity to surface and coating imperfections. Ciddor (1968) discusses attempts to design coatings with phase dispersions that cancel the geometric effect, and thus eliminate or significantly reduce the apparent curvature of the plates. He comments that it is very difficult (if not impossible) to simultaneously maintain a uniform high reflectivity over a broad bandwidth while producing the desired phase dispersion cancelation. Figures 4.14 and 4.5 suggest that our coatings have partially achieved this goal. The sensitivity to imperfections is reduced throughout the bandpass except for very small range between 442 nm and 448 nm where the amplification is only slightly worse than the geometrical term alone (but of the opposite sign). Throughout the red half of the bandpass the sensitivity is reduced by about a factor of 3. These results are only approximate, since we do not have the as-built details of the coatings, but we believe that they are indicative.

The manufacturing tolerance in the individual layer thickness of coatings available commercially is often quoted as $< 2\%$, but this is a conservative figure and today's coatings are undoubtedly better. Netterfield et al. (1980) show that with great care,

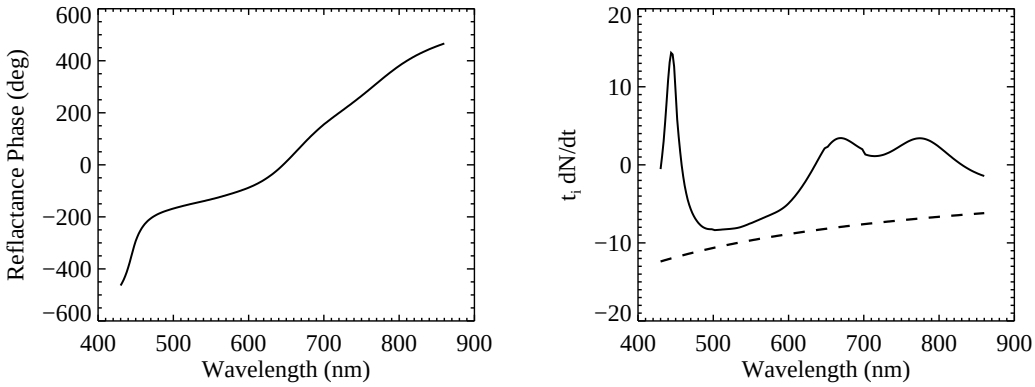

Figure 4.14 Left: calculated phase shift for our coating design. Right: Amplification effect for these coatings; solid curve is full Equation 4.18, dotted curve is the geometrical term alone.

modern coating techniques can achieve $\partial t/t \sim 0.001$. Our measured surface curvatures of RMS amplitude 8 – 13 nm are consistent with the amplification factors of -8 to +3 (from Figure 4.14) and coating thickness variations of $\sim 0.7\%$. To keep the phase dispersion amplified distortions to be less than $\lambda/100$ (the physical flatness of our plates) would require coating thickness variations of less than 0.3% - a demanding but achievable goal.

The change of parallelism with wavelength may also arise from a similar effect. This change occurs in precisely the same wavelength region as the apparent gap change, and so is presumably related to the same sub-structure in the coatings. The similarity of the shape of the parallelism curves for all three etalons, shown in Figure 4.6, suggests that this is a systematic, not random effect. Thus one might suspect that there is a systematic tip between the upper and lower layers of the coating. The measured amplitude of the parallelism changes is -78 ± 20 nm in X and $+59 \pm 7$ nm in Y. The coating irregularities deduced in the previous paragraph were of order 9 nm, and the effect of Equation 4.18 could amplify these by factors ~ 10, so it is possible that this could produce the amplitude of the effect. The shape of the amplification curve in Figure 4.14 (constant at short and long wavelengths and changing rapidly between 600 and 700 nm)

is suggestive of the shape of the parallelism curves; however we do not observe any significant parallelism change around the steep peak at 440 nm of the amplification curve. The plates are marked and their orientation is preserved through the polishing, coating, and assembly processes, so the similarity of the shapes of the parallelism curves for all three etalons could well arise from reproducible irregularities inherent in the coating process. Thus we speculate that the phase dispersion amplification of a relatively small wedge in the coating layers may be the origin of the parallelism changes.

We conclude that it is critical to take into account the effects of phase dispersion when designing broadband coatings for high-finesse FP systems. In our system, the unanticipated effects of the coatings are the main factor that limit the performance of the system. While some specialized FP systems require no relative phase shift over a particular bandwidth (e.g. Lemarquis & Pelletier (1996)), it seems that for general use tailoring the phase dispersion to minimize the amplification effects of equation 4.18 is highly desirable. Although it is unlikely that the competing demands of uniform high reflectance over a broad band and a phase dispersion that cancels the coating effects over the bandwidth can be exactly satisfied, it should be possible to find designs that provide a reasonable compromise.

4.6 Testing the FP system at SALT

The FP system was successfully integrated into the Robert Stobie Spectrograph in Cape Town in August of 2005. We calibrated all the modes around three important wavelengths: 5000 Å, 6500Å and 8200Å. We tested the dual etalon mode for the very first time on RSS for the MR and HR modes. Figure 4.15 shows three images: the top one taken using only the high resolution etalon, the middle one using only the low resolution etalon, and the bottom one using both etalons, in mode. When both etalons are tuned to the same wavelength, the low resolution one selects the desired order, filtering out the rest. Further tests showed that in the dual mode the etalons

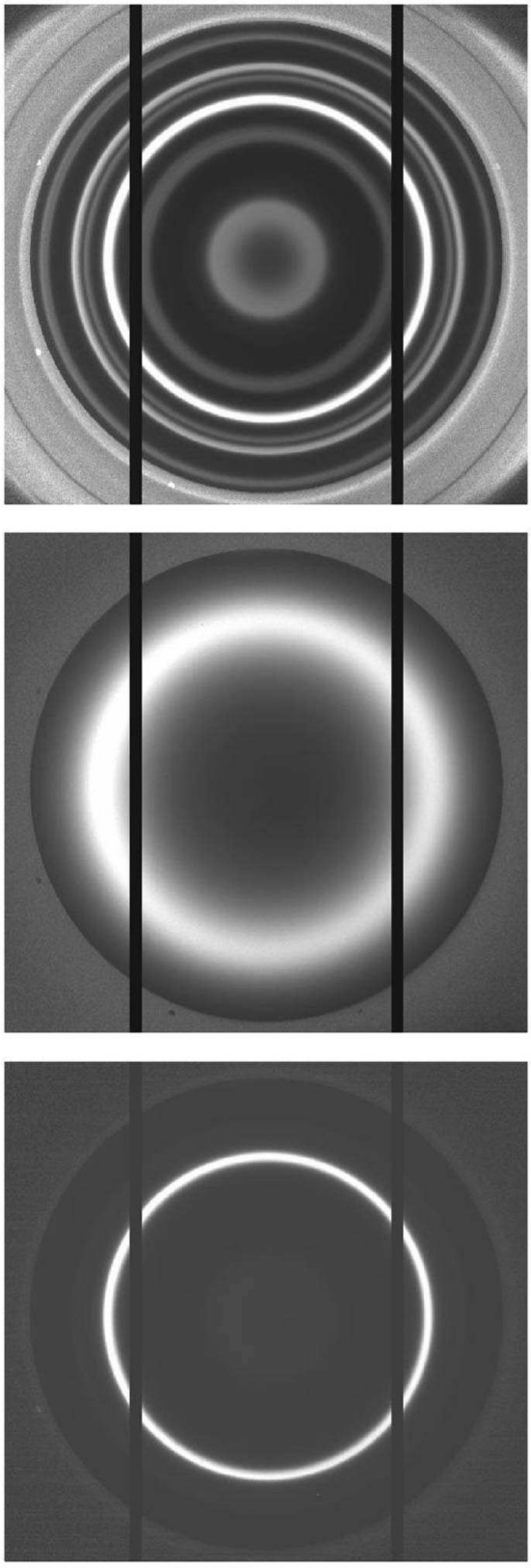

Figure 4.15 Dual Etalon Mode: Top - HR, middle - LR, bottom - dual

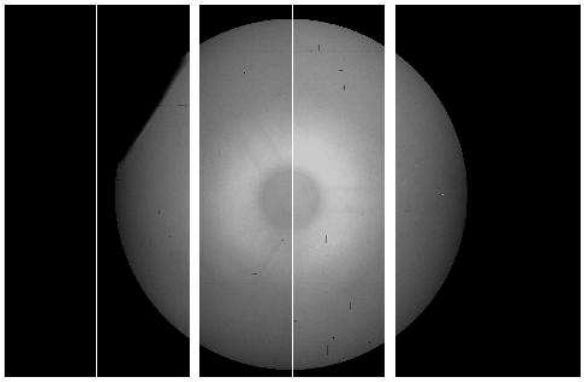

Figure 4.16 The ring ghost in the RSS.

were not tracking accurately in wavelength even though they were aligned physically with each other. This issue was investigated further during on-site commissioning of the FP system when a significant ghost [2] was detected in the flat-field images. This ghost was caused by the reflection off the first surface of the camera field flattener that also serves as a dewar window, then off the back of the interference filter. The ghost takes the doughnut shape of the pupil as shown in Figure 4.16 and is referred to as 'ring ghost'. The intensity of the ghost is enhanced by a factor of two when it reflects off the filter at a different incidence angle compared to its first passage through the filter. The origin of the ring ghost was confirmed by using a circular polarizer on either side of the filter that made it disappear. Further tests revealed that the anti-refection coatings on the dewar window had reflectivity of 8%, well outside the specification. These coatings have been replaced, effectively eliminating the ghost.

Once the RSS was integrated into the telescope, the FP system was affected by noise pickup from other electronics nearby. This was fixed by adding an additional layer of

[2] An optical ghost is defined as light on the CCD produced from internal reflections in the optical system.

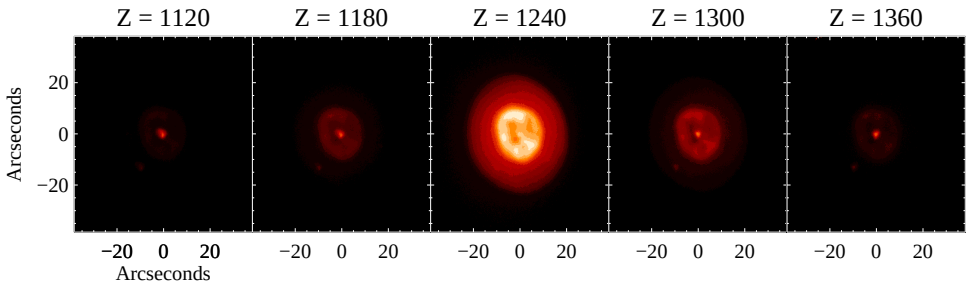

Figure 4.17 First Light I: FP scan of NGC 1535, a planetary nebula.

RFI shielding over the etalon cables and use of AC shielded power cables.

4.6.1 First Light

The first light data using the FP system were taken on 22/23 September 2006. We acquired images of NGC 1535, a planetary nebula of diameter 0.85 arcmin. We obtained a scan of 26 images, each of 60 seconds exposure, covering wavelength range for 643 to 669 nm. The spectral resolution of each image was 0.85 nm. Sample images are shown in Figure 4.17, and show a central star, the inner filamentary structure, and the surrounding featureless shell seen in good ground based images. We also observed NGC 1365, a barred spiral galaxy. The scan consisted of 27 images covering the spectral range for 654.5 to 667.5 nm (around the Hα wavelength redshifted by the systemic velocity of NGC 1365). One of the images is shown in Figure 4.18 (top panel). The bottom panel shows FP velocity field map of the galaxy as measured from the data cube by R. Z. Sanchez. The color represents the line-of-sight velocity at each point in the galaxy. Green areas are moving at the systemic speed of the galaxy, blue regions are coming toward us w.r.t the systemic speed, and red regions are moving away. The organized patterns of the motion show that the galaxy is rotating about its center, while the distortions arise from the gravitational effect of the bar. The details of this rotation map provide clues to the amount and distribution of matter, both luminous and dark, within the galaxy. These data agree well with the previous measurements of the velocity

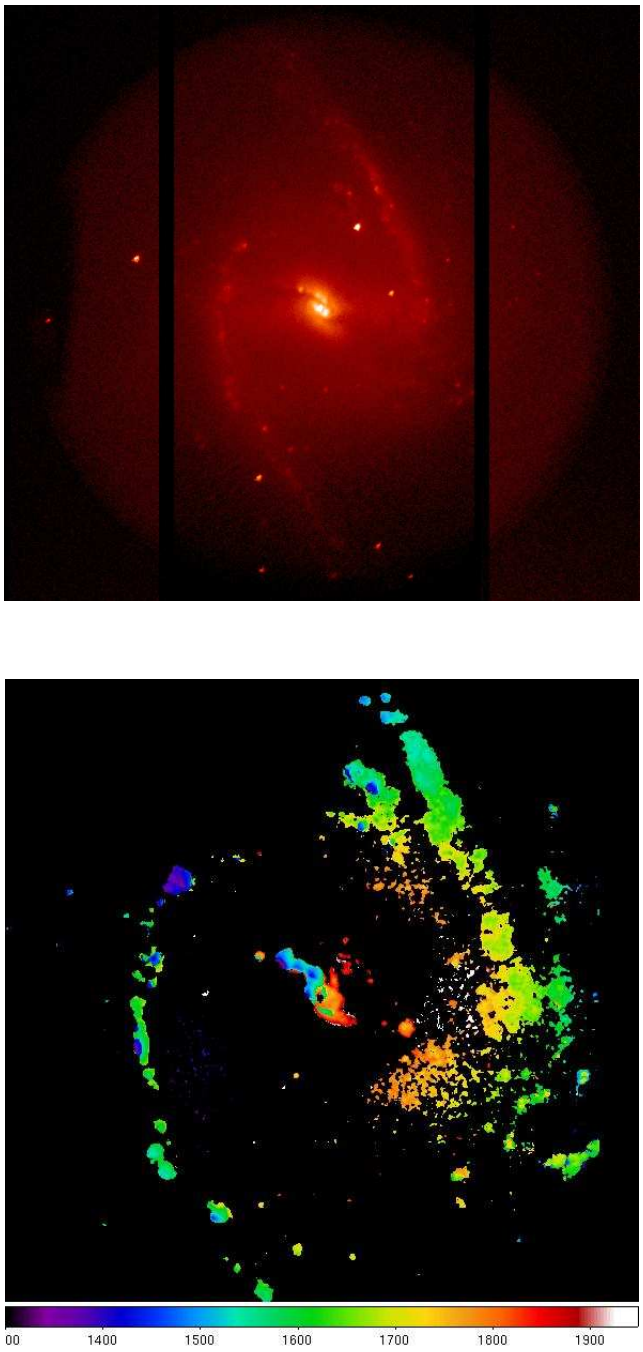

Figure 4.18 First Light II: FP image of a barred galaxy NGC1365 and the corresponding velocity map

field of this galaxy (Zánmar Sánchez et al. 2008).

4.7 Conclusions

In this paper we have presented the design of the SALT FP system, and the laboratory measured characteristics of the as-built system. The system provides spectroscopic imaging at any desired wavelength from 430 to 860 nm in four resolution modes from 300 to 9000. We discovered that the plate parallelism and gap and are wavelength dependent with maximum variation between wavelengths 600 to 720 nm; there is more apparent plate curvature than expected, leading to lower resolution, finesse, and throughput. We believe that all these effects arise from the design of the broadband reflectance coatings of the etalons. It is unfortunate that the $H\alpha$ line falls within the wavelength region of maximum gap and parallelism variation. This will require more care in operating the etalons for many scientific programs, but will not seriously compromise the resulting data. The design goals for the system were based on surveys of the SALT user community, and represent typical but not mandatory requirements for a broad range of scientific investigations. The as-built etalons approach but do not fully meet these goals. The performance of the system is certainly sufficient to satisfy the needs of a very wide variety of programs for the SALT observers, and users will undoubtedly design future investigations to exploit the capabilities of the system.

The SALT FP system will soon undergo performance verification at the telescope and the detailed on-sky performance of this system will be presented in a subsequent paper.

Bibliography

Atherton, P.D., Reay, N.K., Ring, J. & Hicks, T.R. 1981, Optical Engineering, 806, 20

Atherton, P.D., Taylor, K., Pike, David C., Harmer, Charles F.W., Parker, Neil M. & Hook, Richard N. 1982, MNRAS, 201, 661

Burgh, Eric B., Nordsieck, Kenneth H., Kobulnicky, Henry A.,Williams, Ted B., O'Donoghue, Darragh, Smith, Michael P., Percival, Jeffrey W. 2003, Proceedings of the SPIE, 4841, 1463

Bland, Jonathan & Tully, Brent R. 1989, The Astronomical Journal, 98, 723

Bland-Hawthron, Joss & Jones, Heath D. 1998, PASA, 15, 44

Buckley, David A. H., Hearnshaw, John B., Nordsieck, Kenneth H. & O'Donoghue, Darragh 2003, Proceedings of SPIE, 4834, 264

Buisson, H., Fabry, Ch., Bourget, H. 1914, ApJ, 40, 241

Cecil, G. N. 2000, Proceedings of the SPIE, 400, 83

Ciddor, P.E. 1968, Applied Optics, 7, 2328

de Vaucouleurs, G., de Vaucouleurs, A. & Pence, W. 1974, ApJ, 194, L119

Fowles, G.R. 1989, Introduction to Modern Optics, (Dover Publications, INC., NY)

Gelderman, R., Woodgate, B. E. & Brown, L. W. 1995, 3D Optical Spectroscopic Methods in Astronomy, ASP Conference Series, Vol. 71, 89

Giacomo, P. 1958, Le Journal De Physique Et Le Radium, 19, 307

Hartung, Markus, Lidman, Chris, Ageorges, Nancy, Marco, Olivier, Kasper, Markus & Clenet, Yann 2004, Proceedings of the SPIE, 5492, 1531

Kobulnicky, Henry A., Nordsieck, Kenneth H., Burgh, Eric B., Smith, Michael P., Percival, Jeffrey W., Williams, Ted B., O'Donoghue, Darragh 2003, Proceedings of the SPIE, 4841, 1634

Lemarquis, F. & Pelletier, E. 1996, Applied Optics, 35, 4987

Mahapatra, D.P., & Mattoo S.K. 1986, Applied Optics, 25, 1646

Netterfield, R. P., Schaeffer, R. C. & Sainty, W. G. 1980, Applied Optics, 19, 3010

Nordsieck, Kenneth H., Jaehnig, Kurt P., Burgh, Eric B., Kobulnicky, Henry A., Percival, Jeffrey W., Smith, Michael P. 2003, Proceedings of the SPIE, 4843, 170

Pogge, Richard W., Atwood, Bruce, Byard, Paul L., O'Brien, Thomas P., Peterson, Bradley M., Lame, N. J., Baldwin, Jack A. 1995, PASP, 107, 1226

Ramsay, J.V. & Ciddor, P.E. 1967, Applied Optics, 6, 2003

Ryder, Stuart D., Sun, Yin-Sheng, Ashley, Micheal C. B., Burton, Micheal G., Allen, Lori E. & Storey, John W. V. 1998, PASA, 15, 228

Schommer, R.A., Bothun, G.D., Williams, T.B., & Mould, J.R. 1993, AJ, 105, 97

Smith, Michael P., Nordsieck, Kenneth H., Burgh, Eric B.,Percival, Jeffrey W., Williams, T. B., O'Donohue, Darragh, O'Connor, James, Schier, J. Alan 2006, Proceedings of the SPIE, 6269, 62692A

Stobie, Robert, Meiring, Jacobus, Buckley, David A. 2000, Proceedings of the SPIE, 4003, 355

Swat, Arek, O'Donoghue, Darragh, Swiegers, Jian, Nel, Leon, Buckley, David A. H. 2003, Proceedings of the SPIE, 4837, 564

Tufte, S. L., Reynolds, R. J. & Haffner, M. 1998, ApJ, 504, 773

Vaughan, J. M. 1989, The Fabry-Pérot Interferometer, (Adam Hilger, Philadelphia)

Zánmar Sánchez, R., Sellwood, J. A., Weiner, B. J., & Williams, T. B. 2008, ApJ, 674, 797

Chapter 5

Conclusions and Future Work

We successfully show in this thesis that Fabry-Pérot (FP) imaging spectroscopy is very efficient for measuring absorption lines for a large sample of stars. We used this technique to measure the detailed shape of the line of sight (LOS) velocity distribution at three positions along the major axis of the Milky Way (MW) bar. We find the shape to be symmetric and flattopped, which is consistent with a model of the bar where stars stream in elongated orbits along the bar forming two streams at different mean radial velocity, broadening and flattening the total distribution. Our sample was large enough to detect these two streams and measure the difference between their mean radial velocities. The difference in the mean of the two streams is about 35 km s^{-1} at $l = \pm 5$ and almost zero in BW. The latter could be the result of contamination from an old classical bulge population with large random motion as indicated by our velocity dispersion value in this field. The survey with the SALT FP system as described in Chapter 2 will allow such measurements for several LOS in the bar. This will enable us to look for gradients in shape of the velocity distributions, and in radial streaming motions, if any, as a function of position along the bar. The modeling of this data is an on-going work where we are using made-to-measure models of the inner Galaxy that are being developed by Debattista et al. (in prep.). Ideally, we would use this model to predict the more sensitive LOS in the bar for future observations of stellar kinematics.

The survey of the bar with SALT FP system will enable us to obtain about 2000 stars per LOS. This is twice our current sample for an individual LOS and will allow us to measure more precisely the kinematics of red clump giants (RCGs) as a function

of apparent magnitude (or distance) in the bar. We made an attempt to measure this trend with our current sample and found it to be consistent with the model of Häfner et al. (2000). But the number of stars in each magnitude bin is still low. A large sample will increase the possibility of detecting the transition from disk to bar, and measure the bar's thickness directly.

We went beyond the initial goal of this work, which was to only obtain the radial velocities from our FP data set, to measure the Ca II λ8542 line strengths. Because Ca II λ8542 line is a reliable indicator of stellar metallicity in the cool giants, we can use the equivalent width (EW) of this line to derive [Fe/H] for our sample. We find that the limited FP bandpasses do not introduce any systematic bias in our EW compared to fitting the absorption line over a wider bandpass, but increases the uncertainty in EW by a factor of 1.5. By choosing a different observing strategy for the future survey, we can lower these uncertainties. Simulating synthetic spectra shows that we can reduce the uncertainty by factor of 2 by taking four samples on the red end of the line feature (between 8555 – 8580 Å). Increasing our S/N from 20 to 40 will make our EW more accurate by another factor of 2.

We checked the reliability of our EWs by measuring the metallicity of a bulge globular cluster NGC 6522 that is present in our BW field. We find its metallicity to be in good agreement with the high-resolution spectroscopic measurement obtained by Zoccali et al. (2008). Both works find the metallicity of this globular cluster to be around -0.9 dex. This is much lower than expected for a cluster that has an extremely blue horizontal branch. We believe that NGC 6522 is perhaps one of the second parameter clusters, in which case the horizontal branch magnitude is not the sole parameter in determining its metallicity. This case is similar to another bulge globular cluster NGC 6558 measured by Barbuy et al. (2007) that also has relatively lower metallicity than expected from the location of horizontal branch on the color-magnitude diagram.

We measured the stellar metallicity distribution for our three LOS in the bar. The

distribution in BW agree well with previous measurements of Zoccali et al. (2008) and Fulbright et al. (2006). The mean metallicity in BW is close to solar and we find a gradient of up to 0.4 dex in the mean along the bar, different on either sides of the BW. The gradient in metallicity dispersion is about 0.2 dex on each side of BW. In addition this trend correlates with the LOS velocity dispersion that also decreases by the same amount. Bars and bulges in external galaxies show metallicity gradients that are found useful in constraining the star formation history and structure formation in the inner parts of disk galaxies. The same can be done from our measurements in the bar. Our current metallicity data set has relatively large uncertainties, limiting the accuracy in determining the shape of stellar metallicity distributions; this will be significantly improved by changing the FP observing strategy in our future survey.

One of the most exciting possibilities of measuring high S/N velocity and metallicity distribution is to look for tidal streams or debris left behind by disrupted satellites of the Milky Way (MW). One of the best examples yet is that of the Sagittarius dwarf galaxy and its tidal debris wrapped around the MW. We see a possible signature of a tidal stream at $l = +5.5\ ^{\circ}$ field both in velocity and metallicity distributions at 36.5 km s^{-1} and -1.0 dex respectively. We conclude that the stars in this stream are not associated with the Sagittarius stream on the basis of our radial velocity. This result is very encouraging for the future survey with SALT that will be even more sensitive in detecting these features due to large sample size and lower uncertainties.

Finally in Chapter 4 we presented the design and testing of the SALT FP system that will make possible the future survey of the inner Galaxy. This is the only FP system on a 10-m class telescope that provides a variety of spectral resolution over the entire optical bandpass. The next generation instruments on SALT will include a near-infrared FP system that will extend the observing bandpass even further.

Bibliography

Barbuy, B., Zoccali, M., Ortolani, S., Minniti, D., Hill, V., Renzini, A., Bica, E., & Gómez, A. 2007, AJ, 134, 1613

Fulbright, J. P., McWilliam, A., & Rich, R. M. 2006, ApJ, 636, 821

Häfner, R., Evans, N. W., Dehnen, W., & Binney, J. 2000, MNRAS, 314, 433

Zoccali, M., Hill, V., Lecureur, A., Barbuy, B., Renzini, A., Minniti, D., Gómez, A., & Ortolani, S. 2008, A&A, 486, 177

Chapter 6

Curriculum Vitae

Education and Research Positions

2003 – 2009	Ph.D., Physics, Rutgers University, New Brunswick, NJ
2002 – 2003	Graduate & Teaching Assistant, High Energy Physics, Rutgers University
2000 – 2002	M.S., Particle Physics, Durham University, Durham, UK
1997 – 2000	B.Sc., Physics, Wilson College (Mumbai University), Mumbai, India

Publications

1. **Rangwala, N.**, Williams, T. B., Pietraszewski, C., Joseph, C. L., " An Imaging Fabry-Pérot System for the Robert Stobie Spectrograph on the Southern African Large Telescope", *The Astronomical Journal*, (2008) **135**, p 1825-1836

2. **Rangwala, N.**, Williams, T. B. & Stanek, K. Z., "Fabry-Pérot Absorption Line Spectroscopy of the Galactic Bar I: Kinematics" 2009, *the Astrophysical Journal*, Volume 691, Issue 2, pp. 1387 - 1399

3. **Rangwala, N.** & Williams, T. B., "Fabry-Pérot Absorption Line Spectroscopy of the Galactic Bar II: Stellar Metallicity Distributions" 2009, submitted to *the*

Astrophysical Journal

4. Romero-Colmenero, E., Buckley, D., Kniazev, A., Vaisanen, P., Loaring, N., Still, M., Hashimoto, Y., Potter, S., O'Donoghue, D., Nordsieck, K., Burgh, E., Williams, T., Sanchez, R., **Rangwala, N.**, "First Observations with the Southern African Large Telescope (SALT)" 2007, in "The Central Engine of Active Galactic Nuclei", *ASP Conference Series*, Vol. 373, 717

5. Buckley, D. A. H., Barnes, S. I., Burgh, E. B., Crawford, S., Cottrell, P. L., Kniazev, A., Nordsieck, K. H., O'Donoghue, D., **Rangwala, N.**, Sanchez, R. Z., Sharples, R. M., Sheinis, A. I., Vaisanen, P., Williams, T. B., "Commissioning of the Southern African Large Telescope (SALT) First-Generation Instruments", 2008, Ground-based and Airborne Instrumentation for Astronomy II. Edited by McLean, Ian S.; Casali, Mark M., *Proceedings of the SPIE*, Volume 7014, pp. 701407-701407-15